Advanced research on Lithium-Sulfur batteries: studies of lithium polysulfides.

by

Pierre-Etienne Cabelguen

A thesis
presented to the University of Waterloo
in fulfillment of the
thesis requirement for the degree of
Master of Science
in
Chemistry

Waterloo, Ontario, Canada, 2013

© Pierre-Etienne Cabelguen 2013

AUTHOR'S DECLARATION

I hereby declare that I am the sole author of this thesis. This is a true copy of the thesis, including any required final revisions, as accepted by my examiners.

I understand that my thesis may be made electronically available to the public.

Pierre-Etienne Cabelguen

ABSTRACT

Lithium-sulfur (Li-S) battery is a popular system investigated since the 1970s, but it has not reached mass commercialization yet due to its poor capacity retention over extended cycling. This thesis was devised as a fundamental study of the Li-S system by the use of ^{7}Li Magic Angle Spinning (MAS) Nuclear Magnetic Resonance (NMR), X-ray Absorption Near-Edge Structure (XANES), and Non-Resonant Inelastic X-ray Scattering (NRIXS).

The first part of this thesis is dedicated to the synthesis of solid state linear chain polysulfides in order to use them as reference compounds in the following experiments. Lithium polysulfides are synthesized via the chemical reduction of α-S_8 by lithium triethylborohydride. ^{7}Li NMR shows that Li_2S and Li_2S_6 exhibit single but different Li environments, while the others stoichiometry targeted consist of a mixture of them. This is the first report of a stable solid-phase intermediate between elemental sulfur (α-S_8) and Li_2S.

The second part of this thesis is based on *operando* XANES measurements made in the Argonne Photon Source (APS). The principal challenge of such experiment comes from the self-absorption of large sulfur particles (> 100 nm) that particularly distorts the spectra, which was avoided by by confining sulfur in porous carbon nanospheres (PCNS) synthezised by other group members. Linear combination fit (LCF) analyses are performed to interpret the data; and, noticeably, the distinction between short-chain and long-chain polysulfides can be made due to the use of proper reference materials. The results reveal the first detailed observation of typical sulfur redox chemistry upon cycling, showing how sulfur fraction (under-utilization) and sulfide precipitation impact capacity. It also gives new insights into the differences between the charge and discharge mechanisms, resulting in the hysteresis of the cycling profile.

Heat-treated PCNS/S exhibits a particular electrochemical signature, which has never explained. After a preliminary electrochemical study by potentiodynamic cycling with galvanostatic acceleration (PCGA), *operando* XANES measurements at the sulfur K-edge are performed on heat-treated PCNS. Noticeably, the difference in the XANES signatures of the pristine and the recharged state shows the irreversible process that occurs during the first discharges. However, it is difficult to conclude regarding the particular sulfur redox mechanism since the features present in the spectra are identical to the one found in standard Li-S system.

At last, electrolytes are investigated by the compilation of quantitative physico-chemical parameters – viscosity, ionic conductivity, and solubility of Li_2S and Li_2S_6 – on novel class of solvents that are glymes with non-polar groups and acetonitrile (ACN) complexed with LiTFSI. However, all the novel electrolytes explored exhibit too high viscosities and too low ionic conductivities. 1,1,2,2-Tetrafluoroethyl 2,2,3,3-tetrafluoropropyl ether (HFE) is chosen to decrease their viscosities. $(ACN)_2$:LiTFSI attracts particular attention because of the particularly low Li_2S_n solubility and. Its good electrochemical performance when mixed with 50 vol% HFE. *Operando* XANES proves the formation of polysulfides in this electrolyte, although constrains imposed by this novel electrolyte to the XANES experiment complicate the data analysis. The low energy feature evolution shows a more progressive mechanism involved in this electrolyte, compared to standard glyme electrolytes, which could be linked to the particularly low Li_2S_n solubility.

In conclusion, new spectroscopic tools – namely XANES, NRIXS, and ^{7}Li NMR – were applied to Li-S batteries using the first solid-state single phase polysulfide, Li_2S_6, reported. These have allowed finding new insights in the working mechanism of typical Li-S cell as well as untypical systems (heat-treated active material and particular electrolytes).

ACKNOWLEDGEMENTS

I would like to thank my supervisor, Professor Linda F. Nazar, for her guidance and trust throughout the course of this research project. I would also like to extend my appreciation to the members of my committee, Pr. Kleinke and Pr. Prouzet.

I would like to express my gratitude to Dr. Marine Cuisinier who helped me during my 2 years. I whould also like to thank you Dr. Mali Balasubramanian for his help at the Argonne Photon Source in Chicago. I would also like to thank all members of my lab for their assistance.

Table of contents

List of Figures

List of Tables

List of Abbreviations

1NM1	Monotrimethylsilated monoglyme
1NM2	Monotrimethylsilated diglyme
ACN	Acetonitrile
AFM	Atomic Force Microscopy
APS	Argonne Photon source
CPE	Constant Phase Element
CV	Cyclic voltametry
DEC	Diethyl carbonate
DMDMB	1,2-dimethyl-1,2-dimethoxybutane
DME	1, 2-dimethoxyethane
DOL	1, 3-dioxolane
DSC	Differential Scanning Calorimetry
EC	Ethyl carbonate
EIS	Electrochemical Impedance Spectroscopy
EMS	Ethyl Methanesulfonate
EV	Electric Vehicle
EXAFS	Extended X-ray Absorption Fine Structure
FID	Free Induction Decay
GCPL	Galvanostatic Cycling with Potential Limitation
HEV	Hybrid Electric Vehicle
HF	High Frequencies
HFE	1,1,2,2-Tetrafluoroethyl 2,2,3,3-tetrafluoropropyl ether
HPLC	High-Performance Liquid Chromatography
IL	Illinois

Li-S	Lithium-Sulfur
Li_2S_n	Lithium polysulfide, $n > 1$
LCF	Linear Combination Fit
LERIX	Lower Energy Resolution Inelastic X-ray scattering
LF	Low Frequencies
LiTFSI	Lithium Bis(Trifluoromethanesulfonyl)Imide
MAS	Magic Angle Spinning
Me_2S_n	Dimethyl sulfides
MeTf	Methyl Trifluoromethaesulfonate
MWCNT	Multi-Walled Carbon Nanotube
Na_2S_n	Sodium polysulfide , $n > 1$
Ni-Cd	Nickel-Cadmium
Ni-MH	Nickel-Metal hydride
NMR	Nuclear Magnetic Resonance
NRIXS	Non-Resonant Inelastic X-ray Scattering
PCGA	Potentiodynamic Cycling with Galvanostatic Acceleration
PCNS	Porous Carbon Nanosphere
PCNS/S	Porous Carbon Nanospere impregnated with Sulfur
PEO	Poly(ethylene oxide)
PVDF	Polyvinylidene fluoride
PXRD	Powder X-ray Diffraction
rpm	Rotation per minute
TEGDME	Tetra(ethylene glycol)-dimethyl ether
TEY	Total Electron Yield
TGA	Thermogravimetric analysis

THF	Tetrahydrofuran
U.R.I.	University of Rhode Island
UV	Ultra-Violet
U.W.	University of Waterloo
VHF	Very High Frequencies
XAFS	X-ray Absorption Fine Structure
XANES	X-ray Absorption Near-Edge Structure
XPS	X-ray Photoelectron Spectroscopy
XRD	X-ray Diffraction
XRS	X-ray Raman Spectroscopy
wt%	Weight Percentage

1. Introduction: The lithium-sulfur battery.

1.1. The field of energy storage is expecting better batteries.

The idea of making an effective electric vehicle these days is everywhere, and most of the scientific research on electric energy storage are funded in this perspective. Electric power in automotive is not new and plenty electrified-vehicles are now reaching the market. Car manufacturers are forced by the legislation, especially in the EU and the USA,[1,2] to raise fuel efficiency and to lower carbon dioxide (CO_2) emissions. It has also been a major marketing argument. Today, most of the cars present on the market are equipped with internal battery for reducing CO_2 emission by proposing regenerative braking or stop-start function. The classification distinguishes between hybrid electric vehicles (HEV) and electric vehicles (EV). HEV still include a combustion engine, but incorporate a battery to support it, typically when efficiency of the combustion is at its lowest. The first HEV built in series was the Toyota Prius in 1997. In HEV, the reduction in fuel consumption cannot exceed 30%. In contrast, EV does not use any internal combustion engine − all the power is provided by the battery − that is why they are locally emission-free. Unfortunately, to date, the possible driving range of EVs cannot compete with any combustion engine. Improvements need to be made in almost all the critical point for batteries: safety (because high voltage is needed), power density, energy density and capacity retention. Today, the battery in EVs is certainly the most expensive part of the car.[3] The costs of new systems are however difficult to estimate, since industrial production and electricity prices will change them.

To match the customers' behavior, the goal is to make electric cars with driving range around 100 km, which would represent around 90% of all trips. Current technology used in cars

is summarized in **Table 1**. The terms energy density and power density are defined in the next section. Lead acid batteries are based on the redox process between two electrodes of lead and an electrolyte of concentrated sulfuric acid, while Ni-Cd and Ni-MH are nickel-based (Nickel-Cadmium and Nickel-metal hydride, respectively). Lead acid batteries are used in all the cars to power the starter motor, the lights, and the ignition system of a vehicle's engine. Ni-MH is nowadays the most popular system for HEV.

Table 1. Technical performance by existing battery type.

Battery type	Lead acid	Ni-Cd	Ni-MH	Lithium-ion
Energy density (Wh/kg)	35	40-60	60	120
Power density (W/kg)	180	150	250-1000	1800
Cycle life	4500	2000	2000	3500
Cost ($/kWh)	269	280	500-1000	Electronics: 300-800 Vehicles: 1000-2000
Battery characteristics	High reliability Low cost	Memory effect	Most popular for HEVs	Small size Light weight
Application	Car battery Backup power	Replacement for flashlight battery	HEVs Replacement for flashlight battery,	Consumer electronics

1.1.1. Vocabulary, main characteristics.

An electrochemical cell is a device that converts chemical energy into electrical energy and *vice versa*. It consists in the assembly of the cathode and anode electrodes separated by a porous layer that is both an ionic conductor and an electrical insulator. The labels anode and cathode can be confusing in a rechargeable system. The anode is formally the electrode where an

oxidation occurs, while the cathode is where a reduction occurs. During cycling, these labels should switch when switching between charge and discharge. In the literature of lithium-sulfur batteries however, the term cathode always designates the electrode containing the elemental sulfur while anode designates the electrode made of lithium metal. The terms positive electrode (sulfur electrode) and negative electrode (lithium anode), referring to the potential, can avoid any ambiguity. The operation of a cell is based on the difference between the chemical potential of the active material between the two electrodes. A battery has several parameters to describe its performance and operating conditions:

- The gravimetric **power density** (i.e. per mass) and the volumetric power density (i.e. per volume) is the power available when the battery is discharged at a certain discharge current, normalized by the mass of active material and the volume, respectively. As a reminder, the electric power provided by an electric current I through a voltage V is I.V, in Watts.

- The gravimetric and volumetric **energy densities** are the total Watt-hours available when the battery is discharged at a certain discharge current, normalized by the mass of active material and by the volume, respectively. It is calculated by multiplying the power by the discharge time.

- The **specific capacity** of a cell is equal to the total amount of current available when the battery is fully (dis)charged from (up to) x Li: $Q = 1000.x.F/(3600.M)$ where F is the Faraday constant and M the molecular mass of the active material (32 g.mol^{-1} for sulfur).

- The **voltage window** inside which the cell is running. The potential of Li^+/Li^0 is set to 0.00 V by convention. Different active materials used as the electrodes exhibit different redox potentials. A redox reaction occurs ideally at a fixed potential. Having a high cell

potential is important to achieve a high energy. In practice, the voltage window used is set by the operator to perform at best the desired redox process(es). However, it is important to avoid any degradation of the electrolyte or the current collector, which could be reduced or oxidized in the potential window.

- The **columbic efficiency** refers to the ratio of discharged capacity over the preceding charged capacity. It indicates the reversibility of the redox process, and can show if excess electrons are needed to charge the cell compared to the number of electrons available from discharge.

- The **cell polarization**, or overpotential, is the potential difference between an electrode equilibrium potential and its operating potential when a current is flowing. It represents the extra-energy needed to force the redox reaction to proceed. It gives rise to energy loss by heating, and possibly to parasitic reactions if the voltage window has to be widened excessively.

- The **rate capability** describes the capability of a cell to respond to an electrical current applied, depending on its magnitude. The current is commonly referred in term of "n.C". C is defined as the current needed to fully discharge the cell in 1 hour, by considering the theoretical capacity. Another definition states that this is the current applied to intercalate one lithium ion in one hour. This second definition is more convenient to compare between different batteries. However, the first definition given is the most common one in the lithium sulfur literature and will be used in the following.

Besides, all the gravimetric values reported in this work are normalized by the amount of elemental sulfur present in the cathode composite.

1.1.2. Secondary batteries based on lithium chemistry.

Lithium metal is the ultimate negative electrode: its lightness leads to the highest gravimetric energy possible while its electronegativity provides the highest possible cell voltage against any given positive electrode. Its low atomic size results in a high mobility. Overall, this results in the highest energy and power densities for all commercially available rechargeable batteries as shown on **Figure 1**. Today, Li-ion batteries appear to be the best candidate to replace nickel-based batteries and to take over the automotive market in the next years. Besides, Li-ion technology can cover a wide range of applications, from high power to high energy systems. Unfortunately, cells present on the market for consumer applications (mobiles, laptops, etc.) do not fulfill the automotive application requirements in terms of safety and power/energy. Their adaptation is under development, and first EVs equipped with lithium-ion packs, such as the Nissan Leaf, Mitsubishi I MiEV, Tesla Roadster, Renault ZOE or Bolloré Bluecar, have appeared on the market. The driving range reported by the manufacturers depends obviously on the speed used, but it is already superior to 100 km for highway capable cars – i.e. with a speed capability > 100 km/h.
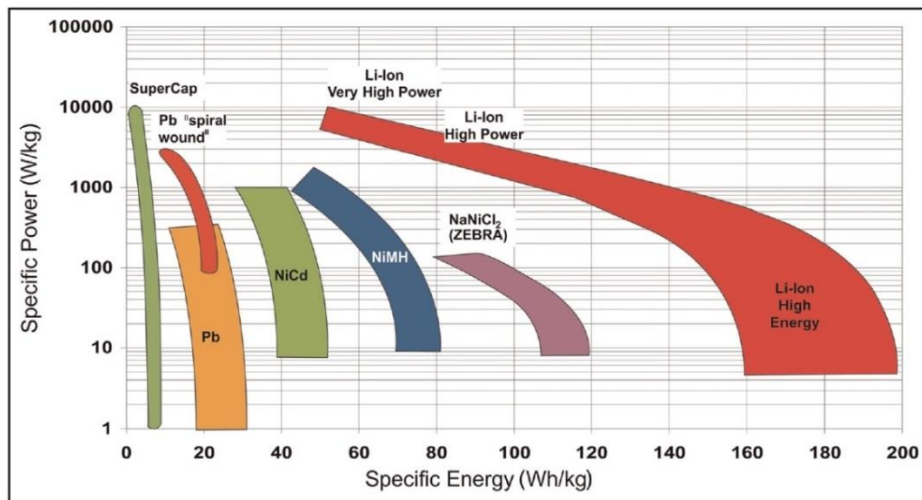
Figure 1. Plot of the specific power vs. specific energy for several battery systems.[3]

A conventional commercial Li-ion cell – exactly like the first one launched by Sony in 1991 – relies on a transition metal based lithium host such as $LiCoO_2$ or $LiFePO_4$ for the positive electrode and a graphitic carbon as the negative electrode. The common electrolyte used is based on carbonate solvents with lithium salts such as $LiPF_6$. During discharge, oxidation at the negative electrode releases Li^+ ions which diffuse through the electrolyte towards the positive electrode. Electrons pass through the external circuit thus generating power. During charge, the reverse processes occur upon external power supply. This mechanism of (de)insertion is highly reversible, and minimal structural change occurs.

Despite their high attractiveness, many problems arise from the use of lithium-ion batteries in cars. One of the most important is a safety concern. Lithium-ion batteries are vulnerable to short-circuiting and overcharging.[4] The retail price is also problematic since it is estimated at one to four times that of nickel-based batteries. However, the cost is expected to decrease while the market grows and production scales up, by a factor of 2 from 2009 to 2020, according to the Deutsche Bank.[5]

Present research on lithium-ion batteries is reaching the theoretical energy and power densities limits. Increasing the performance of electric vehicles as well as lowering the costs appears difficult or even unlikely with current technology. New systems are under investigation for the future. Lithium-sulfur (Li-S) and lithium-air, i.e. the use of sulfur and oxygen, respectively, as the positive electrode, are really promising. The chemistry of these systems is vastly different from lithium insertion typical of Li-ion host materials. Instead, it involves phase-transformation that promises higher energy density. Lithium-sulfur batteries are described in the next section.

1.2. Lithium-sulfur batteries.

1.2.1. Overview of Lithium-sulfur batteries.

1.2.1.1. Lithium-sulfur redox chemistry: a complex mechanism.

Li-S batteries – in which the negative is lithium and the positive sulfur – are a very attractive system due to its high gravimetric and volumetric energy densities. **Figure 2** illustrates the functioning of a Li-S cell.
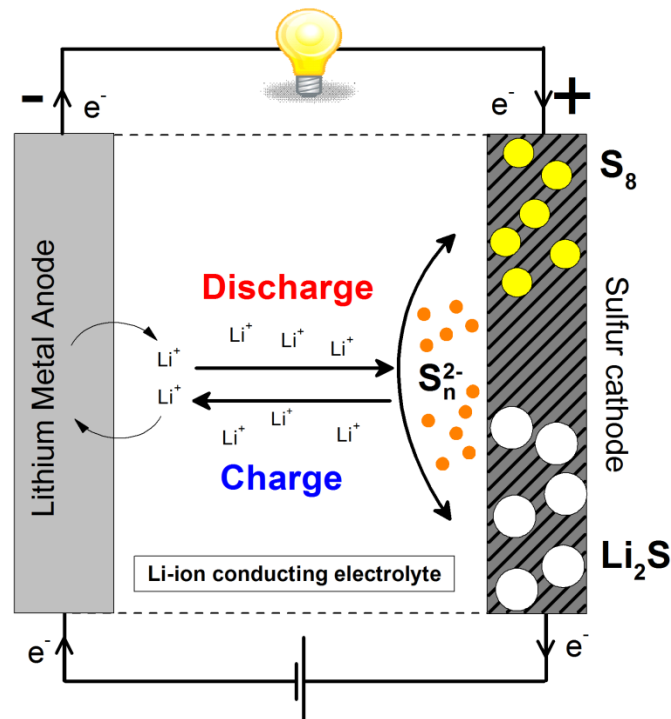
Figure 2. Schematic of a typical Li-S cell.

During discharge, lithium ions liberated by the oxidation of the metal anode migrate through the electrolyte to react with the electrons (external circuit) and reduce the elemental sulfur in the positive electrode. The S_8 ring is opened and subsequent shortening of the sulfur

chain length is thought to occur. During charge, the lithium ions migrate back to the negative electrode where they react with an electron to reform lithium metal. The overall redox reaction $S_8 + 16Li \leftrightarrow 8Li_2S$ occurs around 2.15 V with respect to Li^+/Li^0. However, the reactions involved are vastly different from solid—state intercalation that typically governs the lithium-ion battery chemistry, with the formation of numerous soluble intermediates species Li_2S_n ($8 \leq n \leq 2$).[14]

The theoretical gravimetric capacity of Li-S batteries is 1672 mAh.g^{-1}. Its theoretical energy density is 2500 Wh.kg^{-1} based on weight and 2800 Wh.L^{-1} based on volume, assuming complete reaction to Li_2S.[6] It is 3-5 times higher than lithium-ion batteries. However, these values have to be reassessed since most of the cathodes and sulfur cathode composites proposed in the literature present an active material fraction below 60 wt% with porosity regularly above 30%. The actual energy density of such a positive electrode would not exceed the current level of lithium-ion.[7] **Figure 3** shows a typical voltage profile of a Li-S cell when applying a constant electrical current between 3 V and 1.5 V. The discharge consists in two voltages plateaus, one around 2.35 V and the second around 2.1 V corresponding to the first reduction of S_8 to soluble polysulfides and to the second reduction of these polysulfides to insoluble Li_2S, respectively.[8] The two plateaus are delimited by a supersaturation point (red on **Figure 3**), which denotes to a supersaturated solution of S^{2-} before its precipitation. The charge consists of a first over-potential highlighted on the curve and then a long slopping curve. The presence of this over-potential (i.e. energy barrier, blue on **Figure 3**) shows the difficult oxidation of insoluble and insulating Li_2S.
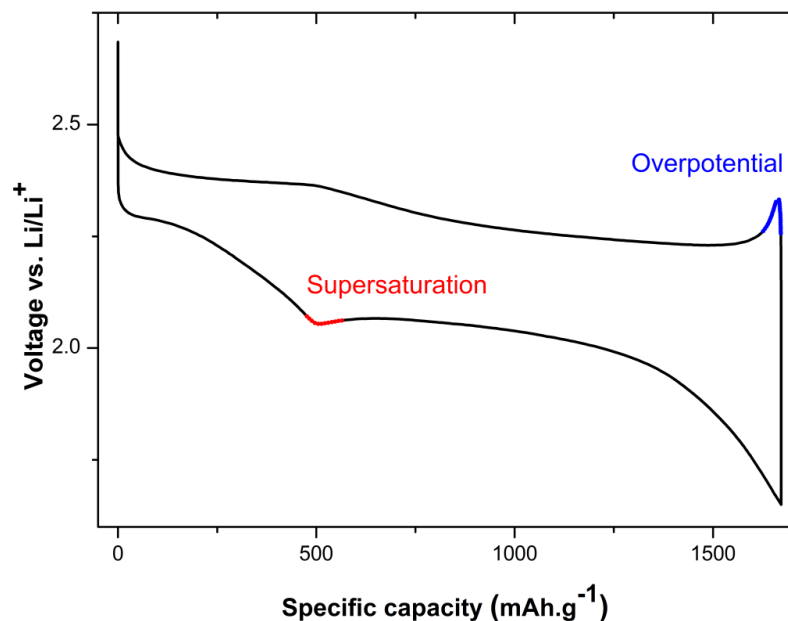
Figure 3. Typical voltage profile obtained for a typical Li-S battery.

1.2.1.2. Challenges of designing lithium sulfur batteries.

The most obvious issue arising for the use of elemental sulfur as an active material in an electrochemical device is its insulating behavior for both ions and electrons.[9] The products of its reduction are also expected to be insulators, especially the very end product Li_2S. Therefore, elemental sulfur alone cannot be used as a material in an electrode, but needs to be intimately mixed with a conductive additive such as carbon. Such dilution is problematic to attain high sulfur loading necessary to a high energy density. Also, the end product Li_2S exhibits a lower density than elemental sulfur (1.66 $g.cm^{-3}$ and 2.06 $g.cm^{-3}$ respectively). It means that the formation of Li_2S result in an increase of the volume of positive electrode.[10] This change in volume has to be taken into account when designing the sulfur host, because it limits the maximum sulfur content, and results in severe mechanical stress and decrepitation.[11] The

9

precipitation of Li_2S results in insoluble agglomerates on the surface of the positive electrode that become electrochemically inaccessible.[12,13]

And yet most of the problems arise from the actual chemistry of sulfur intermediates. Its complexity and thus the lack of understanding are deeply problematic to develop Li-S system as a viable alternative for energy storage. The overall equation of the conversion of elemental sulfur to lithium sulfide Li_2S does not show the various intermediate species, lithium polysulfides Li_2S_n, $2 \leq n \leq 8$,[14] formed by the reduction of S_8 or the oxidation of Li_2S. These lithium polysulfides are poorly known and their respective stability is still discussed in the literature. The fact is that they are highly soluble in the electrolyte, and thus readily diffuse in it.[15] If they reach the lithium metal counter electrode, they can be reduced further to insoluble Li_2S that passivates – i.e. forms a blocking surface – the negative electrode.[12] Another phenomenon arising is a shuttle process during which the polysulfides are reduced at the negative, and then diffuse back to the positive to be oxidized. This process can take place repeatedly. It results in a decrease of the coulombic efficiency and in self-discharge.[16] The migration of active material in the electrolyte is also a cause of capacity loss during the first cycles, even if recent studies tend to show that it does not participate in long-term capacity fading.[17,18] The lack of knowledge of the behavior of these soluble polysulfides is major hindrance to design a proper Li-S cell.

1.2.2. Understanding of the behavior of the cell.

1.2.2.1. The limiting factors are better and better understood.

So far, the performances of Li-S cells proposed in the literature are far from industrial requirements and from theoretical consideration of the Li-S system. The usual gravimetric capacity of the first discharge presented in the literature is around 1200 $mAh.g^{-1}$, which is around

75% of the theoretical value.[19,20] Only really high dilution of sulfur in the cathode host leads to a higher capacity.[21] 1200 mAh.g^{-1} is a decent value, yet all of the results presented fail to achieve 85% capacity retention after 100 cycles. Besides, the rate capability of Li-S cells is also disputable, since cells are usually run at rates below 1C. The second discharge step, i.e. the 2.1 V plateau, is highly sensitive to the discharge rate.[12] Higher rates lead to much less utilization of the active material, and hence to lower capacity. Also, the polarization of the system is problematic since the oxidation takes place at a much higher potential than the reduction, commonly higher by 0.4 V. It means that, even at equal capacities, more energy is needed to charge the battery than the energy obtained during discharge, leading to a loss of energy upon cycling.
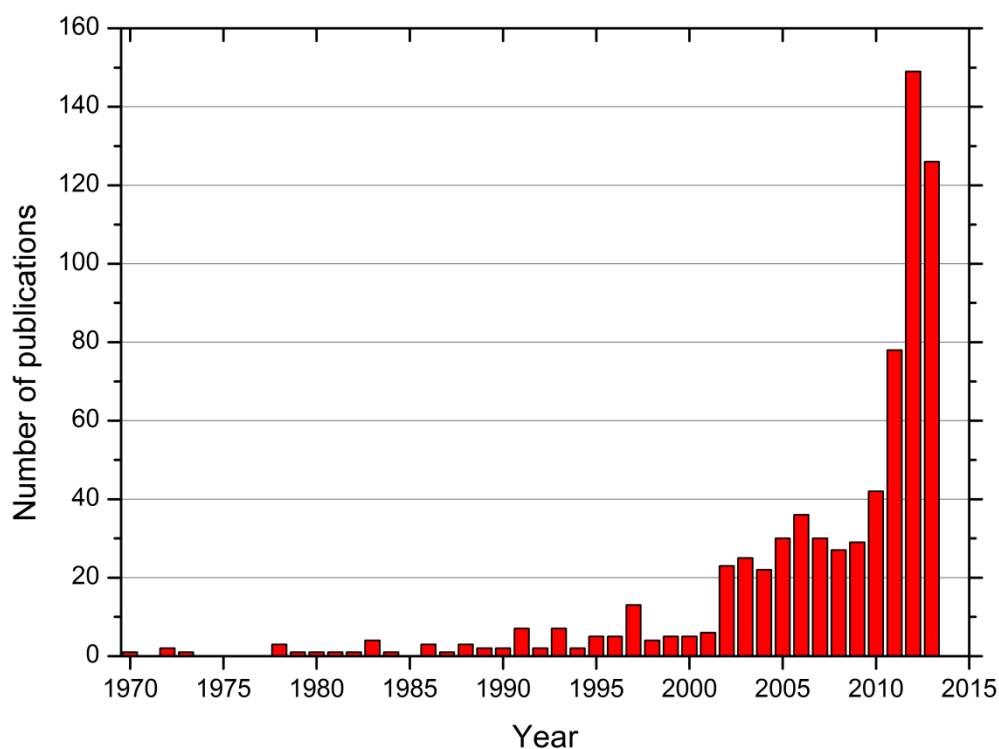
Figure 4. Number of publications on Li-S system vs. the year until July 2013. (Data from Web of Science)

Many different strategies have been pursued to develop Li-S cell. Indeed, the number of publications has increased drastically as shown on **Figure 4**. Most of this literature focuses on

11

increasing the performance and results are indeed getting better and better, but the understanding of the system is also importantly investigated; the reasons for the bad behaviors described in the previous paragraph are not yet all identified however. The change in hydrophobic/hydrophilic interactions has been identified as important in the Li-S cell.[22] While elemental sulfur is hydrophobic, both soluble polysulfides and Li_2S are hydrophilic. Carbon commonly used in the cathode composite is hydrophobic, thus more favorable for elemental sulfur ad/ab-sorption. These changes make the design of the sulfur host delicate, to favor the formation of one or another species and then directly impact the performance of the system. Besides, the low capacity reported during the first discharge is indicative of a poor utilization of the active material that is thought to be inaccessible, lost in the electrolyte under the form of soluble polysulfides or passivated before reacting by the precipitation of insulating Li_2S on the positive electrode that become electrochemically inaccessible.[12,13]

The loss of capacity upon long-term cycling can be ascribed to several factors. First, the loss of active material in the electrolyte is definitively responsible for a part of this. As presented later in 1.2.3.1, the cathode design was developed to inhibit the migration – and loss – of soluble polysulfides outside the electrode. Nevertheless, *in situ* transmission X-ray microscopy imaging[17] and *ex situ* analysis of electrolytes[18] indicated that this factor may not be as severe as previously thought. Detachment of Li_2S from hydrophilic surface and the resulting loss of electronic contact are also believed to play a key role in the loss of capacity.[22] The deterioration of the cathode architecture upon cycling due to the phase transitions and the volume expansion/contraction has been widely mentioned in the literature. It shuts down the strategy of wisely design the positive electrode host because the cathode composite undergoes severe mechanical stress, and can break

12

apart as shown by ex situ Atomic Force Microscopy (AFM).[11] It could encourage all-liquid Li-S batteries that stop the redox process before the precipitation of elemental sulfur of Li_2S.

1.2.2.2. A complex redox mechanism.

As stated before, the mechanisms involved in a Li-S cell are not well-understood. Some works tried to understand the redox mechanism involved during discharge contrary to the charge mechanism that is believed to be much simpler, and therefore was never studied thoroughly. Some papers propose a mechanism for the discharge involving Li_2S_8, Li_2S_6, Li_2S_4 and/or Li_2S_2. These polysulfides are uncharacterized in the solid state, making difficult the understanding of the redox scheme, which is thus mostly based on the electrochemistry signature for now. Ultra-violet (UV) spectroscopy in solution[23,24,25] and proton NMR[26] among other studies[27,28,29] suggest a set of equilibriums between polysulfides in solution, showing the complexity of the intermediate states of the system.

The commonly accepted description of the system is mostly based on a mathematical modeling of the galvanostatic discharge.[30] This model – based on solubility constants and reaction rates – gives useful information on the major species present during cycling. By determining the average concentrations of these species, they can model the typical electrochemical signature of the reduction. The first plateau thus corresponds to the conversion of elemental sulfur to linear chain polysulfides, Li_2S_8, Li_2S_6 and then Li_2S_4. The "knee" on the voltage profile is properly reproduced by the maximum of the concentration of Li_2S, around the average concentration Li_2S_4. The second plateau then corresponds to the precipitation of Li_2S_2 and Li_2S from a supersaturated solution. Globally, the discharge behavior proposed can be summarized in three steps:

- The first stage, until the supersaturation point $S^0 \leftrightarrow S^{0.5-}$, leads to the formation of Li_2S_4 via long chain polysulfides Li_2S_8 and Li_2S_6.

- The second stage, $S^{0.5-} \leftrightarrow S^{1-}$, leads to the formation of Li_2S_2

- The last stage is a diffusion-controlled reaction, thus really slow, which leads to the formation of Li_2S.

In fact this is a very simplified description of the complicated electrochemical behavior of the sulfur positive electrode, as illustrated by recent solution studies.[27,28,29] Barchasz *et al.* used UV spectroscopy on a catholyte cell – i.e. completely in solution – to investigate the complex set of equilibriums involved.[23] Noticeably, S_6^{2-} is identified as the major specie on the high voltage plateau. S_8^{2-} is reported to go through a fast dismutation:

$$S_8^{2-} \rightarrow S_6^{2-} + \tfrac{1}{4}S_8$$
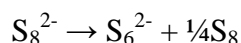
Then S_6^{2-} forms S_4^{2-} at the supersaturation point. S_6^{2-} and S_4^{2-} are reported as the most probable stable polysulfides in solution.[18] The following is a successive reduction of polysulfides that are difficult to distinguish, and ends with S^{2-} (i.e. Li_2S) as expected . Other studies use *in situ* X-ray diffraction (XRD)[31,32,33] or electrochemical impedance spectroscopy (EIS)[34] to try to follow the formation and consumption of solid phases. Noticeably, XRD fails to detect crystalline α-S_8 after a full cycle. It means that if elemental sulfur is formed at the end of charge, it is in an amorphous phase. The use of XRD appears inadequate since most of the species are amorphous. EIS shows that the formation of insoluble Li_2S happens at the very end of the low-voltage plateau, which corresponds to the voltage drop in the voltage profile presented in **Figure 3.**

Interestingly, a first study use X-ray absorption fine structure (XAFS) at the sulfur K-edge to show the reactivity of polysulfides with carbonate solvents. XAFS could be an excellent

spectroscopic technique since it is a local probe and notably elemental sulfur and Li_2S have a complete different spectrum.[35] Also, this study suggests that polysulfides present a clear fingerprint in the low-energy region of the sulfur K-edge, even if reference materials for identifying the signature of Li_2S_n in XANES are not presented.

1.2.3. Strategies to develop the Li-S system as a cogent alternative to lithium-ion batteries.

Many strategies have been adopted to improve the different components of a lithium sulfur cell. This section presents briefly the general ideas developed in the field, focusing on the design of the sulfur host for the positive electrode and on the electrolyte.

1.2.3.1.   Design of the cathode.

The part of the battery that has drawn the most attention is the cathode, i.e. the positive electrode that contains elemental sulfur. The composite needs to be lightweight and conductive in order to "wire-up" the insulating sulfur. Carbon in a multitude of forms has been investigated widely, because it is highly conductive, cheap and light. Other strategies such as porous metal oxide or polymers have been explored, but the use of carbon as an additive or as the main host for sulfur appears to be mandatory.

Most of the recent work using carbon follows the strategy proposed by the Nazar group where sulfur is impregnated into a mesoporous carbon CMK-3.[36] The idea is to contain the sulfur into the porous structure of the carbon host. This confinement hinders the diffusion of soluble polysulfide outside the cathode, hence helping to maintain a high capacity. Many studies investigate the use of porous carbon such as porous carbon spheres[37,38] or hollow carbon

nanofibers, [39,40] playing mostly on the distribution of the size of the pores and on the sulfur loading.

Following this general idea, the impregnation of sulfur into carbon nanotubes has also been studied. The results are more or less convincing. Graphene has also been investigated, even if it does not tackle the issue of polysulfides dissolution. These materials also exhibit a high conductivity and give the opportunity to functionalize their surface.[41,42] Functionalizing the surface of the carbon host is indeed a very promising way to enhance the capacity by providing a favorable hydrophilic interaction with the soluble polysulfides and helping the precipitation of Li_2S. The carbon host can also be coupled with a polymer coating to wrap particles and prevent any loss of active material in the electrolyte.[36]

1.2.3.2. Liquid electrolyte design.

An electrolyte consists of lithium salts dissolved in a solvent. Because most of the sulfur species formed during cycling are soluble in the electrolyte, the selection of the electrolyte appears to be crucial. Linear chain polysulfides are very reactive, and are known to react with most of the common electrolyte solvents, such as esters, carbonates, and phosphates. Also, because of the mobility of Li_2S_n species in the electrolyte,[30] Li-S batteries are subjected to self-discharge, i.e. chemical reactions that reduces the energy stored in the battery without any connection between the electrodes.[43,44]

The common solvents for Li-S batteries are limited to linear and cyclic ethers, such as dimethyl ether (DME) and 1,3–dioxolane (DOL).[45,46,47] Other glymes such as Tetraethylene glycol dimethyl ether (TEGDME) are also reported in the literature.[12] To date, it is not clear if high polysulfides solubility and mobility are favorable for the functioning of the cell. A good

solvent for an electrolyte has to exhibit a low viscosity and a high ionic conductivity. DOL:DME exhibits a viscosity around 2 cP and an ionic conductivity around 11 mS.cm^{-1} for an 1 M concentration of Lithium Bis(Trifluoromethanesulfonyl)Imide (LiTFSI).[48] However, this electrolyte solvent suffers from its low boiling point, making it too volatile for practical use. The salt used is generally LiTFSI in 1 M concentration, even if other salts like $LiPF_6$ have proved their possible utilization.[49]

The use of additives in these electrolytes has been widely studied. They are used to protect the lithium anode, to increase the ionic conductivity of the electrolyte, and/or to play on the dissolution of polysulfides. $LiNO_3$ is nowadays reported in almost all the literature.[50] By forming a very favorable surface layer on the lithium metal anode, the lithium metal is passivated. X-Ray photoelectron spectrometry (XPS) has shown that $LiNO_3$ in solution is directly reduced to form surface Li_xNO_y on lithium metal. In the presence of polysulfides in solution, $LiNO_3$ forms Li_xSO_y.[51] These species passivate the lithium negative electrode, and therefore decrease the possible reduction of soluble polysulfides on the lithium anode. As a result, polysulfides in solution do not react on its surface and the shuttle phenomenon is inhibited. However, $LiNO_3$ gets reduced on the positive electrode at a potential between 1.8 and 1.5 V vs. Li^+/Li^0, giving rise to irreversible capacity during the first cycles. Besides, numerous recent papers investigate the use of polysulfides Li_2S_n as an additive to the electrolyte. [52,53] If the capacity retention appears to be enhanced, some of these papers claim a high gravimetric capacity value but do not take into account the sulfur present in solution. When calculating the gravimetric capacity with all the amount of sulfur (cathode + electrolyte), the actual capacity is much lower indicating that the polysulfides in solution act as a reservoir of electrochemically active sulfur.

1.3. Conclusion.

This chapter was a general introduction of the field of batteries, and more precisely lithium based secondary battery. If lithium-ion batteries exhibit the highest energy and power densities of commercially available devices, the current research is reaching theoretical limits and improvements are less and less expected in terms of energy and power densities. New systems such as lithium-sulfur batteries are expected to take over lithium-ion batteries.

More and more literature exists on the topic. The current research is mostly focused on designing a suitable cathode composite. However, the redox chemistry of sulfur, that involves phase transition, is a severe impediment in order to reach high performances. The electrochemical signature and its modeling have been the basis of most of the understanding of the system for a long time. Now, techniques such as XRD, UV spectroscopy or EIS have been used to investigate deeper the system, but they present inherent limitations that restrict their conclusions. For example, XRD is long-range technique that cannot characterize the amorphous and soluble species formed during the redox process. It is the purpose of this work to investigate the use of local probe, which will be presented in the next chapter, to provide more details on the sulfur chemistry inside a Li-S cell.

2. Techniques used to characterize the Li-S system.

This thesis was devised as a fundamental study of the Li-S system, as a complement to the design and optimization of sulfur-based cathode materials carried out by other and former group members. Therefore, this chapter, describing the methods and equipment, covers not only electrochemical techniques, but also the characterization techniques that were implemented specifically to allow the speciation of sulfur species upon the operation of a Li-S battery.

2.1. Electrochemical characterization.

2.1.1. Design of a coin cell.

The 2325 coin-cell design is shown in **Figure 5**. The cell is contained within two caps of stainless steel that serve both as a sealed container and as current collectors. One of them has a plastic gasket to prevent any electronic contact between them and also to ensure perfect sealing. The cathode composite containing elemental sulfur is drop-cast onto an aluminum current collector, while lithium foil spread on a stainless steel support is used as the negative electrode. Two Celgard® separators – made of microporous polypropylene – are placed between the electrodes to prevent any electronic contact while their porosity ($> 75 \%$) is filled with electrolyte to allow fast ionic conduction. Last, a spring is used to maintain a balanced pressure in the cell. The cell assembly is carried out in an argon filled glovebox with the help of a pneumatic crimper. The advantage of this design resides in the effective sealing maintained during a long period of time, reducing the evaporation of electrolyte and guaranteeing a sufficient pressure. It allows performing long-term cycling. It is also relatively easy to build.

Cap (stainless steel) with plastic gasket

Spring (stainless steel)

Lithium foil on stainless steel

Two Celgard®

Cathode on aluminium foil

Cap (stainless steel)
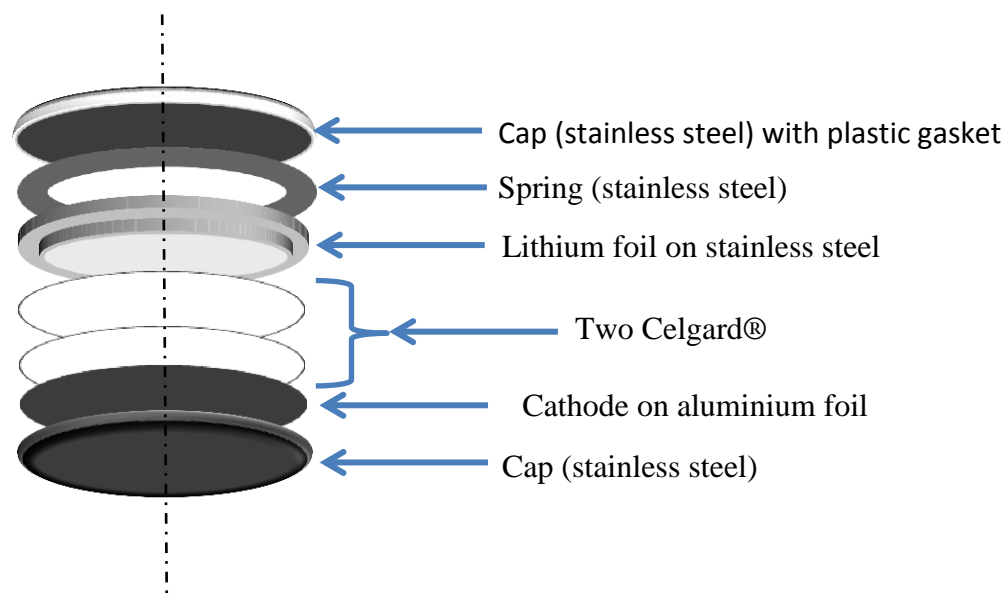
Figure 5. Design of a coin cell. The cartoon is an exploded view of the cell, showing the different parts.

2.1.2. Electrochemical techniques.

2.1.2.1. Galvanostatic Cycling with Potential Limitation (GCPL).

This protocol corresponds to the most standard experiment to study the behavior of batteries upon operation. The performance of an electrode material is determined as a function of its charge and discharge conditions: mainly a given rate (i.e. a constant current), within a given potential range, typically [1.5 V; 3 V] for the Li-S system. The galvanostatic rate is usually expressed as C/h, h being the number of hours at which the nominal charge will be passed through. Here, C is defined as the charge corresponding to the total expected reduction/oxidation of the sulfur-based electrode and hence a 1C rate (1672 mAh.g^{-1}) theoretically enables to fully (dis)charge the battery in one hour (see previous chapter). The most important information obtained from galvanostatic cycling is the voltage-composition relation, as plotted in **Figure 3** for

a typical Li-S cell. Basically a *linear* dependence of the potential vs. composition corresponds to a solid-solution single-phase domain whereas a potential plateau corresponds to a two -phase domain. Additional pieces of information accessible are the rate capability, the charging efficiency and the long term cyclability. These experiments were performed on an Arbin battery tester, mostly at room temperature or sometimes around 60 °C to test the electrolyte tolerance to moderate temperatures.

2.1.2.2. Cyclic voltammetry (CV).

Voltammetry gathers the electrochemical techniques in which the current at an electrode is measured as a function of the potential, or voltage applied. The potential is varied in some systematic manner – in the case of CV a voltage ramp linear with time is used – and the resulting current-potential plot is called a voltammogram. "Cyclic" refers to the inversion of the voltage rate when the potential reaches its lower or upper limit. This potential can be thought of as "electron pressure" which either forces a species to gain or lose an electron (reduction or oxidation). As a result, this technique allows seeing at which voltage the redox reactions happen more clearly than with a galvanostatic measurement. In some cases, electrochemical reaction rates can also be obtained by varying the scan rate.

2.1.2.3. Potentiodynamic Cycling with Galvanostatic Acceleration (PCGA).

This technique is similar to the CV, although more sophisticated. The principle is to scan the voltage window using potential steps, of amplitude dV, while recording the chronoamperometric response. In this mode, the successive steps of potential are applied at fixed time intervals or when the reduction (oxidation) current reaches a predefined value I_{min} which is considered as negligible compared to the capacity of the system (typically C/50 or C/100). The

idea behind this is to let the system relax towards its thermodynamic equilibrium (ideally obtained for $I_{min} = 0$) before changing the potential. Due to the time limit on each step however, I_{min} is not always reached and the thermodynamic equilibrium is not always achieved, but approached. In such case, conditions like $2.5 - 5$ mV/h are reasonable. The chronoamperometric response for each step depends on the nature of the electrochemical reaction that occurs. The curve $i = f(V)$ obtained consists of an incremental capacity voltammogram, obtained with the resolution of the potential step amplitude. It shows much narrower peaks than the one obtained by CV, but the time of the experiment can be really long (1-5 days / cycle). However, contrary to CV, ranges of potential where no electrochemical activity occurs are swept quickly since I_{min} is reached directly.

2.2. Laboratory structural characterization techniques.

In conjunction with the electrochemistry, this research project was focused on the structural characterization of sulfur-based electrodes. As the most common tool used in our lab to characterize solids, X-ray diffraction was a good starting point but its use was limited owing to the nanosized confinement of sulfur in the electrode matrix, and by the amorphous nature of the intermediate species. Therefore, this work was made to investigate the use of short-range spectroscopic techniques on Li-S system namely, X-ray absorption fine structure (XAFS), X-ray Raman Spectroscopy (XRS or Non-resonant inelastic X-ray scattering – NRIXS) and Magic-angle Spinning Nuclear Magnetic Resonance (MAS NMR).

2.2.1. Powder X-ray diffraction.

X-ray diffraction has become one the most common technique to characterize crystalline sample since Laue *et al.* discovered that X-ray radiation could be diffracted by crystals in 1912

because their wavelength is of the same order of magnitude as interatomic distances (10 nm $< \lambda <$ 0.01 nm). In 1913, Sir William Bragg established the law governing the appearance of a diffraction pattern through interference of X-ray reflections from crystal planes:

$$n \cdot \lambda = 2 \cdot d \cdot \sin\theta.$$

It is naturally known as the Bragg's law.[54] n is an integer determined by the order given (n=1 corresponds to the highest intensity), λ the wavelength of the X-ray wave. $2 \cdot d \cdot \sin\theta$ represents the path difference between two parallel waves diffracted by two lattice planes separated by d. If it is a multiple of the incident wavelength, the two waves interfere constructively, as illustrated in **Figure 6**. Due to Bragg's law, each diffracted peak can be associated to a "d spacing".

$$n.\lambda = 2.d.\sin(\theta) \equiv \text{constructive interferences}$$
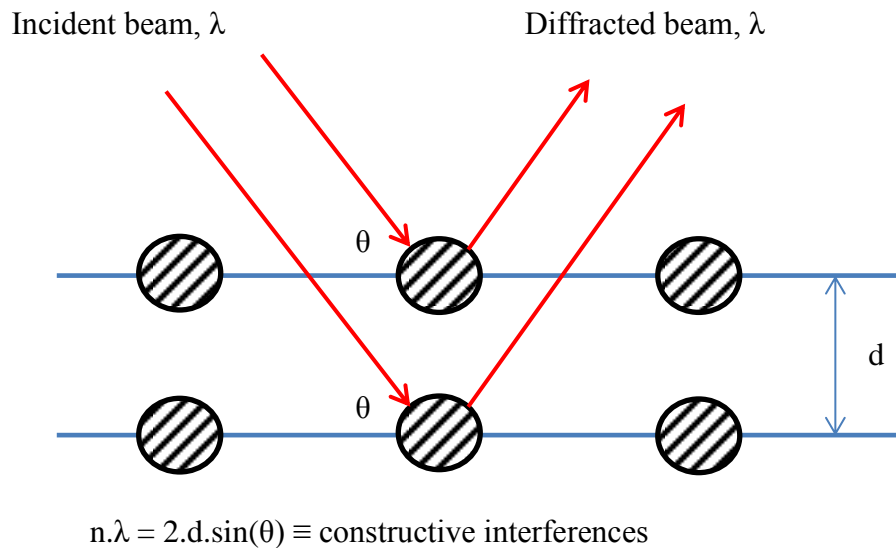
Figure 6. Illustration of the Bragg's law.

Thus, the method consists in scanning the sample over an angular range and measuring the diffused intensity in term of special orientation. Our diffractometer is set up on a "θ-2θ"

configuration which means that both the sample and the detector move to change the orientation vs. the incident beam. Powder samples usually exhibit rich and complex diagrams. Any possible crystal orientation gives rise to diffraction corresponding to each *d* spacing present. Interestingly, the area under all the peaks corresponding to a given crystalline phase is directly proportional to the weight percent of this phase in the powder sample. This phase can be made of crystal domains coexisting with amorphous domains. Also, the peaks widen as crystallite size decreases (typically less than 1 μm) due to the existence of constructive interference at small deviation from Bragg's condition. The Scherrer equation relates the broadening of diffraction lines with crystal size:

$$L = \alpha \cdot \lambda / (\beta \cdot \cos\theta)$$

Where L is the coherence length of the crystal domain, β is the full width in radians at the half maximum intensity measured at θ, α is a constant close to unity. It gives a good approximation of crystallite size in the sample, and along with the integrated intensities, opens the way to quantitative phase analysis providing a careful calibration.

Powder X-ray diffraction (PXRD) patterns were collected using a Bruker D8-Advance powder diffractometer equipped with a Vantec-1 detector, using Cu-Kα_1 radiation (λ = 1.5406 Å). Air-sensitive samples were mounted on a sealed holder comprising a Kapton window to allow X-ray penetration while avoiding any exposure to air during the measurements.

2.2.2. Magic-angle spinning nuclear magnetic resonance (MAS NMR).

Nuclear magnetic resonance is a technique of spectroscopy that detects re-emitted electromagnetic radiation from nuclei placed in a magnetic field. Nuclei that exhibit a nonzero spin **I** can be treated as small magnetic dipoles with an intrinsic magnetic moment $\boldsymbol{\mu} = \Upsilon . \hbar . \mathbf{I}$ where

Υ is the gyromagnetic ratio of the investigated NMR isotope, and $\hbar$ the reduced Planck constant. ^7Li exhibits a spin of 3/2, and it constitutes the most abundant isotope of natural lithium (92.4%), making ^7Li NMR experiments relatively easy to carry out.

In the presence of an external field $\mathbf{B_0}$, the nuclear spins align either with or against the magnetic field because of the Zeeman interaction between $\mathbf{B_0}$ and $\boldsymbol{\mu}$. It provides an energy of $E=\boldsymbol{\mu}.\mathbf{B_0}$. The different $2I+1$ nuclear spin states have an energy of $E_m= -m.\Upsilon.\hbar.B_0$ where m is the magnetic quantum number, and the difference between two adjacent states is $\Delta E=\Upsilon.\hbar.B_0$. In a typical NMR experiment, the sample is subjected to a permanent external magnetic field $\mathbf{B_0}$ that aligns the magnetic nuclear spins. The macroscopic magnetization $\mathbf{M}$ is set parallel to $\mathbf{B_0}$. A perturbation is then performed by applying a radio frequency magnetic field $\mathbf{B_1}$ perpendicular to $\mathbf{B_0}$. When applying this pulse, $\mathbf{M}$ starts precessing around B_0, this phenomenon is called the Larmor precession. Resonant absorption by nuclear spins will occur when the frequency of $\mathbf{B_1}$ is set to match ΔE. Transitions between adjacent states are then possible; and the time dependant relaxations of the magnetic nuclear spins, which occur after the pulse, are the phenomena exploited in NMR spectroscopy. The NMR relaxations can be distinguished using two relaxation times: one in the plane perpendicular to $\mathbf{B_0}$ (plane of $\mathbf{B_1}$), T_2, , known as the spin-spin relaxation time, that corresponds to the decay of the magnetization in the plane transverse to B_0, and one along B_0, T_1 that corresponds to the time necessary to recover $\mathbf{M}$ along $\mathbf{B_0}$.

The signal emitted during the return to equilibrium is known as the Free induction Decay (FID). The oscillations of the magnetic nuclear spins induce an oscillating electrical current created in the reception/emission coil. The precession of each nucleus depends on the total magnetic field experienced, which contains the external $\mathbf{B_0}$ but also the local magnetic fields induced by electrons − which have a magnetic moment − in the molecular orbitals surrounding

the nucleus. Therefore, a deviation from the Larmor precession is observed depending on the local electronic environment surrounding the atom, it is called the chemical shift. The induced electrical current can be decomposed into a sum of simple oscillating function with different frequencies that come from the different chemical shifts in the sample. The NMR spectrum is the result of applying a Fourier transform to the FID, i.e. extracting the characteristic frequencies of the signal. Each electronic environment give a particular signature – a peak at a distinct frequency – on the spectrum obtained, which is used to differentiate between chemically non-equivalent sites.

One of the most important aspects of solid-state NMR is the orientation dependence (i.e. anisotropy) of the interactions involved between the nucleus and its environment. This anisotropy leads to a substantial loss of spectral resolution due to broadening of the spectrum. A common way to tackle this problem is to use the Magic-Angle spinning configuration. It introduces an artificial spinning motion of the sample at the *magic* angle 54.74° with respect to $\mathbf{B_0}$. At this angle, which is the solution of $3.\cos^2\theta - 1 = 0$, the anisotropic terms can be averaged if the frequency of the precession is greater than the one of the anisotropic interaction.

To summarize, MAS NMR provides information about the local environment of the emitted atom. Because most of the species present in a Li-S cell – (dis)charge products, intermediate polysulfides Li_2S_n – are invisible to long-range technique like XRD, ^{7}Li MAS NMR can provide very useful information. In this work, ^{7}Li NMR experiments were carried out on a Bruker Avance-500 (11.8 T) at the University of McMaster, with a MAS frequency of 30 kHz.

2.3.Synchrotron techniques.

The emergence of synchrotron facilities has opened the way to use high intensity, high stability, monochromatic X-rays beam for a wide range of energies. The energy of the x-ray photons (100 eV < E < 100 kev) is of the order of binding energies of core-level electrons. Therefore, X-rays can be used to interact with core-level electrons. X-ray absorption fine structure (XAFS) and the X-ray Raman spectroscopy (XRS) are atomic probes that are sensible to the electronic state of the atom probed itself, and to its close environment. They differ by the energy range used and the interaction *beam-atom* involved. In addition to NMR, they constitute therefore two of the few structural probes available for non-crystalline and highly disordered materials. Also, X-rays are expected to penetrate in matter (it may require special care in the experiment design), so that XAFS and XRS are bulk-sensitive probes as well. In contrast with NMR however, X-ray spectroscopy is not restricted to a few isotopes and instead can be used on essentially every element on the periodic table. Interestingly, XANES used before for *in situ* studies of transition metal oxide used as a cathode in a lithium-ion and organo-sulfides batteries.[55,56]

2.3.1. X-ray absorption near edge structure (XANES).

2.3.1.1. X-ray absorption fine structure (XAFS).

XAFS allows following the evolution of the x-ray absorption probability or absorption coefficient, μ, of a specific atom while the energy of the incident beam energy is scanned. This technique consists of sending a monochromatic X-ray beam a sample to excite particular core-electron and to measure μ by collecting the transmitted beam. The formula $I = I_0 e^{-\mu x}$ gives the direct link between the intensity of the incident beam I_0, the transmitted intensity I and μ. An

important point is that μ is highly dependent of Z, the atomic number. It is therefore easy to achieve good contrast between different atoms.

As we mentioned, energy of X-ray photons is of the order of binding energies of core-level electrons. XAFS refers to how x-rays are absorbed by an atom at energies around its core-level binding energies. The simple mechanism is presented on **Figure 7.a.** When an X-ray beam is sent on an atom with an energy corresponding to the transition of one of its core electron to continuum, there is a sharp rise in absorption called an absorption edge. This transition is ruled by the dipole selections rules which limit the allowed transition. The most intense transition in terms of probability is due to electric-dipole transitions to unfilled orbitals ($\Delta l = \pm 1$, l is the second quantum number). It means that for transitions at the K edge, the transition 1s → np is the most intense. The atom is then in an excited state with a hole which eventually decays to reach equilibrium. This decay mostly proceeds through two main mechanisms, the X-ray fluorescence and the Auger Effect (**Figure 7.b**). During fluorescence, a higher energy electron fills the core hole formed by the absorption of the X-ray. The frequency of the wave emitted during this process is proportional to the one absorbed, and is therefore specific to the atom. The Auger Effect happens when an electron filled the core hole and another electron is emitted in the continuum, or even outside the sample. Recording the fluorescence emissions or the Auger electron outside the sample are two ways to measure the absorption coefficient since they can reasonably be considered as proportional to the absorption coefficient.
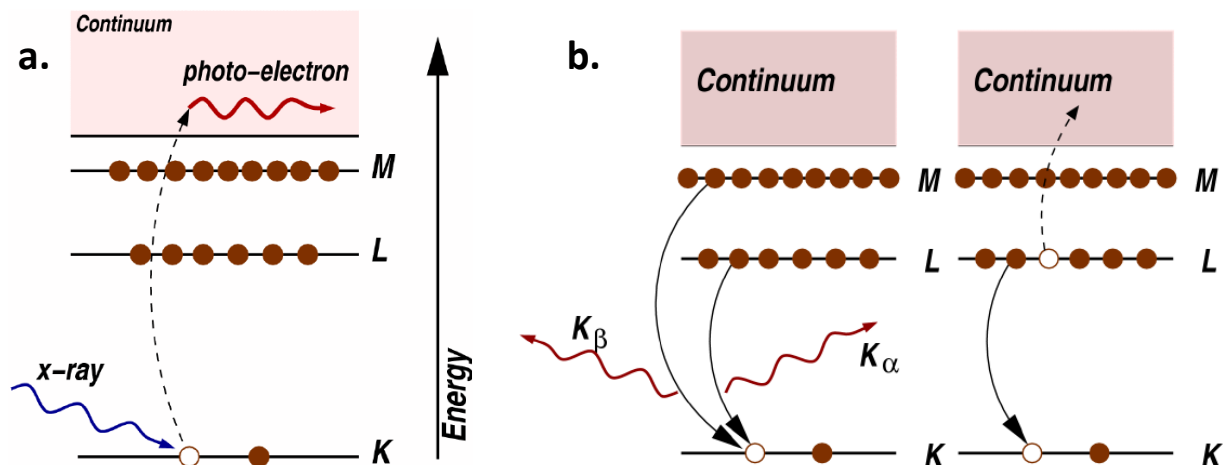
Newville, M. Fundamentals of XAFS. *Consortium for advanced radiation sources* (2004)

Figure 7. a. Schematic of the mechanism involve in the creation of a photo-electron. **b.** Left: relaxation by fluorescence emission. Right: Relaxation by the Auger Effect reproduced from ref. 57.

If the incident energy is less than the binding energy, the electron stays in its well-defined quantum state and no x-ray is absorbed. Any excess energy (still compared to the binding energy) is given under the form of kinetic energy to a photo-electron, which is the electron that has been excited. When a neighboring atom is included in the picture, this photo-electron can scatter elastically from the electrons of this neighboring atom and return back to the absorbing atom. It creates an interference effect that will alter the absorption coefficient, and it gives rise to modulations in the spectrum recorded. The actual probe used in XAFS is the photo-electron. Its mean-free path is around 25 Å (it depends on the incident energy), making XAFS a local atomic probe.

A typical XAFS spectrum is presented in **Figure 8**. μ_0 is the background function representing the absorption of an isolated atom and $\Delta\mu_0$ the edge-step. The spectrum recorded consists of μ_0 affected by modulations arising from the scattering of the photoelectron. Three regions can be identified:

- At low energy, before the edge E_0, the energy of the incident photon is too low to give rise to any transition

- Around E_0, the absorption coefficient increases drastically, giving rise to an "edge". The energy of the electron is transferred to the core electron to reach the first available state present. This region is called X-ray absorption near edge structure (XANES) and is strongly linked to the atomic or local characteristic such as coordination chemistry, molecular orbitals or the band structure of the atom. The theory behind XANES is the most difficult part to interpret in a spectrum.

- From few eV to hundreds of eV, the domain is called Extended X-ray Absorption Fine Structure (EXAFS). It corresponds to a decrease of μ with some modulations. The photo-electron explores the environment with a kinetic energy given by the excess energy of the incident beam regarding E_0. A well-established theory allows obtaining several characteristics of the local environment such as the number of neighbors as well as bond distances and angles.
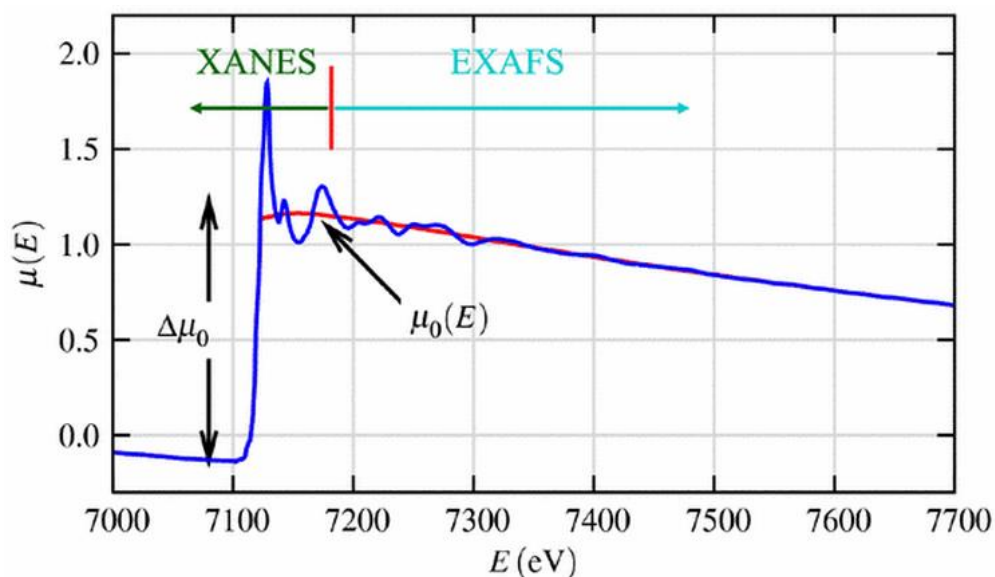
Figure 8. Typical evolution of the absorption at one edge showing the XANES and EXAFS regions reproduced from ref. 58.

The fundamental origin of EXAFS and XANES is basically the same, but several approximations are applicable in the EXAFS range; which permit an easier modeling and quantitative analysis. The most important difference is that for XANES (*low* E, *high* λ) multiple-scattering (i.e. scattering involving several atoms) has to be taken into consideration while for EXAFS (*high* E, *low* λ) single-scattering (i.e. scattering involving one atom) can be sufficient. There is no simple equation for XANES, and it is therefore mostly a finger-print technique. However, XANES spectra are much easier to acquire since the background contribution compared to the signal is significantly lower near the edge compared to the extended region. The feature is intense and concentrated on a small energy range which makes it faster to collect.

All the X-ray absorption data presented in this thesis were collected at the Advanced Photon Source in Argonne National Lab. (USA, IL). Indeed, only synchrotron radiation can

31

provide the sufficiently intense and energy-tunable source of x-rays necessary to carry out XAFS. The experiments were performed at the sector 9-BM-B where the instrumental resolution in the energy range near sulfur K-edge is theoretically about 0.35 eV, with a beam size of about 450 x 450 micrometers.

2.3.1.2.   Experimental setup.

2.3.1.2.1.   *Beam line setup.*

Measurements were performed in Argonne National Laboraty at the sector 9-BM-B. The instrumental resolution in the energy range near sulfur K-edge is theoretically about 0.35 eV, with a beam size of about 450 x 450 micrometers.
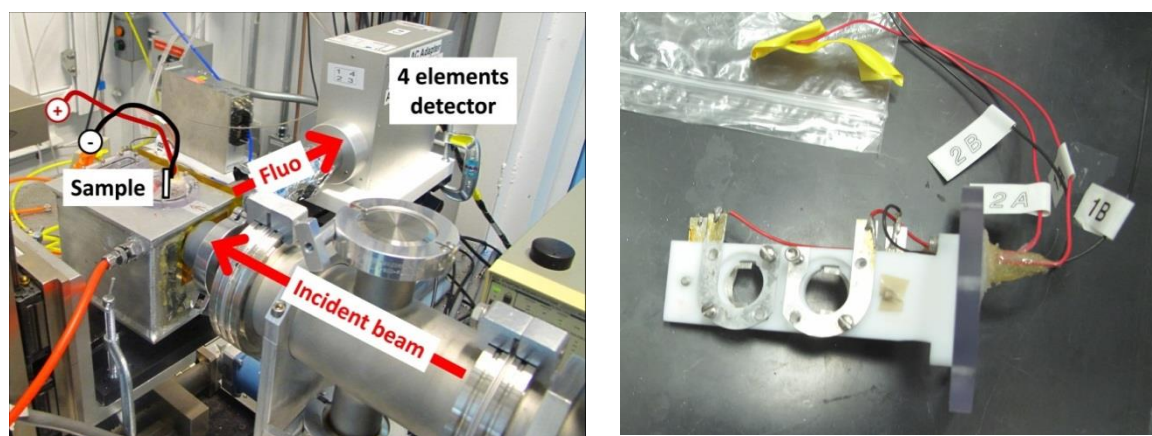
Figure 9. Experimental set-up use and sample holder.

Figure 9 shows a picture of the experimental setup. All of the XANES studies were carried out under constant helium flow in the sample chamber, since the penetration depth of X-rays at sulfur K-edge energy is around 12 meters in helium while it is only around 1 cm and 2 cm in O_2 and N_2, respectively.[59] The sample was put on a specific older (**Figure 9**, right) that has two electrical cables to plug a battery. The data were collected in fluorescence mode using a 4-

element vortex detector. The angle between the sample and the incident beam was kept close to 45°.

The design of the *in situ* cell is presented on **Figure 10**. Basically, it is a standard 2325 coin cell with a Kapton™ window on the side of the cathode. Kapton™ is made of polymide and exhibits an attenuation length around 25 μm at the sulfur K-edge energy.[59] Aluminized Kapton™ was used to prevent any leak since the electrolyte is very volatile. The active material was put on a carbon paper so that it can face the window. Contrary to usual aluminum current collector, the porosity of carbon paper allows the necessary migration of ions. Several tests on standard materials were made to prove that this cell behaves exactly the same as a conventional coin cell. This good behavior is shown later in this thesis (4.2.1.1).
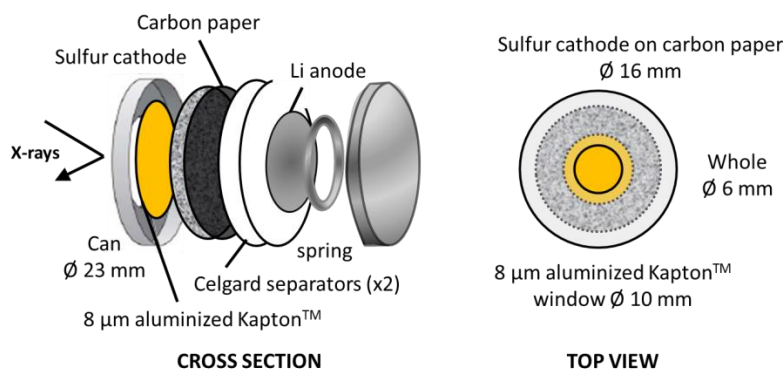
Figure 10. Schematic of the *operando* cell. The design was adapted from a 2325 coin cell, using an aluminized Kapton™ window to allow X-ray beam penetration.

33

2.3.1.3.   XANES data analysis.

2.3.1.3.1.   *Computational model.*

XANES is difficult to predict but different theoretical approaches and formula are implemented in a variety of softwares to try to model the spectra *ab initio*. For example, the FEFF code is based on the Muffin-tin approximation that attributes spherically symmetric potentials to the atoms. This code is the most *user-friendly*, while it still allows playing on different parameters. The FDMNES code is based on the Finite Difference Method to solve the Schrodinger Equation with or without the Muffin-tin approximation. Others code such as EXCURVE or MXAN exist. These codes require the position of the atoms as an input, and are often used after an initial molecular simulation, or structure optimization.

2.3.1.3.2.   *Calibration, normalization, correction of experimental.*

During a run at the synchrotron, a particular attention has to be paid to the calibration of the incident energy. One has to remember that the energy fine-tuning is performed mechanically by the rotation of the double crystal monochromator; therefore this one should return to the same starting angle after each measurement. However, the proper position can be lost because for a number of reasons (temperature, motor…). It is critical that different samples are all measured in the exact same conditions in order to interpret them. At the beginning of each run, or after a beam shut-down, a reference standard is measured in order to set the absolute value of energy. For sulfur K-edge, a common reference standard is sodium thiosulfate pentahydrate $Na_2S_2O_3,5H_2O$ where the pre-edge feature is set at 2469.2 eV.

After acquisition, all the experimental spectra are corrected by subtracting the baseline in the pre-edge and the EXAFS regions and normalized by the edge-step. This operation allows the

quantitative comparison between two different spectra; and proper data analysis relies on the careful attention paid to this steps.

2.3.1.3.3.   Data analysis.

Unlike EXAFS, a XANES spectrum does not require any mathematical transformation to be understood and interpreted. The different features of a spectrum can be fitted with a set of Gaussian and arctangents functions. The spectral features of a compound can be ascribed to Gaussian functions; however, quantitative comparison in a phase mixture is difficult. The fractional amounts of the different phases are not directly proportional to the relative areas of each Gaussian. Scaling factors accounting for the change in absorption cross-section between phases are required.[60] The data analysis can also be based on a linear combination of proper reference spectra, i.e. fingerprints. In this case, prior knowledge of the system is required to choose the appropriate references. Providing that the reference spectra are recorded in the same conditions (beam, calibration, dilution…), a linear combination fit can quantitatively give the composition of a phase mixture.

In the present work, ATHENA™ software was used to perform the data processing, including background subtraction and spectra normalization.[61] The same software was used for the data analysis, either to fit the spectra with a set of Gaussians and Arctangents or to perform linear combinations with a set of reference compounds sequentially on a large number of experimental spectra.

2.3.2. Non-resonant inelastic x-ray scattering (NRIXS).

Non-resonant inelastic scattering of x-rays (NRIXS) is also known as X-ray Raman scattering (XRS) due to its analogy to Raman scattering in optical spectroscopy. Similarly to

XAFS, XRS is based on the interaction of a photon with the electronic structure of the sample. In this technique the process of inelastic non-resonant scattering is involved. **Figure 11** (left) shows the difference between resonant and non-resonant scattering. Non resonant-scattering occurs when the interaction between the atom and the radiation excites the electrons to an unstable virtual state. The interaction is almost immediately discontinued and the radiation is scattered at the same energy and the same momentum (elastic, $\mathbf{q} = 0$ and $\omega_1 = \omega_2$) or at a slightly different energy and different momentum (inelastic, $\mathbf{q} \neq 0$ and $\omega_1 \neq \omega_2$) than the incident radiation. When the energy of the incident X-ray photon is close to a core-electron binding energy, resonant scattering occurs. It can also be inelastic or elastic. Non-resonant inelastic scattering can be divided into two regimes: the low-momentum transfer regime vs. the regime of high momentum and energy transfer (Compton limit). X-ray Raman scattering is a special branch of NRIXS since it is related with excitation of inner shell electrons rather than valence electrons. The inelastic excitation and scattering of valence electrons is referred to Compton scattering. It makes XRS really similar to a soft X-ray absorption technique but with the great advantage that it can be performed using hard – and deep penetrating – X-rays event with low-Z elements such as lithium.
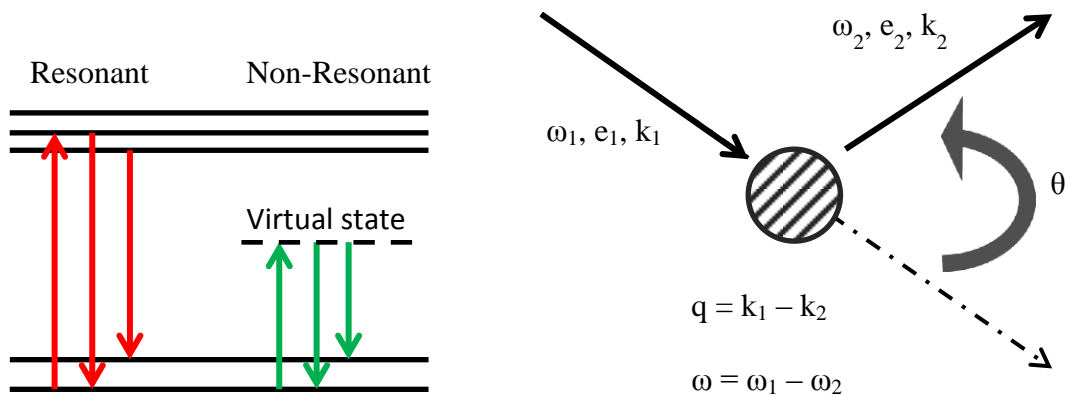
Figure 11. Left: schematics or Resonant (red) and Non-Resonant (green transition. **Right:** Schematic of the interaction of a photon (k_1, ω_1, e_1) and an atom that gives rise to a scattered photon (k_2, ω_2, e_2)

with a transferred momentum q.

The basic kinematics of an inelastic scattering experiment is sketched in **Figure 11** **(Right)**. A photon of energy $\hbar\omega_1$, polarization $\mathbf{e_1}$, and wavevector $\mathbf{k_1}$ interacting with an atom is scattered by an angle θ into a photon of energy $\hbar\omega_2$, polarization $\mathbf{e_2}$, and wavevector $\mathbf{k_2}$. Both the energy and the momentum are transferred to the target. Noticeably, the momentum transfer $\mathbf{q}$ depends on the scattering angle such as $\mathbf{q} \approx 2.\mathbf{k_1}.\sin(\theta/2)$. It allows playing with both the energy and the momentum by tuning the incident beam energy and the solid angle of the scattered beam. In a typical NRIXS experiment, one measure the double differential scattering cross-section, which is the ratio of the current of photons scattered into the solid angle element and into the of range of energy chosen over the current density of the incident photons. It is by tuning the magnitude of $\mathbf{q}$ and ω that one can distinguish between the different types of non-resonant inelastic scattering. X-ray Raman scattering regime is obtained for $\{qa \leq 1, \hbar\omega \approx E_B\}$ where a is the inner-shell orbital radius and E_B the binding energy of that orbital. If NRIXS measurements are frequently used as a bulk-sensitive alternative to traditional soft X-ray absorption spectroscopy, it can also provide an important extension to it. New selection rules can dominate NRIXS depending on the momentum transfer. Such situation is mostly met at high momentum transfer. A drawback of NRIXS is that the cross-section of common atoms in this regime is many orders of magnitude smaller than for corresponding resonant scattering process and for XAFS. As a result, it is more difficult to deal with the background and high concentration of active material is needed.
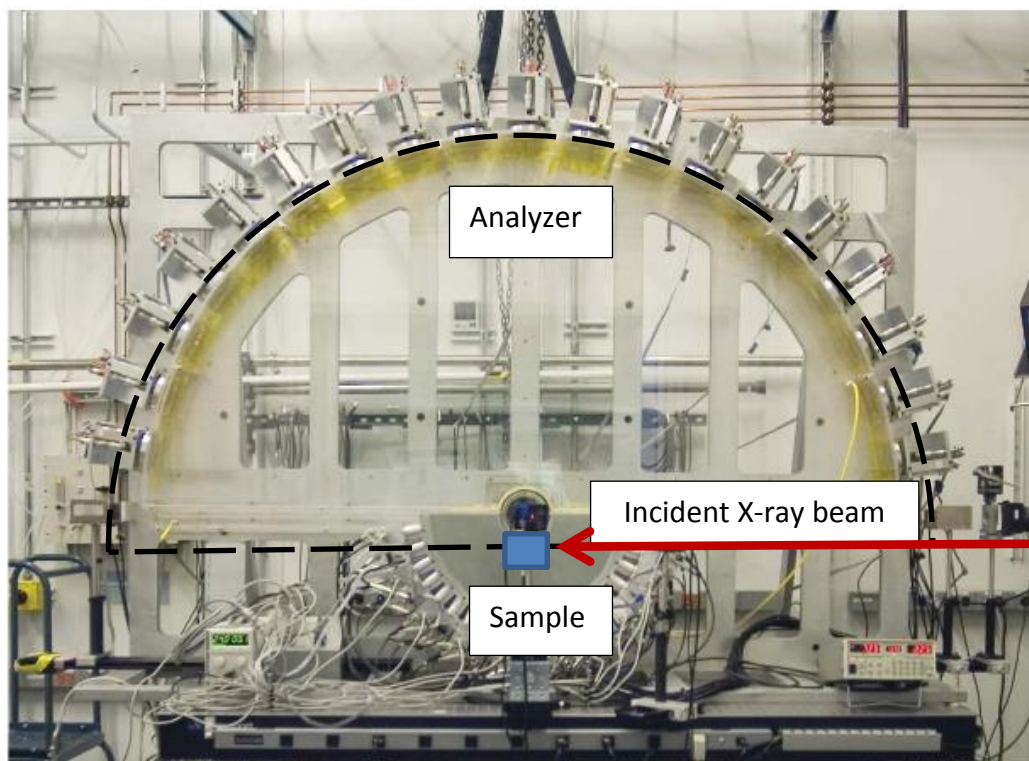
Figure 12. Lower Energy Resolution Inelastic X-ray scattering (LERIX) instrument designed to use NRIXS. The circular arc is made of 19 analyzer crystal modules which correspond to different different momentum transfer.

The Lower Energy Resolution Inelastic X-ray scattering (LERIX) instrument stationed at sector 20-ID at the Advanced Photon Source in Argonne (see the picture in **Figure 12**) was designed for and is dedicated to this type of spectroscopy and in particular to perform studies of q-dependent NRIXS with around 1 eV energy resolutions. The incident beam is indicated by a red arrow. When scattered by the sample, the wave propagates toward different angles corresponding to different momentum transfers. The LERIX detector is made of 19 analyzer crystal modules that are positioned in a circular arc, covering a total q-range from 0.8 to 10 Å^{-1}. This kind of set-ups allows to measure dipole-forbidden final states that are invisible to XAFS. In **Figure 12**, the high q values are obtained on the right side of the instrument ($\theta > \pi$) while low q values are obtained on the left side ($\theta < \pi/2$).

2.4. Conclusion: comments on the methodology of this work.

After a first description of the electrochemical techniques and equipment used, this chapter aimed to present the particular techniques that make the basis of this work on the fundamental chemistry involved in a Li-S cell. XRD is used as a routine technique that is usual in the Nazar group. However, amorphous species cannot be identified. In contrast, XANES, and XRS can characterize the local environment. They constitute a novel approach that has the ambition to characterize the Li-S system. These spectroscopic techniques present the great advantage to probe the matter at the atomic scale, making possible the characterization of the amorphous and highly disordered species possibly formed during the redox chemistry of elemental sulfur. However, they are based on the use of spectroscopies – high field NMR, synchrotron – that are not common in our group and available at the University of Waterloo. All the work depends on the correct utilization and understanding of this novel approach. On top of that, to perform such experiments, time slots have to be asked at different facilities; therefore a careful design and experimental procedure is needed.

3. Synthesis and characterization of solid-state polysulfides A_2S_n (A = Li, Na).

In a Li-S cell, the reduction of elemental sulfur to lithium sulfide proceeds through the formation of several polysulfides Li_2S_n that play a key role in the redox mechanism. Due to their high solubility in most of the electrolyte solvents used, their formation involves a phase transition and their reduction to insoluble Li_2S a second one. Studies based on UV spectroscopy or electrochemical measurements on lithium polysulfides solution showed a complex set of equilibriums.[23-29] To understand the functioning of a lithium-sulfur cell, a better characterization of lithium (poly)sulfides is mandatory. Their solubility, ionic conductivity, and effects on the viscosity of the electrolyte constitute as many parameters that affect the functioning of the cell. In the perspective of using spectroscopic tools such as XANES or XRS to study the redox mechanism involved, isolating stable linear chain polysulfides is crucial to obtain clear fingerprints. While Li_2S is a well characterized commercialized material, Li_2S_n compounds with n > 1 have not been isolated in solution and, unlike sodium (or potassium) polysulfides,[26] no Li_2S_n phase has ever been reported in the solid state .

3.1. Lithium-sulfur and Sodium-sulfur systems.

3.1.1. Li-S system.

The Li-S phase diagram has been reported in different papers, and a representative example is shown in **Figure 13**. Overall, the literature on the Li-S binary system does not mention any stable intermediate between elemental sulfur and lithium except for Li_2S. A monotectic point was found for a Li:S ratio corresponding to "$Li_2S_{3.4}$", but difficulties were

reported to isolate the solid phase that appeared to be unstable and rapidly turned to a mixture containing Li_2S.
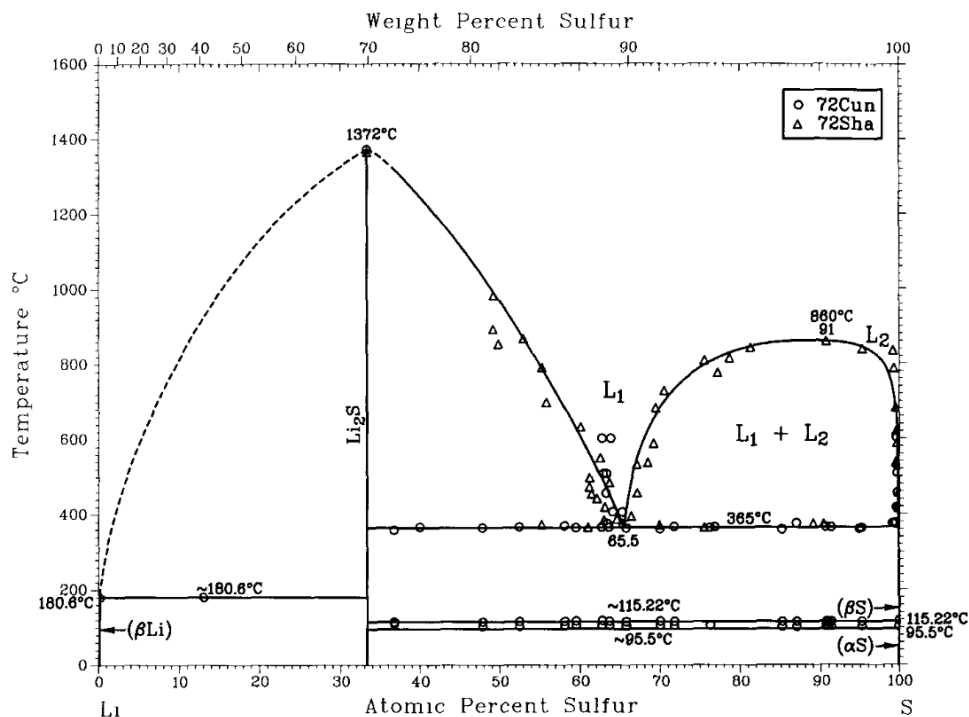
Okamto, H. The Lithium-Sulfur System. *J. Phase Equilibria*, **16**, 94-97 (1995)

Figure 13. Assessed Li-S phase diagram. Between pure lithium (left) and pure sulfur, only lithium sulfide Li_2S could be stabilized as an intermediate solid-phase. Reproduced from ref. 62.

Polysulfides ions, S_n^{2-} (8 < n < 3), have also been studied in solution. In 1977, R.D. Rauh *et al.* reported a complete study of the formation of lithium polysulfides in aprotic media.[63] They showed the existence of a multiple set of equilibriums between the different S_n^{2-}, with noticeably the formation of the radical $S_3^{\bullet-}$. They compared different solvents and tried to figure out which Li_2S_n they had formed by U.V. absorption, starting with a ratio of S_8 and Li_2S. The results emphasized the differences in terms of polysulfides solubility between solvents based on their dielectric constant and their basicity.

U.V.-visible absorption spectroscopy is a common tool to determine the oxidation state of sulfur in solution and more recently, C. Barchasz *et al.* used it on a catholyte cell to investigate the sulfur redox mechanism.[23] They showed that at all time, different polysulfides are present in equilibrium with, noticeably, S_6^{2-} identified as a stable specie for a polarization of 2.4 V, corresponding to the first plateau of discharge in a galvanostatic measurement. S_8^{2-} is reported to go through a fast dismutation: $S_8^{2-} \rightarrow S_6^{2-} + \frac{1}{4}S_8$. U.V. absorbance spectra are sometimes difficult to analyze because the peaks are quite close between two S_n^{2-}, and especially because the assignation of the peaks is under controversial debate.[63] Other studies use electrochemical

$$S_n^{2-} + 2\ CF_3SO_3CH_3 \rightarrow CH_3S_nCH_3 + 2\ CF_3SO_3^-$$
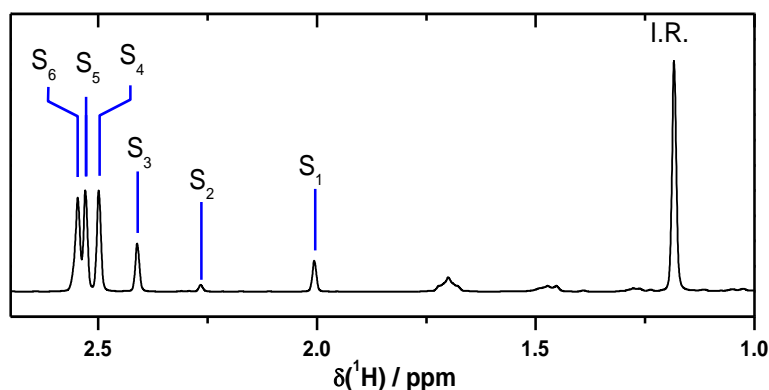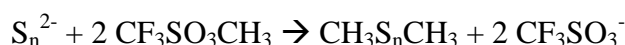
Figure 14. ^{1}H NMR spectrum of a solution of $CH_3S_nCH_3$ with 1,3,5-tributyl benzene in CDCl$_3$ used as an internal standard (IS).

Interestingly, D. S. Argyropoulos *et al.* reported the use of ^{1}H NMR to characterize polysulfides in solution after their methylation.[26] A first step consists in adding a methyl group at each end of the anion S_n^{2-} with a methylation agent, methyl trifluoromethaesulfonate (MeTf):

On the NMR spectrum, the displacement depends on the chain length, n, leading to a quantitative measurement of the distribution of S_n^{2-}. Proton NMR performed on the solution

obtained leads to a spectrum with multiple displacements, i.e. the signature of different S_n^{2-}, as shown on **Figure 14**. This technique will be detailed more precisely later in this report, but it also supports the multi-equilibrium of polysulfides in solution.

3.1.2. Na-S system.

As depicted in **Figure 15**, the Na-S phase diagram is way richer than the Li-S one. Compounds such as Na_2S, Na_2S_4 or Na_2S_5 have been stabilized. Their synthesis has been described in the literature and they are characterized by their XRD patterns.[26] In the perspective of spectroscopic studies, this makes sodium polysulfides a good alternative to their lithium analogues.
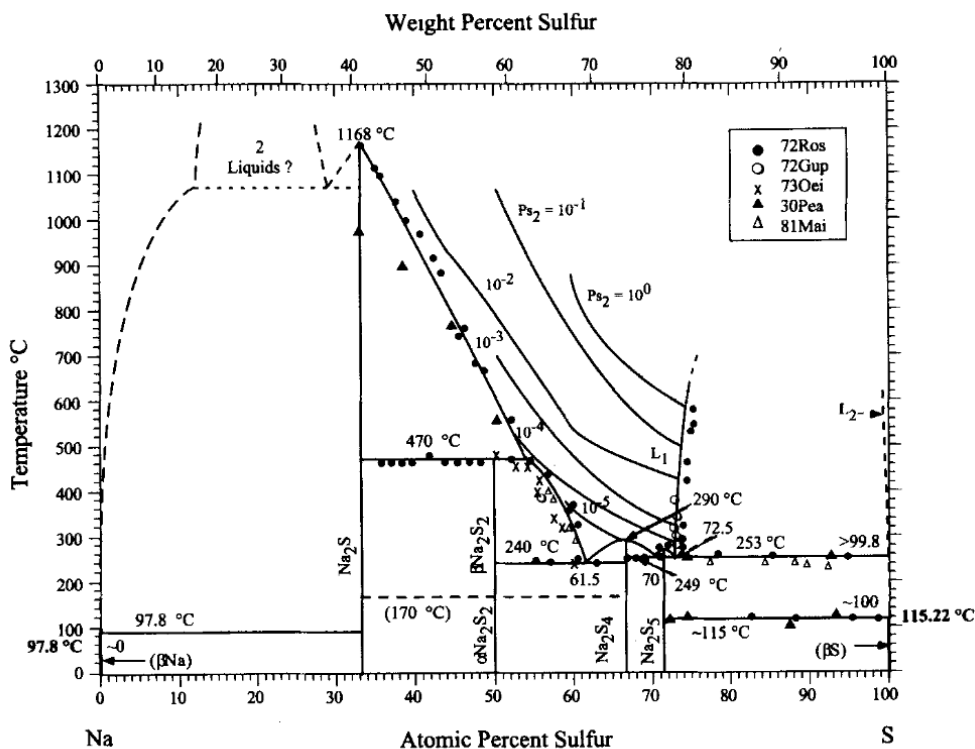
Sangster, J. & Pelton, A. D. The Sodium-Sulfur system. *J. Phase Equilibria*, **18**, 89-96 (1997)

Figure 15. Assessed Na-S diagram reproducted from ref. 64.

3.2. Synthesis of lithium-polysulfides.

3.2.1. Methods followed to synthesize solid state Li_2S_n.

Lithium polysulfides were synthesized using the reduction of elemental sulfur in THF by lithium triethylborohydride ($LiEt_3BH$, a.k.a. Super Hydride) as previously described in the literature.[65] The one-step synthesis was carried out under argon atmosphere and the solvent was then removed by vacuum drying. The route is shown in **Figure 16**. The ratio Li:S was tuned in a systematic fashion to aim a collection of Li_2S_n ($1 \leq n \leq 8$). Interestingly, the color of the solution and of the powder recovered depends on the ratio itself, from white for Li_2S to orange for "Li_2S_8".
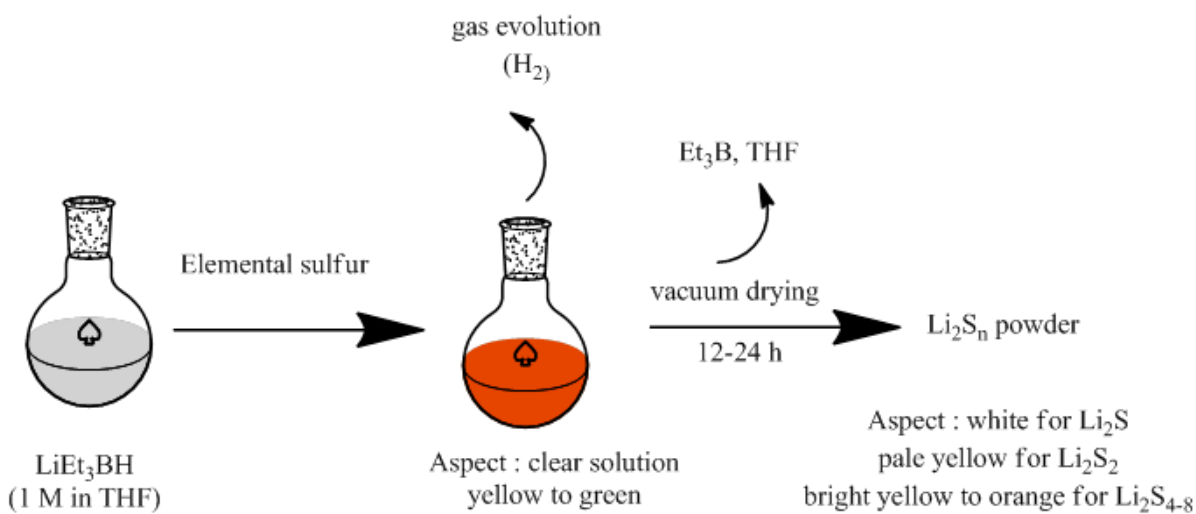
Figure 16. Synthesis of lithium polysulfides performed. First, Super Hydride and element sulfur reacts in THF; and then, the solvent is removed by vacuum drying. The ratio Li:S is tuned to aim a collection of Li_2S_n ($1 \leq n \leq 8$).

3.2.2. Characterization of as-synthesized lithium polysulfides

3.2.2.1. Colors in DOL:DME : change in the "average" oxidation state?

A first preliminary way to characterize our samples was to test their solubility in DOL:DME(1:1). Linear chain polysulfides are expected to be highly soluble in such solvents while elemental sulfur and Li_2S exhibit a low and negligible solubility, respectively. Also, the color of the solution should change with the chain length of the polysulfides in solution. Around 10 mg of as prepared lithium (poly)sulfides – Li_2S, "Li_2S_2", "Li_2S_4", Li_2S_6, and "Li_2S_8" - were put in 2 mL of DOL:DME(1:1). A picture of the vials is shown in **Figure 17**. A precipitate identified by XRD as Li_2S (black arrow on **Figure 17**) was observed in all the cases except for Li_2S_6. It is a strong suggestion that "Li_2S_2", "Li_2S_4", and "Li_2S_8" consist each in a phase mixture containing Li_2S. The absence of any precipitate in Li_2S_6 is a good sign that neither Li_2S nor α-S_8 is present in this compound.
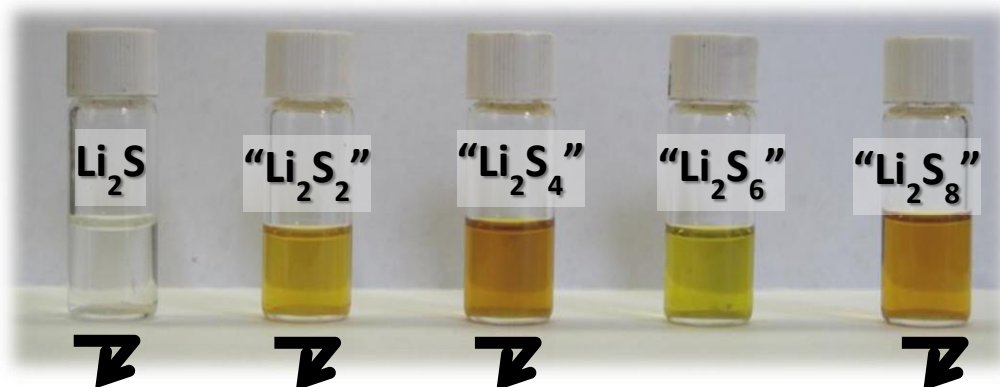
Figure 17. Picture of the different polysulfides dissolved in DOL:DME (1:1). The arrow under the vials indicates the presence of a precipitate. No precipitate could be seen for Li_2S_6.

3.2.2.2. Powder XRD characterization.

As-synthesized lithium (poly)sulfides powder samples were subjected to XRD, as illustrated in **Figure 18**. A TiO_2 anatase internal reference was used to compare the degree of crystallinity of the samples. Diagrams shown in **Figure 18** were therefore normalized accordingly. Results, summarized in **Table 2,** suggest that the only targeted composition successfully reached is Li_2S_6, although the poor signal to noise ratio may hide a small contribution of elemental sulfur. Due to its amorphous state XRD alone cannot give any further indication regarding its structure. Lithium sulfide synthesized with the same procedure is nanosized with coherent domains of 9 nm in average, while 40 wt% of the material is X-ray amorphous. "Li_2S_2" exhibits the clear presence of a Li_2S component, while element sulfur diffraction peaks are observed in "Li_2S_8".
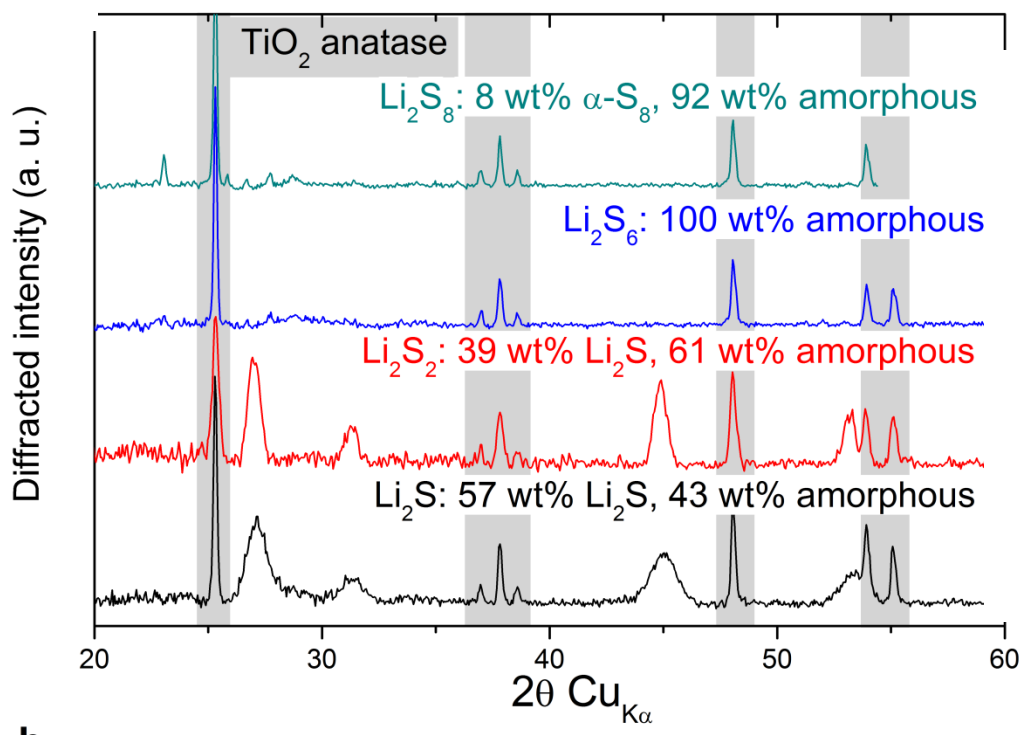
Figure 18. XRD patterns of lithium (poly)sulfides prepared by reduction of sulfur using $LiEt_3BH$ in THF. In each pattern, TiO_2 anatase was added as an external standard to quantify the amorphous content. The "Li_2S_2" sample (red pattern) contains significant nanoscrystalline Li_2S. Li_2S_6 (blue) is purely X-ray amorphous while "Li_2S_8" (green) exhibits weak diffraction peaks of α-S_8.

	Diffracting Li_2S	Diffracting $\alpha\text{-}S_8$
Li_2S	57 wt%	none
Li_2S_2	39 wt%	none
Li_2S_6	< noise	≤ noise
Li_2S_8	< noise	8 wt%

Table 2. Li_2S and $\alpha\text{-}S_8$ quantification from XRD diagrams of Li_2S_n samples

3.2.2.3. Characterization by MAS (Magic Angle Spinning) NMR

3.2.2.3.1. ^7Li NMR on synthesized lithium-polysulfides.

^7Li MAS NMR experiments were first run in McMaster University in collaboration with Dr Gillian Goward. **Figure 19**.**a.** shows the isotropic band observed for Li_2S, "Li_2S_2", Li_2S_6, and "Li_2S_8" at a MAS frequency of 30 kHz. From **Figure 19**, it appears that at least two different Li NMR shift can be distinguished. It shows single but distinct Li environments in the case of Li_2S and Li_2S_6 confirming that the amorphous content of Li_2S is similar to the crystalline phase and that of Li_2S_6 corresponds to an intermediate lithiated phase. The two distinct peaks are separated by approximately 1.3 ppm. **Figure 19.b.** shows the use of Li_2S and Li_2S_6 components to fit "Li_2S_2". It appears the other targeted compositions "Li_2S_8" and "Li_2S_2" are a mixture of these two phases, and possibly elemental sulfur, invisible to ^7Li NMR.
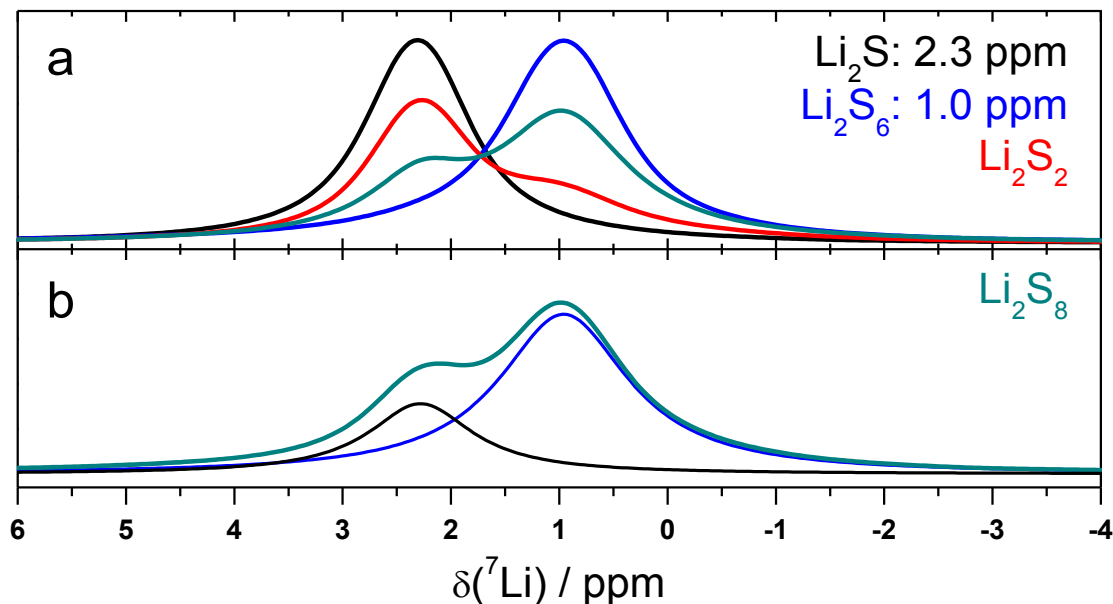
Figure 19. ^{7}Li MAS NMR showing single but distinct Li environments in the case of Li_2S and Li_2S_6.

3.2.3. Conclusion on lithium polysulfides synthesis.

As a conclusion to this section, we are quite confident that a novel stable intermediate Li_2S_6 between Li_2S and elemental sulfur was successfully isolated. While XRD could not reveal its structure, ^{7}Li NMR confirmed a novel lithium environment and a single phase. This stabilization is the first in the literature and it allows using it as reference for long-chain polysulfides. However, all the others Li_2S_n compositions targeted correspond to mixture of Li_2S, Li_2S_6 and elemental sulfur, which is why sodium polysulfides are needed to complete the picture.Synthesis of sodium polysulfides.

3.2.4. Synthesis of Na₂S₂ and Na₂S₄.

Sodium polysulfides Na_2S_2 and Na_2S_4 were prepared by the reaction of sodium sulfide nonahydrate with elemental sulfur in absolute ethanol.[26] In brief, the sodium sulfide nonahydrate was dissolved in absolute ethanol into a three-necked flask fitted with a reflux condenser and

rubber septa. The system was first flushed with argon and then maintained under argon flow. Sulfur powder (stoichiometric) was added quickly and the resulting mixture was refluxed under nitrogen for 1 h. The temperature was decreased and kept at room temperature overnight. The reflux condenser was removed and the flask connected to a water pump by a two-way glass stopper. The solvent was evaporated at room temperature after what the orange powder was further dried at 80 °C for 2 hours.

3.2.5. Characterization by XRD.

Figure 20 shows the XRD patterns of these compounds. Na_2S_2 is on the top, Na_2S_4 on the bottom. The diagram of Na_2S_4 exhibits no extra diffraction peak, validating its use as a reference. Unfortunately, Na_2S_2 exhibits a $Na_2S.5H_2O$ secondary phase which makes it a questionable reference for any analysis, although it can still be used for fingerprinting on the purpose of XANES measurements.
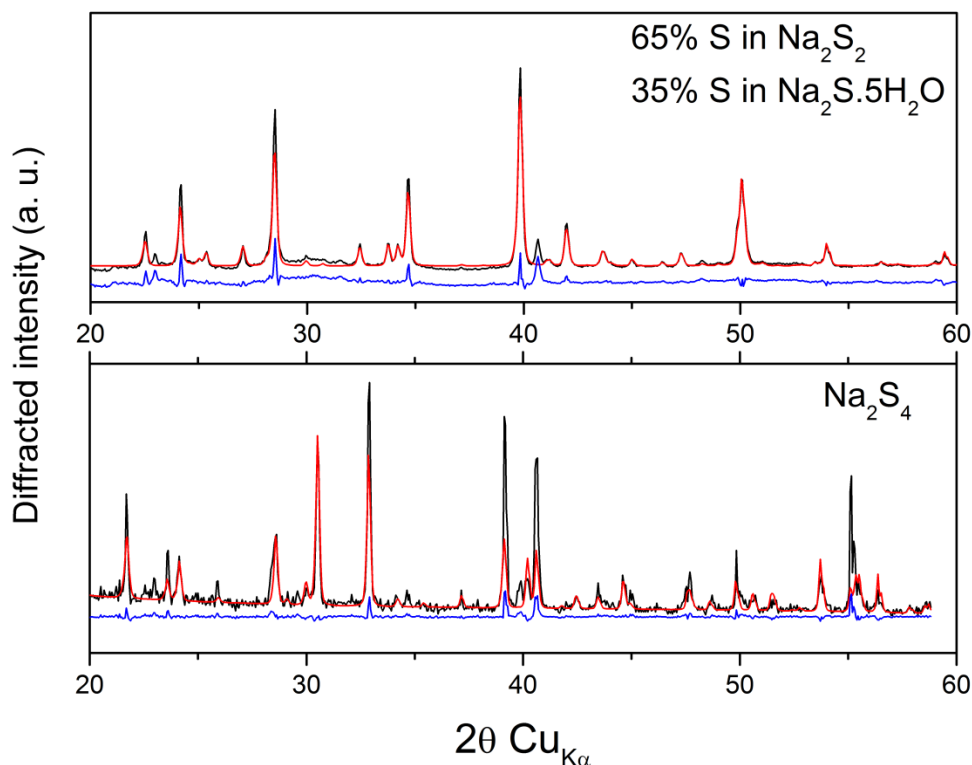
Figure 20. XRD patterns of sodium (poly)sulfides prepared by reacting sulfur and sodium sulfide in ethanol. The Na_2S_4 sample exhibits the diffraction peaks of the pure phase, while the Na_2S_2 sample contains a $Na_2S \cdot 5H_2O$ impurity, accounting for 35 % of the total sulfur.

3.3. X-ray Raman Spectroscopy (XRS) and X-ray absorption Near-edge structure (XANES).

The core of this thesis lies in the X-ray absorption spectroscopy study of the Li-S system under operating conditions. Preliminarily, opportunity was given to run non-resonant inelastic X-ray scattering (XRS) measurements on the as synthesized lithium polysulfides. The goal was also to test the feasibility of *in situ* XRS studies. In the present section are presented as well the X-ray absorption near-edge spectroscopy (XANES) spectra measured on the reference powder samples, setting the groundwork of the *operando* studies detailed in the next chapter. All the synchtrotron

data were collected at the Argonne Photon Source (APS) in the Argonne National Laboratory, in collaboration with Dr. Balasubramanian and Dr. Bolin.

3.3.1. Sulfur K-edge XANES measurements.

XANES spectra at sulfur K-edge of as-synthesized lithium (poly)sulfides – Li_2S and Li_2S_6 –, sodium polysulfides – Na_2S_2 and Na_2S_4 –as well as elemental sulfur are presented in **Figure 21**. The spectra were recorded in fluorescence mode. To reduce distortion due to self-absorption, low sulfur concentration (around 10 wt% of sulfur) was used by dilution in carbon. The small particle size of the as prepared Li_2S, and certainly lithium polysulfides, was there very convenient. By contrast, micron large Na_2S_n powder samples were ball-milled at 500 rpm for 5 hours together with carbon under Argon atmosphere.
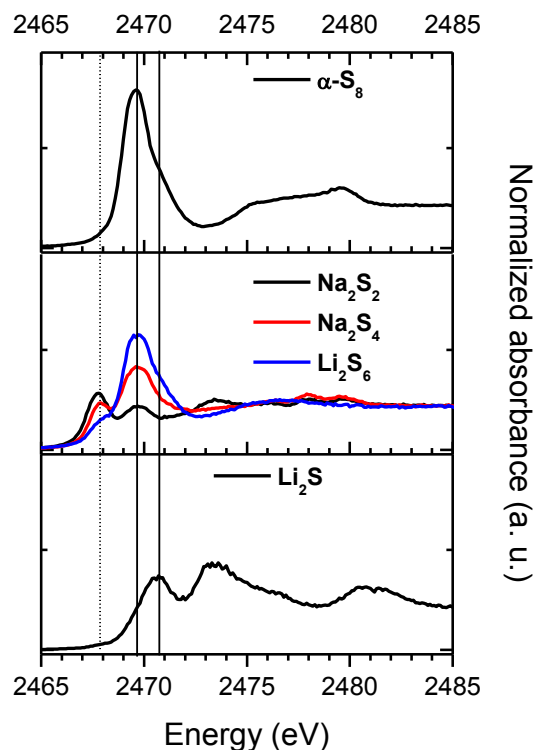
Figure 21. XANES spectra for elemental sulfur (**top**), linear polysulfides (Na_2S_2, Na_2S_4, and Li_2S_6, (**middle**) and lithium sulfide (**bottom**). Linear polysulfides exhibit a low energy feature which intensity is function of the chain length.

Elemental sulfur (top) exhibits a high intensity white-line around 2469.5 eV arising from the transition from the 1s to 3p levels, along with a higher energy feature at 2476.8 eV.[35] The three polysulfides used – Li_2S_6, Na_2S_4, and Na_2S_2 – all exhibit a low-energy feature around 2468 eV as well as a contribution at the white-line energy. Noticeably, the low energy feature varies with the polysulfide chain length, decreasing in intensity from Na_2S_2 to Li_2S_6, which is opposite to the increase in intensity of the white-line. The presence of this feature in the spectrum of Li_2S_6 comforts the hypothesis drawn from ^{7}Li NMR that a novel solid phase was successfully isolated. The last reference spectrum shown at the bottom corresponds to lithium sulfide and is mainly composed of two features at 2471 eV and 2474 eV, it is very similar to other Li_2S spectra that can be found in the literature, and to that of the commercial material we measured (not shown here).[35, 66]

As mentioned in the introduction chapter, the assignment of the low-energy feature to linear chain polysulfides was proposed by Abruña *et al*.[35] In contrast, this is a clear experimental evidence since the spectra of Na_2S_2, Na_2S_4 – both identified by XRD –, and Li_2S_6 are very similar. The difference lies in the intensities ratio between the white line and the low-energy feature. The spectra of elemental sulfur and lithium sulfide are clearly different, and the low energy feature is only present in linear chain polysulfides. Overall, the XANES signatures of the various redox species are different at the sulfur K-edge, which should allow carrying *operando* XANES studies of the Li-S system. However, the spectra of different polysulfides exhibit the same characteristic features, which could make it difficult distinguishing between them.

3.3.2. X-ray raman at the sulfur L-edge and at the lithium K-edge.

By using the non-resonant inelastic X-ray scattering (NRIXS or XRS) setup of sector 20 at the APS, both the sulfur $L_{2,3}$-edge and the lithium K-edge are accessible. Measurements were carried out on (poly)sulfides and elemental sulfur.

3.3.2.1. Solid lithium polysulfides spectra.

XRS experiments were first performed on thick pellets of: Li_2S, Li_2S_2, Li_2S_6, Li_2S_8 and S_8. Spectra recorded on the S-$L_{2,3}$ and Li-K edges are displayed in **Figure 22** and **Figure 23**, respectively.
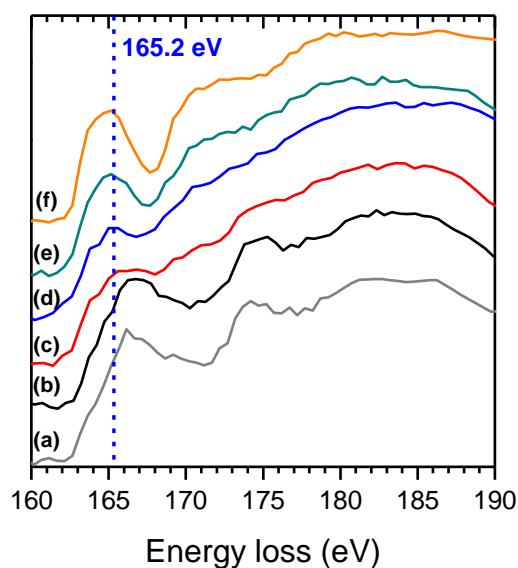
Figure 22. Processed XRS S-$L_{2,3}$ spectra of reference Li_2S_n: (a) commercial Li_2S, (b) as-prepared Li_2S, (c) "Li_2S_2", (d) Li_2S_6, (e) "Li_2S_8", and (f) commercial S_8. The dotted line shows is placed at the edge of elemental sulfur for comparison.

From the S-L$_{2,3}$ edge profiles (**Figure 22**), several observations can be made:

➢ The large Compton background observed for these samples however make the edge less well-defined compared to XANES (see **Figure 21**). The Compton scattering is higher because XRS exhibit small scattering amplitude (smaller cross-section).

➢ The local structure of Li$_2$S synthesized by reduction of sulfur using super hydride is identical to the commercial sample. The peak broadening observed by XRD does not hide any XRD-amorphous impurity phase, in excellent agreement with ^{7}Li NMR.

➢ Rather than exhibiting intermediate peaks, the spectra of Li$_2$S$_n$ samples "Li$_2$S$_2$", Li$_2$S$_6$, and "Li$_2$S$_8$" look like linear combinations of S$_8$ and Li$_2$S end members. Previous XRD and ^{7}Li MAS NMR measurements show that it is the case for "Li$_2$S$_2$" and "Li$_2$S$_8$". Li$_2$S$_6$ on the contrary shows no such Li environment as in Li$_2$S. If the biphasic nature of Li$_2$S$_6$ could previously be ruled out, it does not necessary imply that the electron configuration should be identical for all sulfur atoms in the polysulfide chain.
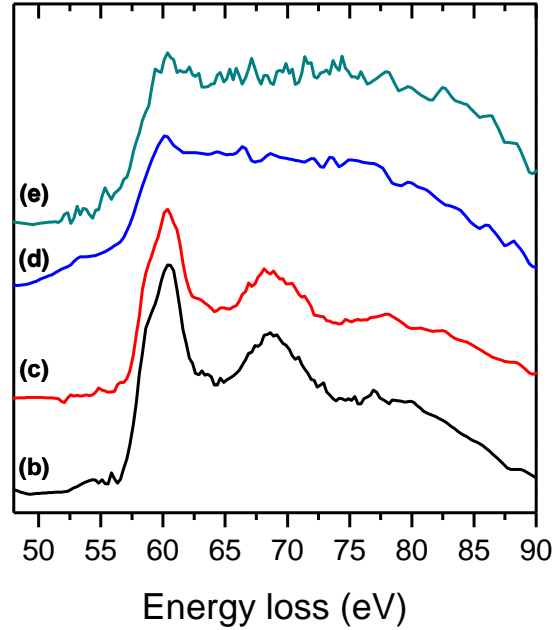
Figure 23. Processed XRS Li-K spectra of reference Li_2S_n: (b) as-prepared Li_2S, (c) Li_2S_2, (d) Li_2S_6, and (e) Li_2S_8.

Regarding the lithium K edge (**Figure 23**), it is also clear that the "Li_2S_2" sample mostly comprises of Li_2S as already suggested by ^7Li NMR. The spectra measured on Li_2S_6 and "Li_2S_8" are both less straightforward, again due to Compton scattering caused by the higher sulfur content in the samples. For low-Z elements such as lithium, Compton scattering contribution is problematic, and concentrated lithium systems are required. Unfortunately, this criterion is apparently not met in the case of long chain polysulfides.

3.3.2.2. Feasibility of *operando* XRS : *Ex-situ* measurements on cycled sulfur cathodes.

The feasibility of *operando* XRS measurements was tested by preliminary *ex situ* measurements. After different cycling duration (see **Figure 24.a**) electrodes were recovered and sealed in small Kapton pouches. Positive electrodes prepared for these experiments were based

55

on active material containing 82 wt% of sulfur to ensure high sulfur concentration. The addition of inactive electrode components was drastically limited (8 wt% of Multiple walled carbon nanotubes (MWCNT) and 7 wt% PEO binder) in order to avoid Compton scattering (background) while sulfur loading was increased up to 3 mg.cm^{-2} to maximize the effective intensity. Despite such requirements (unfavorable to electrochemistry), attention was paid to obtain satisfactory galvanostatic response, as illustrated by **Figure 24.a**.
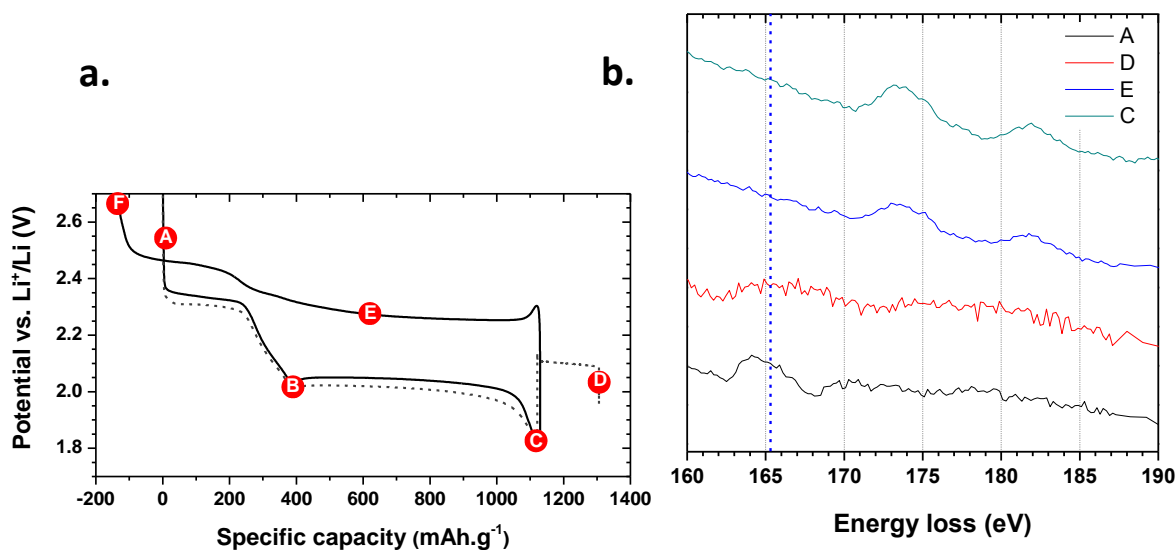
Figure 24. a. Electrochemical profile preliminary to the *ex-situ* XRS measurements, the letters design the points where the cells were stopped. **b.** Processed XRS S-L$_{2,3}$ spectra measured on the cathode;

The analysis of these samples by XRS proved extremely difficult, due to rapid beam damage. Such sensitivity was assigned to the exothermic degradation of PEO binder, used as an alternative to PVDF to avoid the contribution of fluorine to the background. Thus, only few samples could be analyzed and **Figure 24.b** displays the S-L$_{2,3}$ edges measured in **A**, **D**, **E** and **C**. Notice that the signal is significantly less intense compared to thick pellets, the spectra measured in **A** and **D** could correspond to elemental sulfur and lithium sulfide, with a first XRS peak at 164 eV and 166 eV, respectively. Unfortunately, the XRS peaks observed for **E** and **C** are

significantly shifted toward higher oxidation states (possibly S^{4+} or S^{6+} at 9 eV from elemental sulfur), which could be attributed to contamination of the samples during their preparation or analysis.

3.3.3. Conclusion.

A clear distinction can be made between linear chain polysulfides, lithium sulfide, and elemental sulfur using XANES at the sulfur K-edge. Among linear chain polysulfides, short-chain and long-chain polysulfides can be distinguished based on the intensity of the low-energy feature. These species are expected to be involved in the redox mechanism between lithium and sulfur. Therefore, it is confirmed that XANES is a method of choice to perform an *operando* analysis of a Li-S battery. However, self-absorption issues, which result in a huge distortion on the sulfur K-edge, have to be dealt with care.

The overall conclusion to XRS experiments is that, on the S-$L_{2,3}$ edge, the energy range separating the different sulfur species in presence in a Li-S cell is extremely narrow. As a result, the resolution in energy does not seem sufficient to distinguish polysulfides and the application of XRS to *operando* studies of sulfur reduction appears compromised. Indeed, e*x situ* measurements were also performed, but even at high sulfur ratio (82 wt%) the Compton scattering compromised the analysis of the signal.

3.4. Overall conclusion and perspectives of this chapter.

An attempt to synthesize solid Li_2S_n ($n \geq 1$) from the chemical reduction of α-S_8 by $LiEt_3BH$ is presented in this chapter. The use of XRD, ^{7}Li NMR, XANES, and XRS to characterize lithium and sodium polysulfides provides a clear spectroscopic signature – or fingerprint – of these different species.

The synthesis leads to the first report of stable linear chain intermediate, Li_2S_6, between element sulfur and Li_2S. XRD cannot characterize this new phase due to its amorphous nature, and is therefore irrelevant to study the lithium polysulfides species. In contrast, the use of local probes proposed in this work results in a better characterization of (poly)sulfides. ^{7}Li NMR shows a clear difference between as synthesized Li_2S_6 and Li_2S of 1 ppm, and therefore proves that Li_2S_6 is stabilized as novel solid lithium polysulfide. To complete the picture, sodium polysulfides Na_2S_2 Na_2S_4 and Na_2S_5 are good alternative in the perspective of spectroscopic studies.

Preliminary *ex situ* XANES results show that this spectroscopy is a really promising technique to follow sulfur speciation since elemental sulfur and Li_2S exhibit a clearly different signature at the S K-edge. All linear chain polysulfides are characterized by a low-energy feature, and their spectra differ only by the ratio of the intensities of the low-energy feature and the white-line. This could be an important issue to characterize mixtures of (poly)sulfides for *in situ* measurements. By comparison, *ex situ* XRS proves a less straightforward technique for sulfur speciation. The experimental requirements are more problematic, while the differences between elemental sulfur, polysulfides and Li_2S are not that pronounced.

4. Sulfur redox mechanisms in lithium batteries by *operando* XANES.

4.1. XANES Sulfur K-edge to probe Li-S batteries.

4.1.1. Introduction.

Although sulfur K-edge XANES is an excellent probe of S-S bond scission and re-formation,[67] only one study so far had investigated the electrochemistry of the Li-S system by this method.[35] The setup used was optimized to elucidate the reactivity of electrolytes and this report showed that the solvent was playing a key role in the electrochemical performance of the cell. It confirmed the reactivity of alkyl carbonate-based electrolyte with intermediate sulfur radicals such as $S_3^{\bullet-}$. They compared the effect of electrolytes based on TEGDME, DOL:DME and carbonate solvents. Interestingly, a spectral feature at low energy, characteristic of polysulfides, was observed in TEGDME and DOL:DME, even if no reference spectrum could clearly confirm it at this point.

This earlier study is a strong encouragement to perform *operando* XANES measurements on a Li-S battery. Reference compounds prepared during this thesis (see previous chapter) would certainly help clarifying this. In particular, the successful synthesis of Li_2S_6 could provide a clear signature of one linear chain polysulfide at the sulfur K-edge. From there, the idea was to follow the evolution of sulfur species upon cycling in a typical Li-S cell; it is much more ambitious than this seminal study, and as a result requires more precautions. The study has been extended to untypical Li-S system. The *in situ* X-ray absorption experiments involved 4 days of data collection at the Argonne Photon Source in Argonne National Laboratory with Dr. Marine

Cuisinier and Mason Kolbelck (undergrad student), followed by weeks of data treatment. This chapter discusses the "digested" results, and the knowledge gained.

4.1.2. Design of the carbon host and preparation of reference materials.

4.1.2.1. Design of the carbon host: self-absorption issue.

4.1.2.1.1. Fluorescence mode involves distortion of the spectra.

The statement that $\mu(E)$ measured in fluorescence is proportional to the absorption – and therefore that recording the fluorescence emission is similar to recording the absorption – is only true in the limit of very thin samples or very dilute samples. For thick, concentrated samples, the depth into which the incident beam can penetrate changes as fine structure of $\mu(E)$ changes. As the oscillatory part goes up, the penetration depth diminishes, decreasing the actual intensity recorded. As it goes down, the depth increases, increasing the actual intensity recorded. This effect causes non-linear distortion that leads to a flatten spectrum. It is called self-absorption or overabsorption. At the sulfur K-edge particularly, this is known to be a major issue of the fluorescence acquisition mode.[60,68]

The impact of self-absorption is mainly linked to the depth probed by the X-ray beam. In this context, the size of sulfur domains with respect to this penetration depth (around 1-2 μm after the edge[59]) is important as shown on **Figure 25**. It is clear that, as the sulfur domain size increases from 200 nm to 10 μm, the distortion becomes a serious issue. It can results in the incapacity to distinguish the different features that make a spectrum recorded from a mixture.
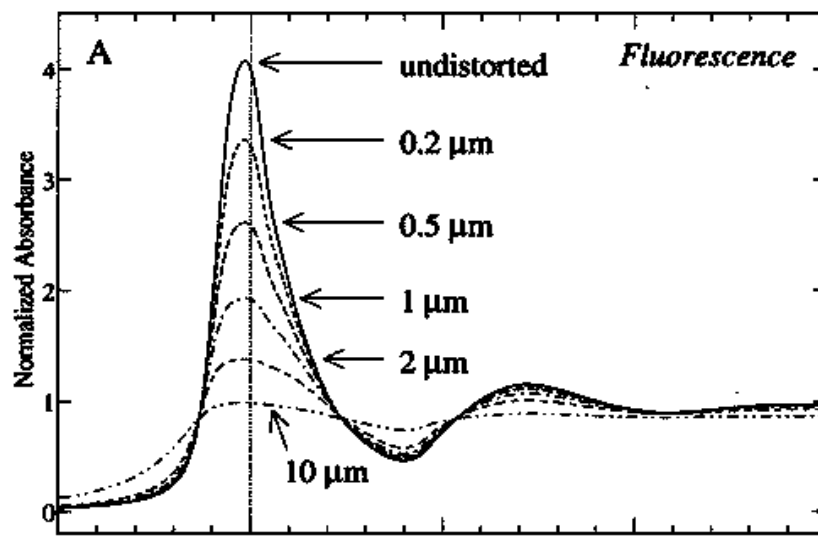
Figure 25. Self-absorption, or overabsorption, effect on the sulfur K-edge compared for different size of sulfur domains from 0.2 μm to 10 μm reproduced from ref. 68.

4.1.2.1.2. Porous Carbon Nanospheres as a solution to avoid self-absorption.

To avoid overwhelming self-absorption, a nanoscale characteristic length in all the three dimensions was needed. The experience of our lab in designing carbon hosts for Li-S battery was an opportunity to obtain such a tailored material. In this purpose, Scott Evers prepared porous carbon nanospheres (PCNS) that are shown in **Figure 26**. The SEM image shows spheres that are all approximately close to 220 nm in diameter, with a homogeneous ≈ 20 nm shell thickness. After sulfur infiltration (PCNS/S), the energy dispersive X-ray (EDX) line-scan (inset in **Figure 26**) also shows a homogeneous sulfur signal throughout the shell of the sphere where the sulfur is primarily confined, and no sulfur contribution from the exterior. The sulfur domains are not more than 220 nm, and certainly less than that if considering that sulfur is mostly within the shell.
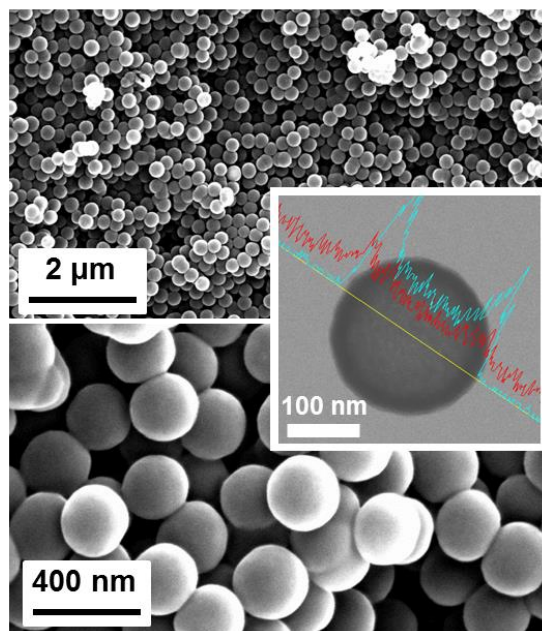
Figure 26. SEM images of PCNS's at both low and high magnification. Inset: STEM image with EDX line-scan (red line – carbon, blue line – sulfur) shows a homogeneous sulfur distribution throughout the shell of PCNS/S- 58 wt%.

The purpose of reducing the distortion caused by self-absorption is to be able to approximate its effect and then correct it. Realistically, the distortion could never be 0. If the distortion is too important, it is however impossible to correct a spectrum strictly. In order to double-check the correction, a a pristine cathode was measured in total electron yield (TEY), which is not subject to self-absorption phenomenon. **Figure 27** shows the spectrum collected by TEY (red) compared to the one collected by fluorescence (black). As a matter of comparison, a cathode based on sulfur imbedded in CMK-3, which is made of nanorods of carbon is also shown (blue). There is a clear diminution of the white line of sulfur between these three, which corresponds to the distortion caused in fluorescence mode. The distortion is not severe for PCNS/S, compared to what can be seen for CMK-3/S, with respectively 17 % and 37 % attenuation on the white line. This small distortion in the case of PCNS/S can be reasonably

corrected with ATHENA software (crosses on **Figure 27**). The correction on CMK-3/S is also

feasible but would be controversial since the distortion is too important.
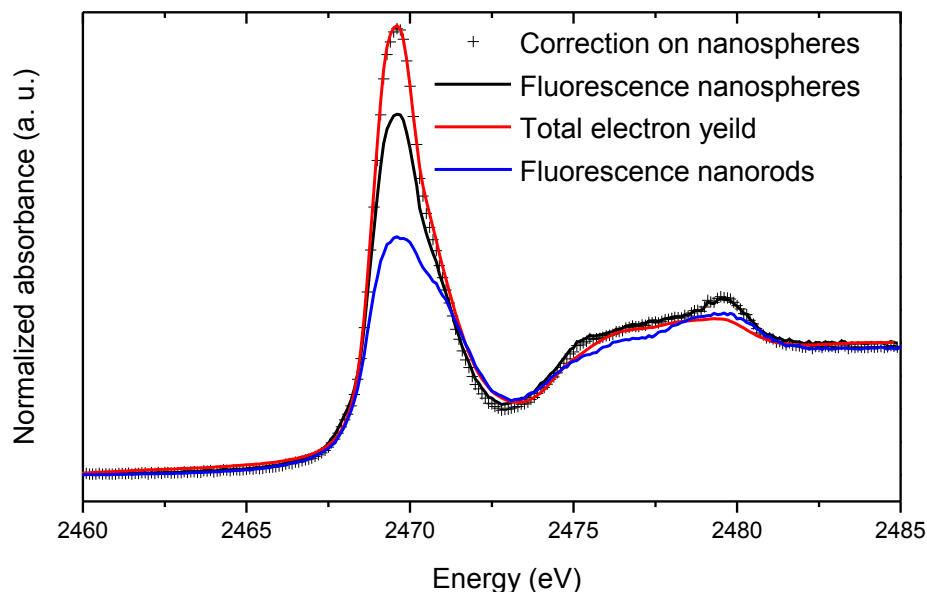
Figure 27. Sulfur. K-edge spectra of a pristine sulfur cathode made with PCNS (black) and CMK-3 (blue) measured in fluorescence yield compared to a pristine cathode measured in total electron yield (TEY, red). The small distortion achieved in the PCNS/S allows correcting the spectra (black crosses).

4.1.2.2.   Reference materials used for data analysis.

Since XANES is mostly a finger print method, reference spectra of appropriate

compounds were needed to understand the evolution of the XANES measurements upon cycling.

It was particularly important to collect the reference spectra in the exact same conditions as the *in*

situ measurements (size of the sulfur domains, dilution in the carbon host, beam line setup and

energy calibration) to avoid misleading spectral distortion or energy shift. The reference materials

– α-S_8, Li_2S, Na_2S_2, Na_2S_4, and Li_2S_6 – were presented in the previous chapter. **Figure 21** showed

their XANES signature at the sulfur K-edge.

4.2. Operando XANES study of PCNS/S composite filled with 56 wt% sulfur.

Operando XANES measurements were performed on the PCNS filled with 56 wt% of sulfur. The overall percentage of sulfur was decreased to 10 wt% by the addition of Super P and PVDF as a binder, to circumvent self-absorption. DOL:DME (1:1) was used as the electrolyte with 1 M $LiClO_4$ as a salt in order to circumvent any contribution from the electrolyte at the sulfur K-edge compared to commonly used LiTFSI. 2 wt% $LiNO_3$ was added to prevent any shuttle mechanism.

Reproduced in part with permission from DOI: 10.1021/jz401763d Copyright 2013 American Chemical Society.

4.2.1. Results obtained.

4.2.1.1. Electrochemistry of the first cycle, good behavior of *in situ* cell.

One crucial point was to make sure that the *in situ* cell behaved similarly to a normal coin cell. **Figure 28** compares the voltage profile of the *in situ* cell (red) and a normal 2325 coin cell with the PCNS filled with 56 wt% sulfur used as the cathode. There are very similar, with an overall capacity around 1100 mAh.g^{-1} which is in good agreement with what can be found in the literature (see **Figure 3**). The voltage profile consists approximately of two plateaus during discharge and a long slopping curve during charge.
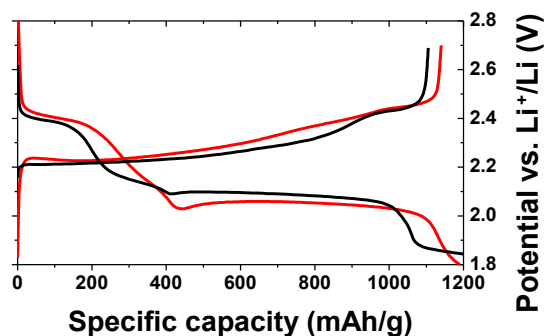
Figure 28. Voltage profile of the standard 2325 coin cell (red) and of the cell designed for the operando XANES measurements (black).

4.2.1.2. Spectra collected, small distortion achieved.

Figure 29.a shows the *operando* XANES results on a PCNS/S cathode during the first galvanostatic discharge at a C/5 rate and for the second full cycle at C/10, as a function of specific capacity. Discharge capacities of approx. 1200 mAh.g^{-1} and 1100 mAh.g^{-1} were achieved during the first and second cycle, respectively, at these slower rates that were utilized to minimize the compositional change between two spectra.

Figure 29.b displays the pristine, charged and discharged states recorded in the course of cycling along with the reference spectra. The comparison with α-S$_8$ (top) proves that the pristine state and the charged states of the *operando* cell correspond to elemental sulfur. It is a first strong result that contradicts some previous *in situ* studies based on long range techniques like XRD,[31,32,33] thus proving the usefulness of XANES for sulfur speciation. At the end of discharge, the intensity is minimal at the white-line energy, in agreement with the Li$_2$S reference showing two peaks at 2470.8 eV and 2473.7 eV. The spectra illustrative of the discharged state (bottom) do not exhibit any low energy intensity characteristic of linear polysulfides, although comparison with pure Li$_2$S shows that some α-S$_8$ remains in the cathode composite. This is consistent with the electrochemistry which shows 75% capacity compared to theoretical (1675 mAh.g^{-1}) on discharge. The reason for this is explained later in this report.
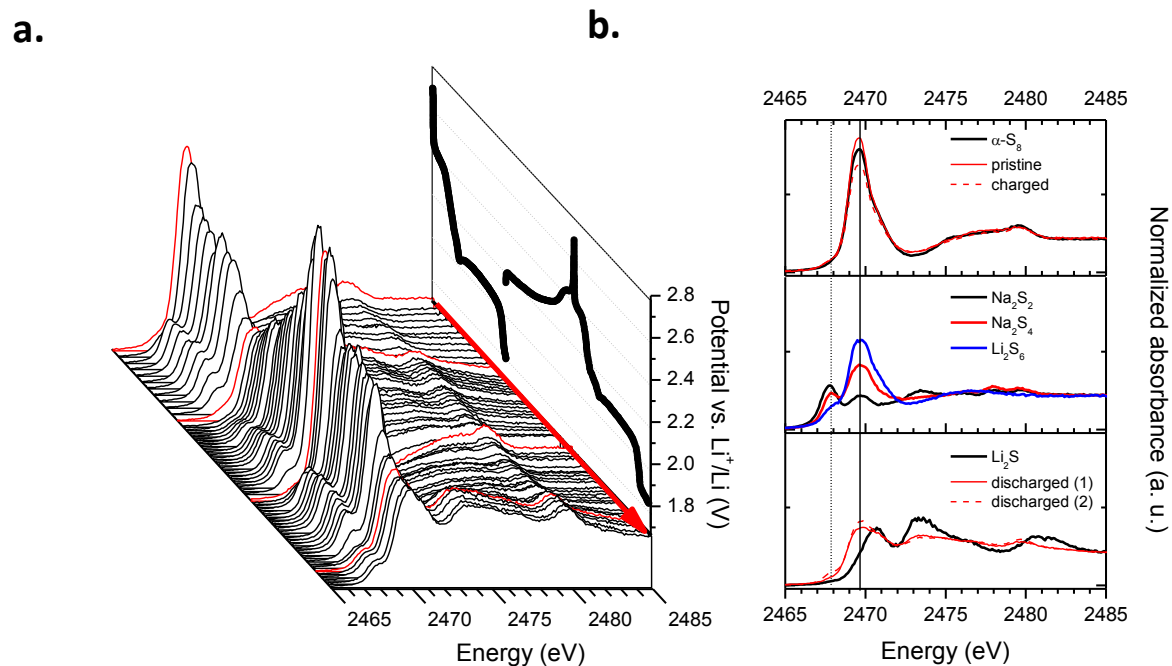
Figure 29. Sulfur K-edge XANES upon cycling and reference spectra. **a.** Evolution of absorbance as a function of the electrochemical cycling, at C/5 (first discharge) and then C/10. End of (dis)charges are highlighted in red. **b.** Reference spectra for elemental sulfur (top), linear polysulfides (Na_2S_2, Na_2S_4, and Li_2S_6, middle) and lithium sulfide (bottom).

Some representative spectra are displayed on **Figure 30**. **Figure 30.a** shows four spectra recorded during charge at different average compositions Li_xS. x=1.3 (i.e. 1090 mAh.g^{-1}) corresponds to the discharged state of the cathode while x=0 corresponds to the pristine or recharged state. **Figure 30.b** shows some spectra representative along the discharge. The formation of polysulfides for instance is clearly indicated by the appearance of the low-energy feature. During charge, from x=1.3 to x=0.25, it is particularly visible that this low-energy feature around 2467 eV and the white line of sulfur around 2469.5 eV increases, signaling the formation of linear chain polysulfides. Simultaneously, the feature around 2474 eV that is related to Li_2S decreases. At the end of charge, between x=0.25 and x=0 the low energy feature decreases until complete disappearance, signaling the consumption of polysulfides. During discharge, similar

observations can be made, showing the formation and the consumption of Li_2S_n, elemental sulfur and Li_2S as will be detailed after.
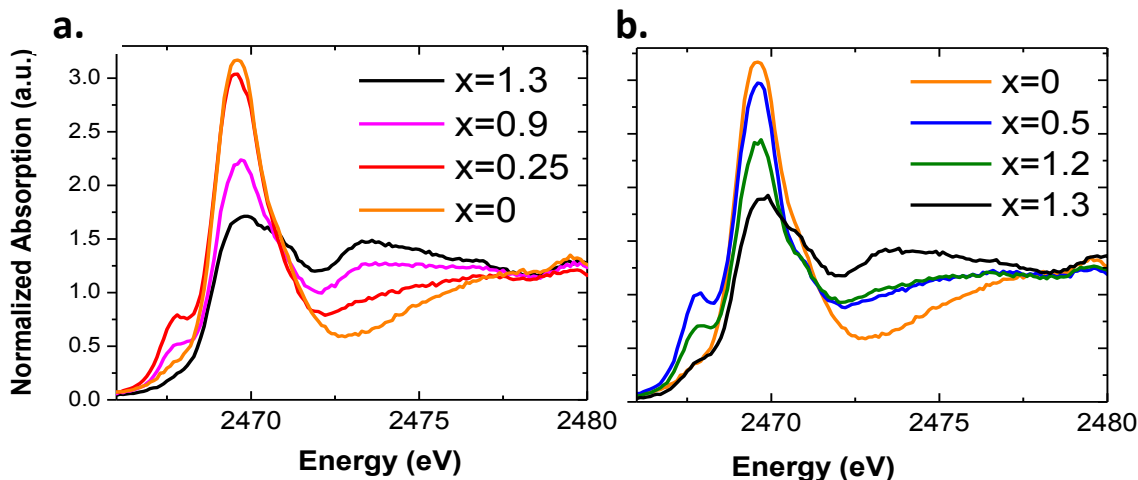
Figure 30. Selected spectra recorded during **a.** charge and **b.** discharge. x corresponds to x in Li_xS.

4.2.2. Data analysis.

The exceptional quality of the spectra allows performing a detailed data analysis. The first method envisaged was an analytical fit using Gaussians, but it cannot follow sulfur speciation in details alone as we will see. Linear combination analysis allows a more detailed analysis and was performed based on the reference spectra, which represent the sulfur species successively formed by the electrochemistry. This method is more subject to interpretation but obviously, it should lean against what we already know about the Li-S electrochemical system.

4.2.2.1.   Gaussian fit analysis.

4.2.2.1.1.   Principle of Gaussian fit analysis.

Reference spectra were fitted using a combination of Gaussian and Arctangent functions. The idea is to assign to each compound one or more Gaussians, and then to follow the evolution of their intensity upon cycling.[67]

Figure 31 shows the Gaussian functions present in each reference compounds, from elemental sulfur (top) to Li_2S (bottom). The position in energy and the assignment of each Gaussian is summarized in **Table 3**. Unfortunately, each of them can be found in several compounds, which makes it difficult to use a particular Gaussian to follow the formation/consumption of one particular species. However, some Gaussians appear to be more strongly correlated to one compound. For instance, {G2; G5} are indicative of elemental sulfur, {G3; G4} of Li_2S, and G1 is characteristic of lithium polysulfides.
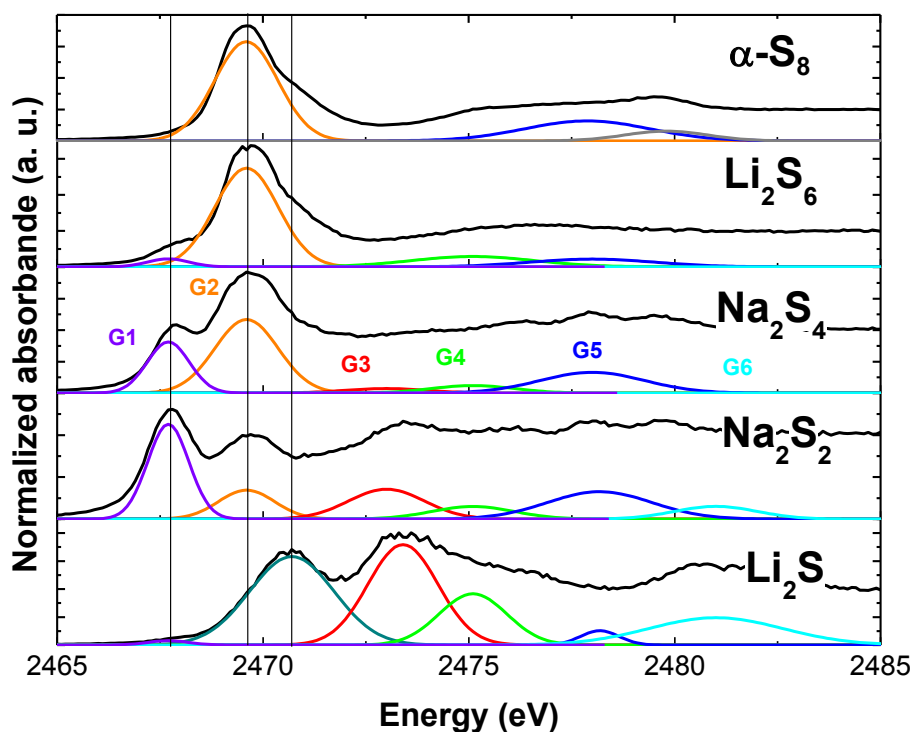
Figure 31. Gaussian contributions present in α-S$_8$, Li$_2$S$_6$, Na$_2$S$_4$, Na$_2$S$_2$, and Li$_2$S. 6 Gaussians named G1 (purple), G2 (orange), G3 (red), G4 (green), G5 (blue), and G6 (light blue) was used.

Name	Position (eV)	Relation with compounds
G1	2467.7	Characteristic of lithium polysulfides
G2	2469.5	White line of sulfur Indicative of elemental sulfur, but also present in polysulfides
G3	2470.8	Indicative of Li$_2$S, but also present in other compounds and element sulfur (in minority)
G4	2473.7	Indicative of Li$_2$S, but also present in polysulfides (in minority)
G5	2477.7	Indicative of elemental sulfur, but also present in polysulfides
G6	2483.1	Li$_2$S

Table 3. List of Gaussian peaks used to fit experiment S K-edge XANES spectra of the reference compounds.

Even if most of the Gaussian functions used are present in multiple compounds, a first look at their evolution upon cycling is interesting. The data analysis focuses on the full cycle performed at C/10, beginning with the charge of the cell. Results from this fitting method are shown in **Figure 32**.

The charge voltage profile, reminded on the bottom, consists of a slopping curve from around 2 V to 2.4 V, followed by a small plateau around 2.5 V. This electrochemical behavior is reflected by the variation of the peaks intensity of the Gaussian functions. Therefore, the charge can be divided into two regions. The first region corresponds to a clear increase of G1, G2 and G5 – corresponding certainly to the formation of polysulfides, and maybe elemental sulfur – at the expense of G3 and G4 that reflects the consumption of Li_2S . During the second step G1 drastically decreases, showing the consumption of linear chain polysulfides to form elemental sulfur (G2 and G5). In the same way, the Gaussian analysis looks consistent with the electrochemical signature of the discharge, which consists of two plateaus (around 2.35 V and 2.1 V). The first plateau corresponds to the sudden increase of G1, which reaches its maximum, at the expense of elemental sulfur (G2 and G5 decrease). The contribution of {G3; G4} also increases. Next, during the beginning of the second plateau, there is no change in the XANES (all the contributions are relatively constant during 300 $mAh.g^{-1}$). The last step corresponds to a clear decrease of G1 along with an increase of {G3; G4}, suggesting the consumption of polysulfides and the formation of Li_2S.
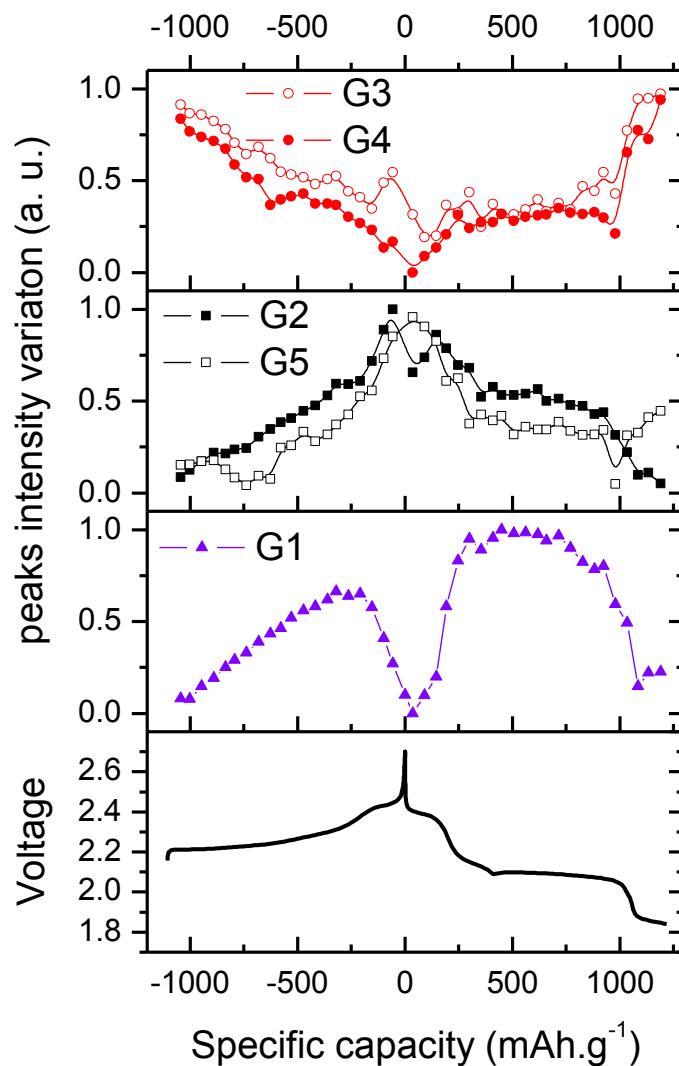
Figure 32. Evolution of the intensities of each Gaussian peaks upon cycling, starting on charge. {G3; G4} (top) are indicative of Li$_2$S, {G2; G5} (middle) are indicative of element sulfur, and G1 is characteristic of lithium polysulfides. The voltage profile is reported on the bottom.

To conclude, even if the Gaussian peaks analysis cannot follow quantitatively sulfur speciation upon cycling because no Gaussian function are characteristic of one particular compound, this first analysis shows that XANES evolution is clear upon cycling. For example, following G1 leads to follow the formation and consumptions of lithium polysulfides. The beginning of the low voltage plateaus correlates to no change in the XANES spectra; it is the only

part of the cycle where this spectroscopic study is unable to draw any conclusion as we will see in the next section.

4.2.2.2. Linear combination fit.

4.2.2.2.1. *Number of reference used for the fit.*

A linear combination analysis was performed using the reference spectra presented above. Because of the multiple solutions possible, this method requires a prior understanding of the electrochemical system. For example, the contribution of elemental sulfur is not expected to increase during discharge and such evolution was thus forbidden. **Figure 33** shows the fit results obtained with the different sets of references in terms of χ^2, which is used as the figure of merit. It is equal to $\sum(data - fit)^2$ reduced by the estimated noise of the data.[69] In **Figure 33.a**, χ^2 values of the 4-component LCF using $\{\alpha\text{-}S_8; Li_2S_6; Na_2S_4; Li_2S\}$ are plotted as a function of the scan number. In **Figure 33.b**, alternative LCF are compared, for which the χ^2 are normalized to the lowest (i.e. best) values given above for the 4 component fit. The 5-component fit (green) gives similarly good agreement with the experimental data. However, the additional Na_2S_2 component is found to be zero for a large majority of spectra. Among the 3-component fits, the one using only Na_2S_4 to account for the low energy feature gives the best results (red), but χ^2 values remain 20-50% higher than in the presence of Li_2S_6 in the 4-component fit. Moreover χ^2 of the 3-components fit noticeably increases when Li_2S_6 is expected to be present from the electrochemistry (scan number 20 to 30, which is the end of charge and the beginning of discharge), which is a strong indication that this component is necessary.
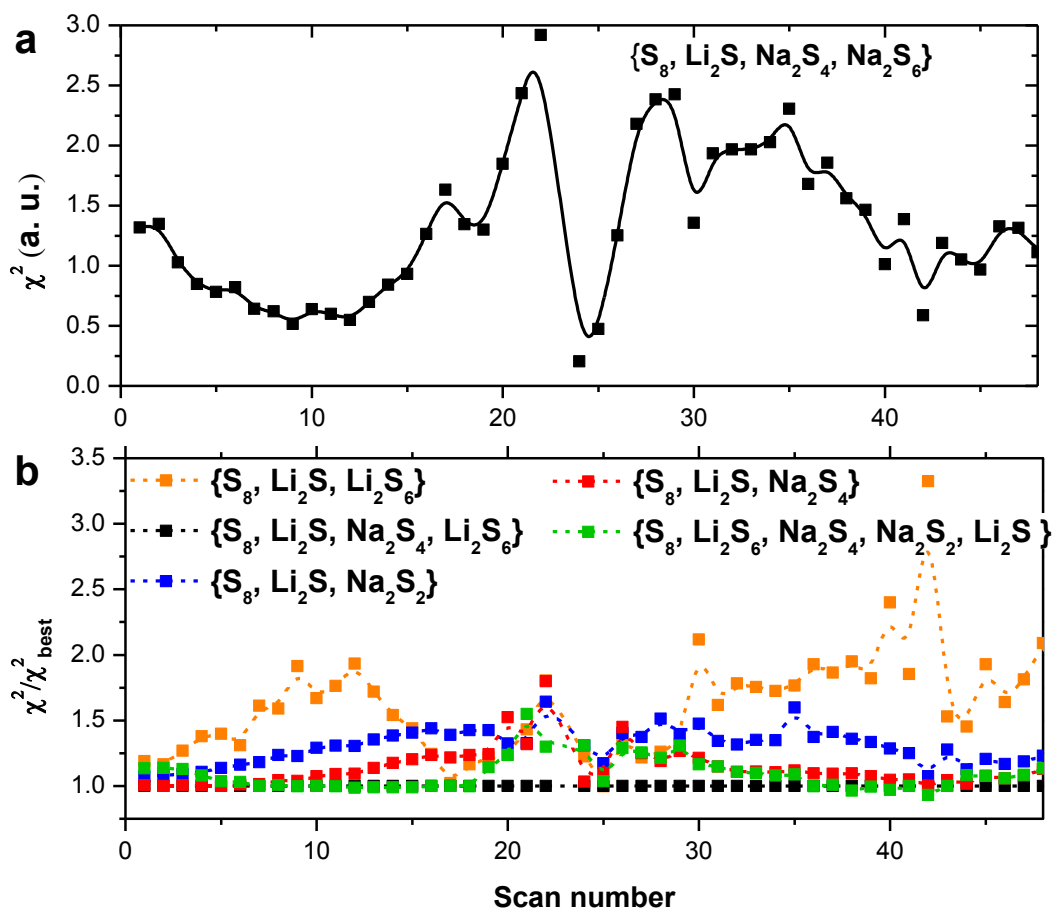
Figure 33. a. χ^2 obtained for the 4 component fit using {α-S_8; Li_2S_6; Na_2S_4; Li_2S}. **b.** Comparison of the χ^2 obtained with alternative LCF. The lowest value shown in a) is normalized to 1.

In conclusion, the fit using {α-S_8; Li_2S_6; Na_2S_4; Li_2S} is the best, justified on the basis of minimum number of components and minimum χ^2, not to mention the consistency with the electrochemistry as will be detailed below.

4.2.2.2.2.   *Results of linear combination analysis.*

The results of such linear combination fitting are plotted in **Figure 34**. The analysis starts with the charge at C/10 since we chose to discard the first discharge at C/5. Linear combination analysis allows following in real time the weight of each compound. This latter is directly linked to the actual fraction of sulfur since the reference spectra were recorded in the same conditions.

Unlike the Gaussian analysis presented in the previous section, the difference between Na_2S_4 and Li_2S_6, i.e. between different chain lengths of polysulfides, can be made (green and blue curves, **Figure 34**). The Li_2S contribution clearly decreases during charge reaching zero, and then increases at the end of discharge, as expected. The contribution of elemental sulfur is maximal in the charged state, and decreases upon discharge until the supersaturation point around 0.2 (molar fraction). After that, it stays constant so that $\alpha\text{-}S_8$ remains present at the very end of discharge.
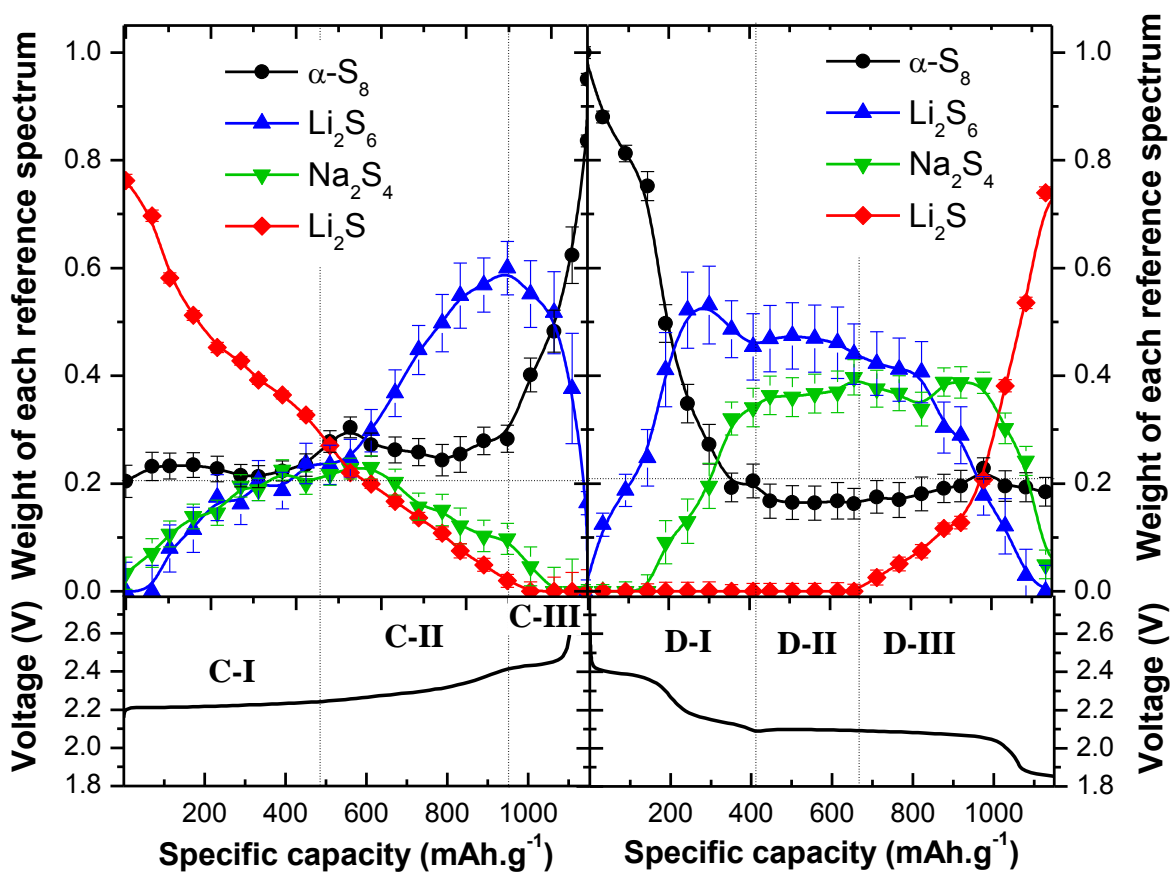
Figure 34. Linear combination fitting results using elemental sulfur (black), Na_2S_4 (green), Li_2S_6 (blue) and Li_2S (red) function of the specific capacity calculated from the electric current. The voltage profile is reminded on the bottom.

74

The validity of the linear combination analysis was also evaluated by its accordance with the electrochemistry. The result is presented in **Figure 35**. Lithium content (x in Li_xS) from XANES is calculated from the LCF and reported as a function of x calculated by integrating the current measured by electrochemistry. On **Figure 35.a**, an example of the fitting result using the 4 components is shown. The equivalent numbers of electrons for each compound used to calculate the capacity are indicated. For convenience on **Figure 35.b**, a dotted line $- x = y -$ represents the perfect agreement between the two capacities calculated.
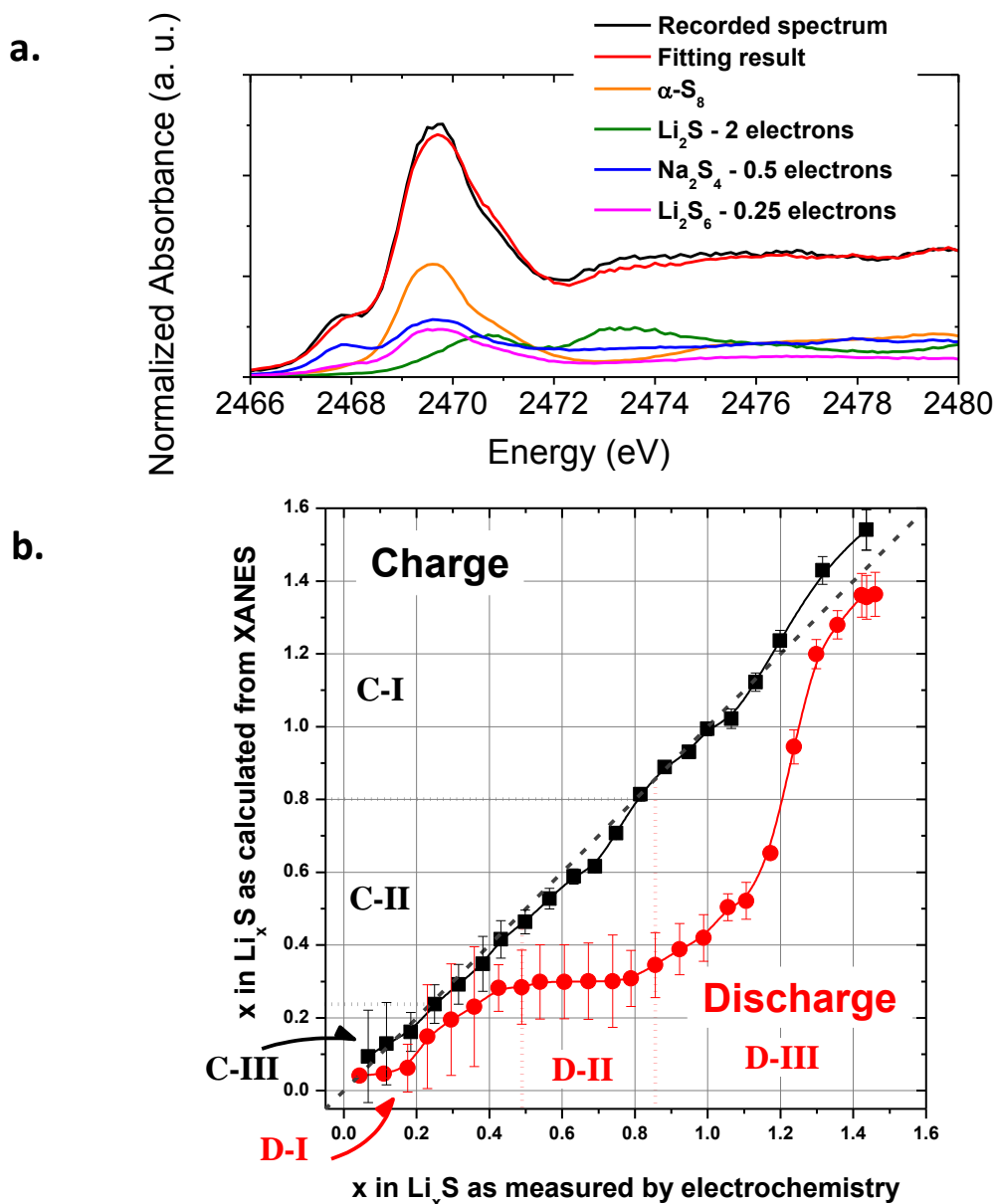
Figure 35. a. LCF result (red) of an experiment spectrum (black) obtained with α-S$_8$ (orange), Li$_2$S$_6$ (purple), Na$_2$S$_4$ (blue), and Li$_2$S (green). **b.** Composition of the cathode upon cycling based on the XANES and on the current. Lithium content from XANES is calculated from the LCF and reported as a function of x in Li$_x$S calculated by integrating the current measured by electrochemistry.

The perfect accordance observed upon charge doubly validates the experimental approach in the sense that the area probed is proved representative of the overall cathode behavior and sulfur speciation is effectively achieved. It also illustrates the excellent coulombic efficiency of

the cell (no redox shuttle). During discharge however, a clear discrepancy appears on the beginning second voltage plateau (D-II). It was shown during the Gaussian analysis that no change in the XANES spectra (i.e. no measureable structural change) occurs during 300 mAh.g^{-1}. At the end of discharge, the capacity calculated from XANES catches up the one measured by the current. This delay has no simple explanation; it could come from a weak spectral signature of Li$_2$S at the beginning of its formation. We can however rule out artifacts from cell design owing to the good agreement in charge.

4.2.2.3. Investigation of the charge mechanism.

The evolution probed by XANES and its consistency with the electrochemical profiles allow us to propose the following charge mechanism in three steps, as delineated by the dotted line **Figure 34 (left)**. The charge begins from the discharged state − after the first discharge at C/5 − that exhibits the clear presence of elemental sulfur as already highlighted in **Figure 29.b**, it corresponds to a molar fraction of 0.25 from the LCF.

Contrary to the common belief that S$_8$$^{2-}$ and elemental sulfur are the main oxidation products, [28] we observe that the slow and monotonic consumption of Li$_2$S during most of the charge process is instead accompanied by the formation of shorter chains. In fact, the formation of shorter chains, as observed here, is more likely because S$_8$$^{2-}$ is reported to rapidly dismutate[23] :

$$S_8^{2-} \rightarrow S_6^{2-} + 1/4\ S_8^{0}$$
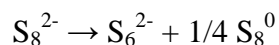
The contribution from S$_6$$^{2-}$ is detected even at the earliest stage, and increases along the sloping charge at the expense of S$_4$$^{2-}$, which appears as a transient species allowing the oxidation of Li$_2$S into more stable Li$_2$S$_6$ by the following reactions:

$$S^{2-} \rightarrow 1/4 \ S_4^{2-} + 3/2 \ e^- \ \text{and} \ S^{2-} \rightarrow 1/6 \ S_6^{2-} + 5/3 \ e^-$$
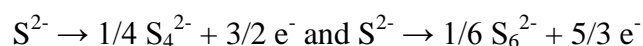
The late disappearance of Li$_2$S and S$_4^{2-}$ – hence the maximum of S$_6^{2-}$ – coincides with the voltage rise signaling the final oxidation step. This latter consists in the full conversion of S$_6^{2-}$ to α-S$_8$, as highlighted by the disappearance of the low energy peak and the steep increase of the white-line on the S K-edge spectra. While the consumption of Li$_2$S is still ongoing as described in the previous paragraph, the following reactions now occur:

$$S_4^{2-} \rightarrow 2/3 \ S_6^{2-} + 2/3 \ e^- \ \text{and} \ S_6^{2-} \rightarrow 3/4 \ S_8 + 2 \ e^-$$
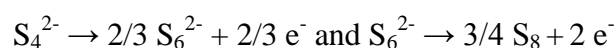
As discussed for **Figure 29.b,** the cathode composite recovers its pristine sulfurous state at the end of charge, indicating the excellent reversibility and retention of the active material within the PCNS host. In terms of the weight of the components, and considering the fraction of inaccessible sulfur, the overall charge can be summarized as**:**

$$\frac{3}{4} Li_2S \rightarrow \frac{3}{4} S^0 + \frac{3}{2} Li^+ + \frac{3}{2} e^-$$
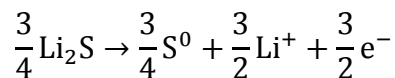
corresponding to a specific capacity of 1254 mAh.g^{-1}. Considering the accuracy of the measurement and the possible error on the LCF, this is in relatively good agreement with the 1085 mAh.g^{-1} measured experimentally. As highlighted in **Figure 29.b**, the cathode composite recovers its pristine sulfurous state at the end of charge, indicating the excellent retention of the active material within the porous carbon nanospheres.

4.2.2.4.   Investigation of the discharge mechanism.

The Li-S cell discharge was similarly investigated; the decomposition of the XANES spectra is shown in **Figure 34 (right)**. The partitioning as a function of the specific capacity is based

both on the electrochemistry and on the evolution of XANES. The following discharge mechanism can be proposed.

The first discharge plateau is usually described as the reduction of elemental sulfur to S_8^{2-}. As discussed above, it exist strong experimental evidence for the rapid chemical disproportionation of S_8^{2-}. Such chemical reactions would explain the formation of S_6^{2-} by the following reactions:

$$S_8 + 2e^- \rightarrow S_8^{2-} \text{ while } S_8^{2-} \rightarrow S_6^{2-} + 1/4\ S_8 \text{ which gives } 3/4\ S_8 + 2e^- \rightarrow S_6^{2-}$$
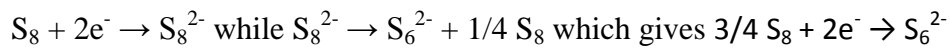
The linear combination fitting shows that the formation of S_4^{2-} already starts at the tail of the high voltage plateau. The second discharge step mostly corresponds to the reduction of S_6^{2-} to S_4^{2-}. These first two steps are not well resolved by XANES, but their separation is clear from the discharge curve, in agreement with the literature. The contribution of polysulfides increases at the expense of elemental sulfur, although no absorbance can be assigned to Li_2S at this point.

The third stage corresponds to the beginning of the low voltage plateau, where the successive reduction of polysulfides is believed to occur. Super-saturation marks not only the end of the α-S_8 consumption but also the maximum of polysulfides. While the cell voltage is then fixed at 2.1 V – implying the presence of Li_2S in the positive electrode – no significant change occurs in the XANES spectra during almost 300 mAh.g^{-1} recorded by the galvanostatic measurement.

The final reduction stage signals a steep increase in the fraction of the Li_2S component probed by XANES. It corresponds to the conversion of all the available polysulfides to Li_2S and results in the sudden voltage drop. The overall discharge as probed by XANES can be summarized as the equation:

$$\frac{2}{3}S_8 + \frac{3}{2}Li^+ + \frac{3}{2}e^- \rightarrow \frac{3}{4}Li_2S + \frac{1}{4}S_8$$
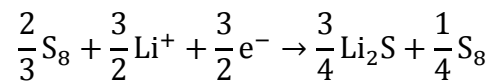
− to account for the persistence of elemental sulfur − whose calculated specific capacity of 1254 mAh.g^{-1}, is in excellent agreement with the electrochemistry (i.e. 1189 mAh.g^{-1}). While the appearance of Li_2S occurs without any notice from an electrochemical perspective, its rapid precipitation at the end of the plateau supports the idea of a mainly sequential mechanism. This could be the cause of the sudden voltage drop (i.e. electrode passivation), as suggested by impedance spectroscopy measurements.[34]
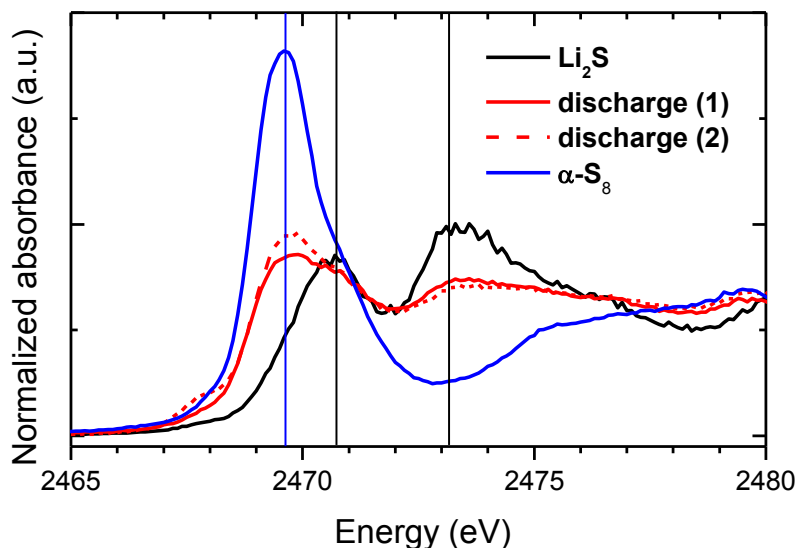
Figure 36. Spectra recorded for the discharged states of the *in situ* cell (red), elemental sulfur reference spectrum (blue) and lithium sulfide reference spectrum (black).

The end of discharge spectra do not exhibit any low energy feature but instead only consist of a mixture of S_8 and Li_2S. The presence of non-reactive elemental sulfur during all the cycling is surprising, but the XANES spectra of the discharged cell are unequivocal as shown in as shown on **Figure 36**. It might be an intrinsic limitation of the Li-S system, and could explain the usual reported capacity around 1200 mAh.g^{-1}.

4.3. Overall conclusions on the investigation of a typical lithium-sulfur system by operando XANES.

This chapter presented the results of the first *operando* XANES study of a lithium-sulfur cell. The preparation of a novel linear polysulfide stabilized in its solid phase, Li_2S_6, and the small distortion achieved by constraining the sulfur (and (poly)sulfides to nanodimensions allowed proceeding through a thorough data analysis of the XANES spectra collected

While the charged state of the cell corresponds to pure elemental sulfur, the end of discharge spectra do not exhibit any low energy feature characteristic of linear chain polysulfides, but instead only consist of a mixture of α-S_8 and Li_2S. Hence, contrary to what has been assumed to date,[20] the presence of insoluble Li_2S_2 or other polysulfides as a final reduction product and as a source of lower than theoretical capacity is not supported by our XANES data. Importantly, the *operando* XANES experiments indicate that the typically reported discharge capacity, which is around 75% of the theoretical value for the first cycles, is not limited by the precipitation of Li_2S, but is instead mostly restricted by unreacted sulfur, which was previously observed by AFM on electrodes prepared from bulk sulfur simply ground with carbon.[11]

During discharge, the stop in α-S_8 consumption coincides with the maximum of polysulfides in solution, thus suggesting that once S_6^{2-} is formed, reduction proceeds much easier through the polysulfides in solution than for either the initial or reformed sulfur, leaving elemental sulfur in reserve. There is a delay in the detection of Li_2S by XANES upon discharge, possibly arising from a weak spectral signature. This delayed formation of Li_2S could explain why previous operando X-ray diffraction/tomography studies failed to identify Li_2S during cell

operation even at the lower potential limit[17] while suggesting that crystalline Li_2S eventually forms upon later equilibration.

The hysteresis between charge and discharge – i.e. the difference in potential of the two mechanisms – is also described by the inherent difference between the steps in the reduction and oxidation processes. On reduction, we observe a fast, but not complete conversion of solid α-S_8 to solution species followed by intermediate redox chemistry in solution that occurs around 2.1 V (low-voltage plateau). This step does not correspond to any structural change detected in XANES. The precipitation of Li_2S happens at the very end of this plateau, resulting in a voltage drop. On the contrary, the oxidation of solid Li_2S proceeds gradually during the large majority of the charge through the soluble intermediates, S_4^{2-} and S_6^{2-}.

4.4. Operando XANES study on PCNS/S- 22 wt%: atypical Li-S system.

The same active material – porous carbon nanosphere (PCNS) filled with 58 wt% of sulfur – was heat-treated at 230 °C to leave only. The resulting material (then containing only 22 wt% sulfur) used as a cathode in a lithium-sulfur cell exhibits an atypical voltage profile that has already been reported in the literature for heat-treated, polymer-based cathode and organo-sulfur materials. However, no clear explanation has ever been given. Again, classical probes failed at elucidating the mechanism and XANES could bring new insights for this behavior.

4.4.1. Heat-treated porous carbon nanospheres.

4.4.1.1. Thermogravimetric analysis (TGA).

TGA was performed under air, which results in sulfur evaporation, followed by the complete oxidation of carbon at temperatures > 450°C. Focusing on the moderate

temperatures (i.e. on sulfur), the TGA of PCNS/S-58 wt% studied in the previous chapter clearly exhibits two regions, as separated by the dotted line on **Figure 37.a**. The differential scanning calorimetry (DSC) is plotted on **Figure 37.b**. It exhibits a pic around 250 °C that corresponds to highly exothermic (i.e. spontaneous) evaporation of sulfur. This 40 wt% loss corresponds to a steep decrease of the sulfur content around 230 °C, while the second 18 wt% loss after 250 °C appears gentler on TGA and liberates less energy on the DSC. This is indicative of two different sulfur environments; the first corresponds to the usual "free sulfur" whereas the second is more confined and/or in stronger interaction with in the carbon host; its vaporization is therefore less easy.

From the TGA and DSC results, the idea was to perform a heat treatment of the PCNS filled with 58 wt% sulfur at 230 °C (at the onset of the exothermic reaction on **Figure 37.b**) during 3 to 5 hours. This heat-treatment should remove the "free sulfur" described above, but leave the more confined sulfur in the material. A second TGA showed that this novel PCNS/S then contained 22 wt% sulfur as shown by the TGA on **Figure 37.a**. The TGA and DSC signatures correspond to sulfur confined in the carbon host as expected.
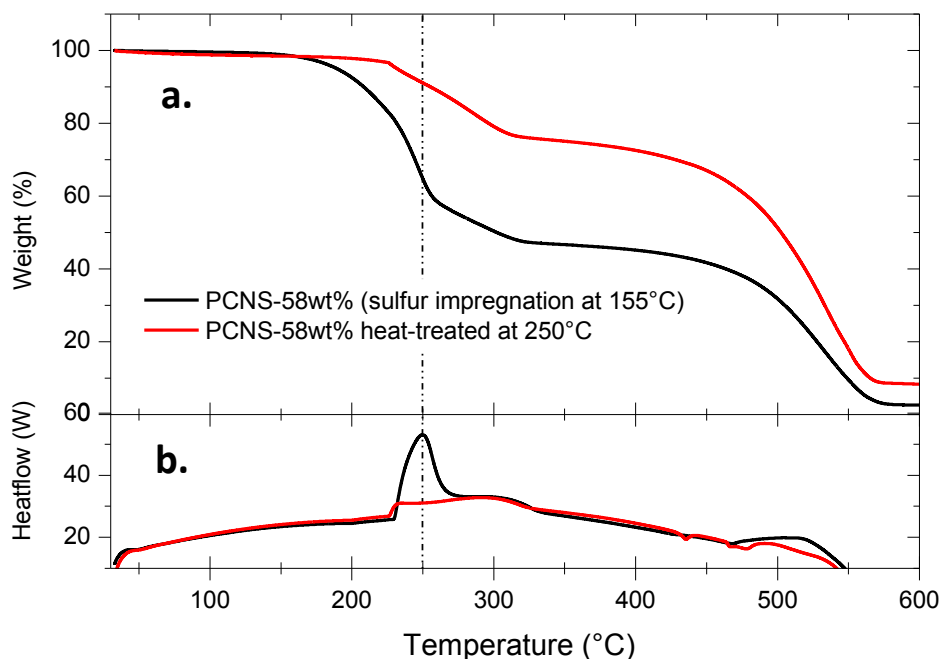
Figure 37. a. Differiential scanning calorimetry and **b.** thermogravimetric analysis under air on the PCNS filled with 58 wt% sulfur (black) and the same carbon/sulfur composite heat-treated at 230 °C (red).

4.4.1.2. Galvanostatic cycling.

PCNS/S- 22 wt% used as a cathode in a lithium-sulfur cell exhibits an unusual voltage profile as shown on **Figure 38**. It consists of a first short decrease between 2.0 V and 2.2 V and then a long slopping curve around 1.8 V. It also features a very high irreversible capacity (around 800 mAh.g^{-1}) between the discharge and the charge on the first cycle. More interestingly, this material is able to cycle in EC:DEC as shown on **Figure 38**, indicating that no sulfur radicals are formed upon cycling since they would attack the electrolyte solvents.[35] It is a strong indication that the heat-treatment leads to a strong interaction between the carbon host and the element sulfur – as already intuited by TGA results, possibly forming organo-sulfur compounds.

84
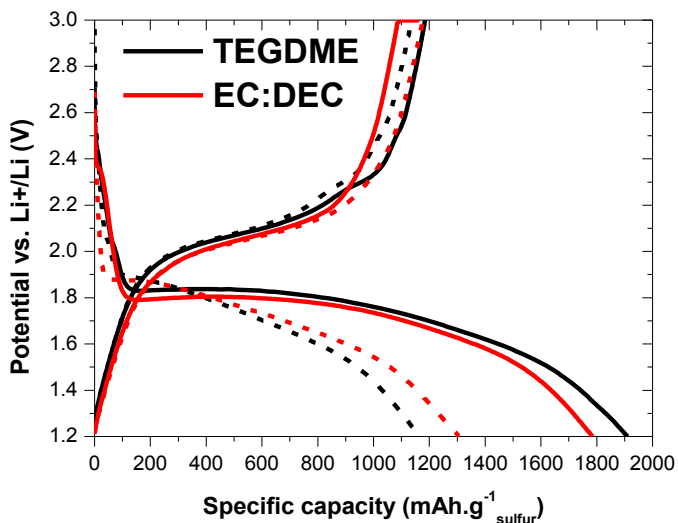
Figure 38. First and second (dashed) cycles of the heat-treated PCNS/S- 22 wt% run in TEGDME (black) and EC:DEC (red) electrolyte solutions.

The electrochemical signature exhibited by this material strongly resembles that presented in the literature for organo-sulfur compounds,[70,71] polymer impregnated with sulfur,[72,73] or heat-treated carbon/sulfur materials.[74,75,76] In all these cases, sulfur was reported to be in intimate interaction with carbon. In fact, the formation of C-S bonds during the heat treatment was claimed based on X-ray photoelectron spectrometry (XPS) measurements[77]. The redox mechanism for organo-sulfur compounds is usually described as scission of C-S**-S**-C bonding to form Li^+**-**S-C bonding – and *vice versa* – during (dis)charge.[70] It has noticeably been observed by changes in XAFS spectra on organo-disulfide.[56]

4.4.1.3. Potentiodynamic cycling on PCNS/S- 22 wt%.

Figure 39 shows the cyclic voltammetry (CV, **a.**) and potentiodynamic cycling with galvanostatic acceleration (PCGA, **b.**) of this active material in TEGDME – 1M LiTFSI. The material exhibits a first reduction peak around 2.45 V, which could be attributed to residual "free" sulfur since it is a typical signature of the reduction of α-S_8 to linear polysulfides; this peak

does not appear in the next cycle. The second reduction peak around 1.8 V must correlate to the irreversible capacity observed during the first galvanostatic cycle, since its intensity decreases drastically in the second cycle. Subsequently, the reduction peak is shifted to 1.9 V and is mostly reversible, as indicated by the integration of cathodic and anodic peaks. On the PCGA curve, it appears more obviously that the prominent discharge peak involves quasi-simultaneously an irreversible biphasic process at 1.95 V and a reversible monophasic one, spread between 1.9 and 1.6 V. The irreversible reduction is not complete after one cycle, and the reversible capacity can be estimated around 800 mA h.g^{-1}.
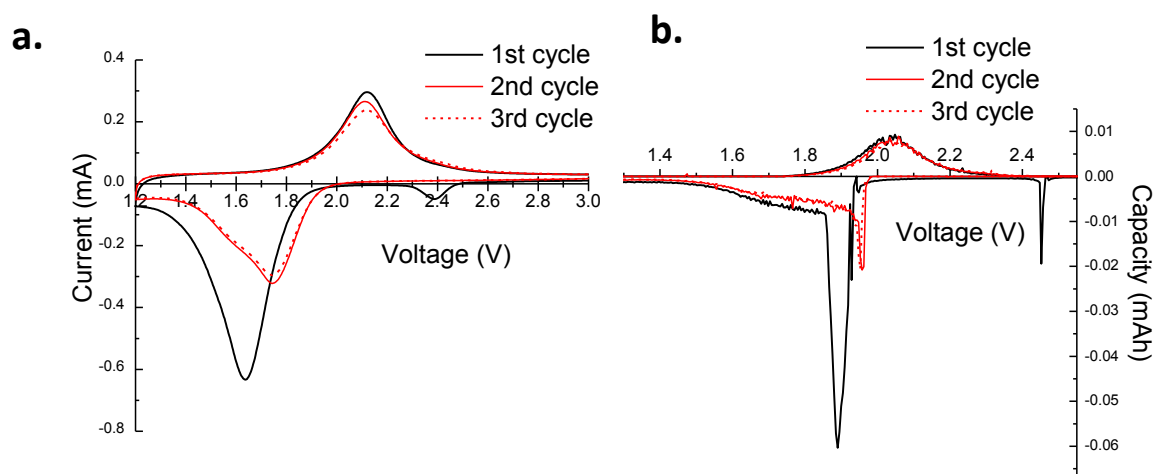
Figure 39. a. Cyclic voltammetry in TEGDME – 1M LiTFSI. **b.** PCGA in TEGDME – 1M LiTFSI

4.4.2. *Operando* XANES results

XANES measurements were performed on this material upon cycling at C/5. The same experimental setup presented in the previous section was used. Similarly to the previous study, the electrochemical behavior was well reproduced in the *operando* cell. **Figure 40.a** presents the 3D plot of the collection of XANES spectra recorded upon cycling. **Figure 40.b** shows a comparison between the pristine and the recharged states of the PCNS/S- 22 wt% cathode.
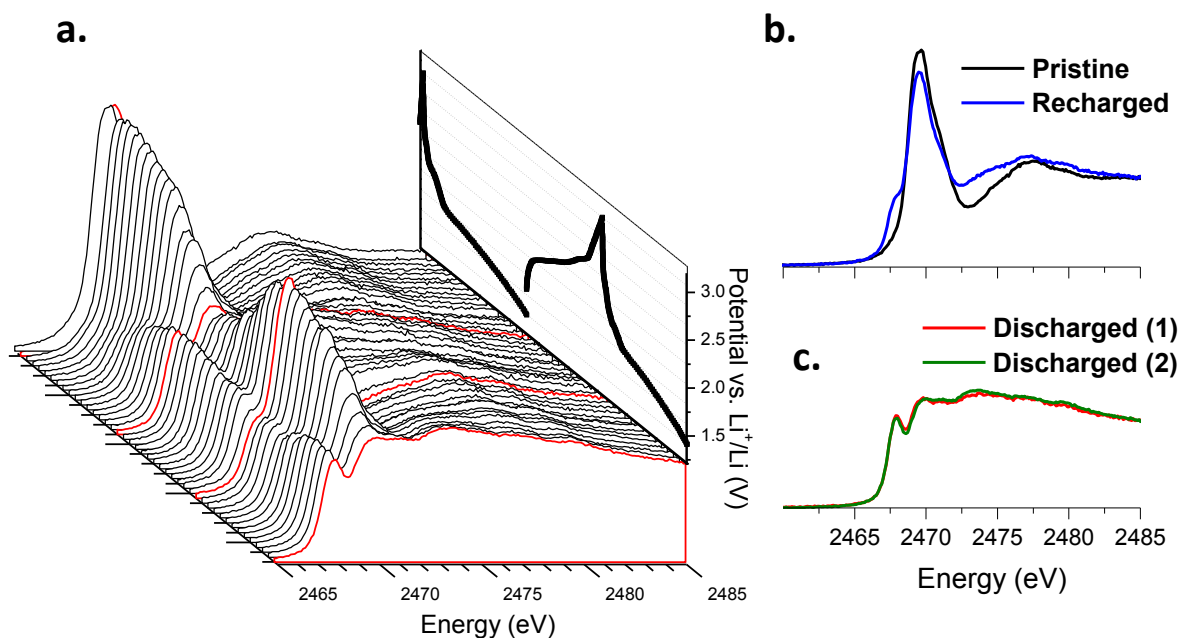
Figure 40. a. Collection of XANES spectra recorded upon cycling. **b.** Comparison between the pristine and the recharged state of the in-situ cell. **c.** Comparison between the two discharged states.

The pristine spectrum corresponds to elemental sulfur (see **Figure 21**, top, for comparison) while the recharged state exhibits a low-energy feature. This difference could correlate with the irreversible process occurring during the first discharge. On the contrary, the spectra of the two discharged states are super-imposable (**Figure 40.c).** It means that there is no structural difference between them whereas there is a difference of 800 mAh.g^{-1} in electrochemistry. It indicates that the charge process is fully reversible. The discharged product exhibits an intense low energy feature that has been assigned to linear chain polysulfides in the previous chapter. Compared to the white-line at 2469.5 eV, its intensity is high so that it corresponds to short chain polysulfides (**Figure 21**, middle).

The previous *in-situ* XANES study of organo-disulfides aforementioned reports the sulfur K-edge in poly(trithiocyanuric acid) electrodes in both charged and discharged states.[56] The

spectra obtained on these organo-sulfides are fairly similar those plotted in **Figure 40.b** and **c.**, in agreement with the assumption of the presence of C-S bonds in the PCNS/S- 22 wt% compound. The main features of the spectra are identical to what can be found in the typical Li-S system investigated in the previous chapter: around 2468 eV, 2469.5 eV, and 2471 eV. Therefore, no novel XANES signature, which could give a direct appreciation of the sulfur local environment, could be shed light on.

The lack of proper reference materials for the heat-treated composite presented in this chapter is a severe hindrance to perform a correct analysis of the XANES data. A first analysis was carried out using LCF with elemental sulfur, Na_2S_2, Na_2S_4, and Li_2S. The LCF results are presented on **Figure 41.a**. It cannot be interpreted literally, but it might still give dsome insight on the electronic structure and/or geometry of the redox species in presence. Li_2S_6 could not be used to describe the evolution of the sulfur K-edge upon discharge, suggesting that the sulfur rings may be smaller than usual (< 8 atoms). The contribution described by Na_2S_2 and Na_2S_4 – blue on **Figure 41.a**, i.e. the low energy feature – increases during the first discharge, stays fairly constant during the charge, and then slightly increases again during the 2nd discharge. It could correspond to the formation of a particular arrangement in the sulfur environment and be linked to the irreversible capacity observed during the first and second discharge. On **Figure 41.b** are shown some selected spectra recorded during the electrochemical process above 1.8 V of the first (top) and second (bottom) discharges. During this part of the discharge no changes are detected by the XANES measurement while it corresponds to a capacity of 400 $mAh.g^{-1}$, and like on the 2.1 V discharge plateau of the typical Li-S cell (see previous section), there is no simple explanation for that. It is however unlikely that similar phenomenon occurs in the two cases: while in the previous study, it could come from a structural delay in the XANES response (the

capacity matches at the end of discharge), in that case it would instead be linked to parasitic reactions that do not involve sulfur, resulting in the irreversible capacity.
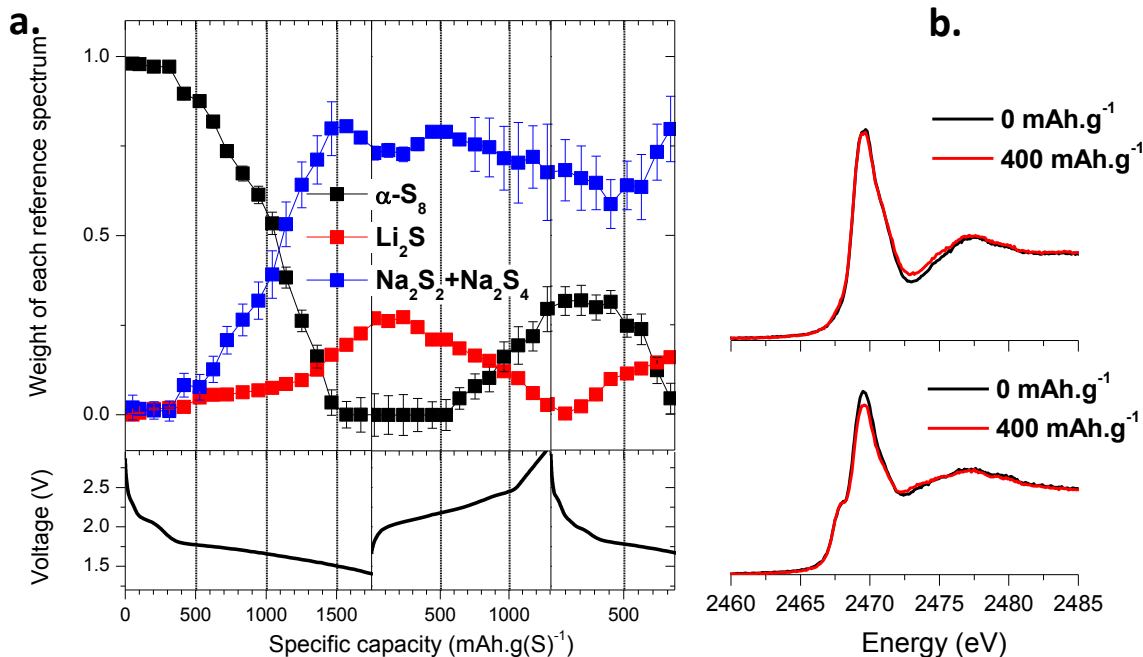
Figure 41. a. Linear combination fit results using elemental sulfur (black), the sum of Na₂S₄ and Na₂S₂ (blue) and Li₂S (red) function of the specific capacity calculated from the electric current. The voltage profile is also plotted on the bottom. **b.** Selected spectra during the first (top) and second (bottom) discharges show the absence of structural evolution on the first 400 mAh.g⁻¹.

4.5. Overall conclusions and future work on the investigation of an atypical lithium-sulfur system by operando XANES.

This section presented the electrochemical study coupled with operando XANES on heat-treated PCNS/S. This material exhibits a particular electrochemical voltage-composition profile that has already been reported in the literature, but never fully explained. TGA and DSC results show that the composite formed after heat treatment at 230°C is probably made of sulfur in an

intimate interaction with the carbon matrix. The electrochemical behavior includes a high initial irreversible capacity, as highlighted by PCGA.

Operando XANES showed a clear evolution at the sulfur K-edge, mimicking the redox behavior. Noticeably, the irreversible reduction process results in a clear structural transformation between the pristine and the recharged state. The XANES features present in the spectra recorded on this redox system are similar to the one recorded in a typical Li-S system. However, their evolution upon cycling is clearly different: the low-energy feature rises during the plateau around 1.8 V of the first discharge and then stays fairly constant, it is still noticeably present in the discharged state. Rather than typical Li_2S_n, it might be linked to the irreversible electrochemical process.

The PCGA gives good insights into the electrochemical processes involved, but the similarities in the XANES features observed between the typical Li-S system and this untypical are disconcerting. It is not a surprise considering previous XANES study on organo-sulfides.[56] A second *operando* XANES experiment was intended during the first week of July 2013. The idea was to perform the XANES measurements during a PCGA to obtain *in situ* reference spectra and to have a more precise XANES signature of the redox chemistry. In addition, chemically reduced and re-oxidized PCNS-22wt% were targeted as *ex situ* reference materials. However, the instability of the X-ray beam during most of the run did not allow performing the experiment. It should be repeated during the next campaign.

5. Exploration of non-aqueous electrolytes for Li-S batteries with low Li_2S_n solvation properties.

This chapter presents the investigation of different families of solvents and their impact on the electrochemical performance of a Li-S cell. The relevant parameters of an electrolyte are its ionic conductivity and its viscosity. In the particular case of the sulfur redox system, between the charged product and the discharged product – α-S_8 and Li_2S, respectively – most of the polysulfides are expected to be in solution. Therefore, the solubility of the intermediate products in the electrolyte should highly impact the phase transitions involved during (dis)charge, and a particular attention should be taken to this parameter.

The approach to formulate novel electrolytes for lithium-sulfur batteries is here based on the compilation of quantitative physico-chemical parameters including the solubility of Li_2S and Li_2S_6. The original synthesis of solid-state, single-phase, Li_2S_6 presented before in this report gives access the solubility of long-chain polysulfides, which is not possible when simply reacting S_8 and Li_2S in solution.

The cathode material used for all this study was made of CMK-3/S (50:50 – 80 wt%), Carbon Black (5 wt%), Carbon Fiber (5 wt%), and PVDF-HFP (10 wt%) as a binder. A particular attention was paid to keep the electrode formulation and loading constant, so that the only variable is the nature of the electrolyte.

5.1. Solvents chosen for this study and their characteristics.

5.1.1. Novel solvent investigated in this study.

5.1.1.1. Glymes.

Glymes are the common class of solvents used in Li-S batteries, they have been investigated since the 1990s.[45] As stated in the introduction chapter, the usual electrolyte is based on DME or TEGDME solvents, which should dissolve polysulfides in a large extent.[78] Compared to DME, TEGDME suffers from a higher viscosity and lower ionic conductivity. Dioxolane (DOL) is often used as a counter solvent because of its capability to protect the lithium electrode, while maintaining a low viscosity.[79] The use of glyme solvent is here extended to solvents provided by the University of Rhode Island (U.R.I.), which consist of the mono- and diglyme with a *trimethylsilyl* group added at one end as shown in **Table 4**. 1,2-dimethyl-1,2-dimethoxybutane, synthesized in the University of Waterloo (UW), is also investigated. The addition of non-polar groups – trimethylsilyl and methyl – makes these compounds more hydrophobic and should reduce the polysulfides solubility. **Table 4** presents them and the labels used in the following.

1NM(1-2) compounds are already reported in the literature.[80] All three compounds solubilize LiTFSI salt in a large extent, so that (solvent)$_2$:Li or (solvent):Li molecular complexes could be formed. However, 1 wt% LiNO$_3$ could only be solubilized in 1NM2, but neither in 1NM2 nor in DMDMB. The solubility of other salts such as LiPF$_6$ or LiClO$_4$ was not tested.

Name	Formula	Label	Source
Monotrimethylsilated monoglyme (n=1)		1NM1	URI
Monotrimethylsilated diglyme (n=2)		1NM2	URI
1,2-dimethyl-1,2-dimethoxybutane		DMDMB	UW

Table 4. Glyme derivatives synthesized and under evaluation as Li-S electrolyte solvents.

5.1.1.2. Nitriles and specifically acetonitrile.

A second solvent was also explored following the example of Yamada *et al.* who showed that by saturating acetonitrile (ACN) solutions with LiTFSI, those became stable in regards to metallic lithium.[81] $(ACN)_2$:LiTFSI molar ratio was chosen from previous study of complexed TFSI by ACN.[82] It does not dissolve metallic lithium anymore, as shown in **Figure 42** after one month of immersion. However, such complex is not expected to exhibit high conductivity and Li^+ transport. On the other hand, if solvent molecules are effectively prevented from reacting with metallic lithium, one can also presume of the total absence of solubility for polysulfides.

Figure 42. Metallic lithium immersed in a $(ACN)_2$:LiTFSI solution for one month.

5.1.2. Characterization of these electrolytes.

5.1.2.1. Viscosity and conductivity.

The viscosity and ionic conductivity of LiTFSI solutions of the solvents presented above used as electrolytes (fully complexed or with 1 M LiTFSI, as commonly used) are indicated in **Table 5**. The viscosity was measured using a µVISC viscometer and the ionic conductivity with a ORION STAR conductimeter. All the ionic conductivities of the novel electrolytes are significantly lower (0.615 mS.cm^{-1} for (DMDMB)$_2$:LiTFSI, 1.352 mS.cm^{-1} for (ACN)$_2$:LiTFSI) than the one of DOL:DME (1:1) – 1M LiTFSI, which was measured at 10.8 mS.cm^{-1} in perfect agreement with the value found in the literature.[48] As one can expect, their viscosities on the contrary are much higher than the one of DOL:DME (160 cP for (DMDMB)$_2$:LiTFSI, 138 cP for (ACN)$_2$:LiTFSI). For comparison, EMS was also measured. It was used in the past as an electrolyte for Li-S cell,[83] but was then discarded for its too high viscosity/low ionic conductivity.

Electrolyte	Ionic conductivity (mS.cm^{-1})	Viscosity (cP)
DOL:DME (1:1) – 1M LiTFSI	10.8	2.17
DMDMB:LiTFSI (2:1)	0.615	160
1NM1 – 1M LiTFSI	1.4	-
1NM2 – 1M LiTFSI	2.5	-
TEGDME – 1M LiTFSI	2	13.0
ACN:LiTFSI (2:1)	1.352	138
EMS – 1M LiTFSI	2.25	23.3

Table 5. Ionic conductivity and viscosity of the electrolytes studied in this chapter.

5.1.2.2. Lithium polysulfides solubility.

Li$_2$S$_6$ was dissolved in the solvents presented in the previous section until saturation of the liquid, i.e. the first appearance of a precipitate. A methylation agent, methyl

trifluoromethaesulfonate ($CF_3SO_3CH_3$, MeTf), was then used to stabilize Li_2S_n in solution. Its addition in the polysulfide solution leads to the following reaction:

$$S_n^{2-} + 2\ CF_3SO_3CH_3 \rightarrow CH_3S_nCH_3 + 2\ CF_3SO_3^-$$
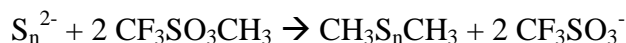
Dimethyl sulfides – Me_2S_n – offer the benefit of being stable in air and aqueous solutions. However, this reaction may be accompanied by the hydrolysis of MeTf as described by the reaction:

$$CF_3SO_3CH_3 + H_2O \rightarrow CF_3SO_3^- + CH_3OH + H^+$$

The formation of protons is not wanted since they can react with the lithium polysulfide species and modify chain length, i.e. the polysulfides distribution in solution. To prevent further disproportionation reactions from occurring, a $1\ mol.L^{-1}$ buffer solution (pH = 7) was prepared from Na_2HPO_4 and NaH_2PO_4 in deoxygenized water and added to the reaction.

Although the original method was developed by Argyropoulos *et al.* to investigate alkaline aqueous solutions,[26] similar methylation procedure was employed by Barschasz *et al.* to study Li_2S_n in a catholyte cell by high-performance liquid chromatography (HPLC). The ^{1}H NMR method was preferred for the possibility to probe concentrated solutions. By this technique, it is possible to differentiate the different $CH_3S_nCH_3$ from their characteristic chemical shifts as shown on **Figure 43.a**., it allows quantifying the distribution of polysulfides in solution as shown on **Figure 43.b**.1,3,5-tributyl benzene in $CDCl_3$ is used as an internal standard to calibrate the integration and know the precise amount of Li_2S_6 solubilized.
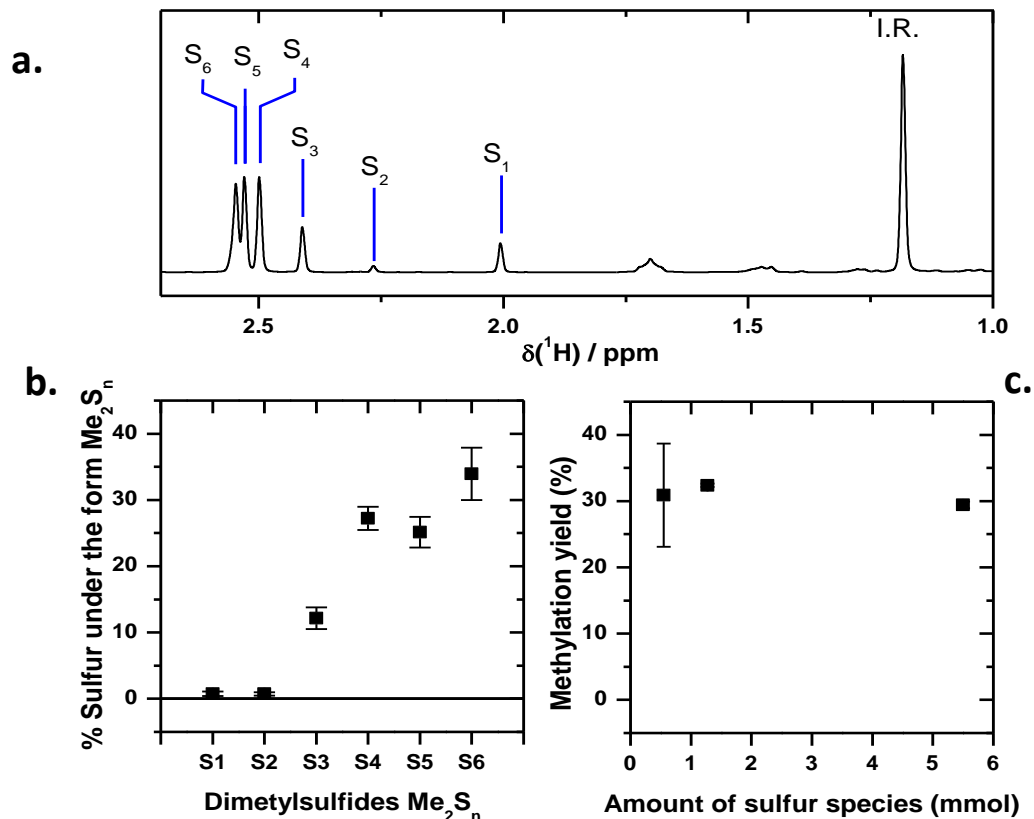
Figure 43. a. Illustrative 1H NMR spectrum, **b.** Average distribution of sulfides in the Me_2S_n solutions obtained by reacting Li_2S_6 in DOL:DME (1:1) . **c.** Methylation yield as a function of amount of sulfur species put in solution.

A first set of experiments using $0.25 - 1$ mmol of Li_2S_6 in DOL:DME (1:1) was necessary to optimize the amount of the different reagents, the order and duration of their addition, and to determine the yield of the procedure, which was found around 30% (see **Figure 43.c**). All the experiments are carried out under argon atmosphere. 0.5 mL of the buffer solution is first added quickly, and then the solutions of MeTf (0.5 mL) and the internal standard 0.05 M in $CDCl_3$ (1.0 mL) are added drop wise over approximately 5 minutes. The reaction mixture is then stirred for 90 minutes. Discoloration was found to be a reliable indicator of reaction completion.

Solvent	Li_2S_6 solubility in $mol_{sulfur} \cdot L^{-1}$	Li_2S solubility in $mol_{sulfur} \cdot L^{-1}$
DOL	55	-
DME	61	-
TEGDME	7.5	0.03
1NM1	36	0.08
1NM2	7.5	0.03
DMDMB	1.5	0.13

Table 6. Solubility of Li_2S_6 and Li_2S in mol of sulfur per liter for the glyme solvents investigated.

Table 6 reports the results of Li_2S_6 and Li_2S solubility tests performed on glymes solvent: DOL, DME, TEGDME, 1NM1, 1NM2, and DMDMB. The solubility of Li_2S is increased in the new solvents investigated, especially for 1NM1 and DMDMB. Although all values are extremely low, any increase would facilitate the formation and the consumption of Li_2S on the positive electrode surface and beneficiate to the performance of the cell. The Li_2S_6 solubility values are high to extremely high – DMDMB exhibits the lowest with 1.5 mol(S).L^{-1} – so that the electrolyte saturation in soluble polysulfides in unlikely to occur in a confined Li-S cell where the full dissolution of the active material in the overall electrolyte volume would result in a ≤ 0.5 mol(S).L^{-1} concentration. However, depending on the capability of Li_2S_n to migrate fast enough compared to the redox reactions, the volume to consider could be much less than that.

The dissolution of polysulfides in the electrolyte during cycling is expected to have an impact on the ionic conductivity of the electrolyte. To quantify this impact, Li_2S_6 has been added to selected electrolytes based on mixture of DOL and another solvent (all ratio given are volume ratio, see next section for their electrochemical performance). In the case of DMDMB, the complex $DMDMB_2$:LiTFSI is replaced by DMDMB alone in the notation for convenience. On **Figure 44.a** is plotted the measure of the ionic conductivity of DOL:DME (1:1), DOL:TEGDME (1:1), DOL:1NM1 (1:1), and DOL:DMDMB (1:1) upon the addition of Li_2S_6. **Figure 44.b** shows the conductivity retention, where the value for [S] = 0 mol.L^{-1} is set to 1. All the electrolytes

exhibit the same behavior, with a conductivity decrease that becomes severe after $1mol_{(S)}.L^{-1}$, which is higher than the maximum concentration of sulfur possible in a Li-S cell. Note that in the case of DOL:DMDMB (1:1), the ionic conductivity slightly increases first. This could come from a slight deviation from the (2:1) molar ratio targeted when the complexing DMDMB with LiTFSI. These examples show that the dissolution of polysulfides should not have a severe impact on the global electrolyte characteristics, except in the case of local dissolution.
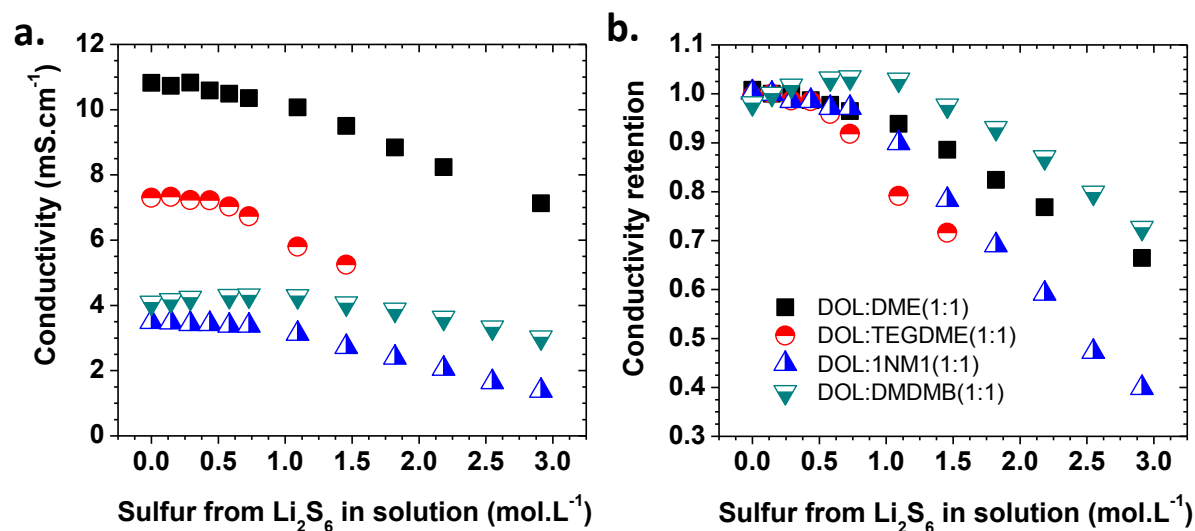
Figure 44. a. Evolution of the ionic conductivity upon the addition of Li_2S_6 of selected electrolytes : DOL:DME(1:1) (black), DOL:TEGDME(1:1) (red), DOL:1NM1(1:1) (blue), and DOL:DMDMB (1:1) (green). **b.** Ionic conductivity retention upon the addition of Li_2S_6.

In the particular case of ACN, no methylation could be performed. Lithium polysulfides and Li_2S solubilities were first investigated by putting approximately 10 mg of Li_2S_6 and Li_2S in 0.5 mL of $(ACN)_2$:LiTFSI. The pictures of the vials for Li_2S_6 and Li_2S are displayed on **Figure 45.a** and **.b**, respectively. The two compounds seem to have a really low solubility in the electrolyte.

Figure 45. Pictures of **a.** Li$_2$S$_6$ and **b.** Li$_2$S in (ACN)$_2$:LiTFSI.

5.1.3. Conclusion.

The purpose of this chapter is to investigate new solvents for the electrolyte in a Li-S cell. The novel solvents 1NM1, 1NM2, and DMDMB − provided by U.R.I. or co-workers at U.W − are glymes which is a typical solvent family used in Li-S electrolytes, but the addition of non-polar groups *methyl* and *trimethylsilyl* decreases the polysulfides solubility. However, it is still high enough to dissolve all the sulfur present in a standard cathode. The presence of non-polar groups also increases Li$_2$S solubility noticeably for 1NM1 and DMDMB. The solubility of Li$_2$S and Li$_2$S$_6$ could not be measured in ACN$_2$:LiTFSI using the same route as for other solvents, but they should be particularly small, which makes this electrolyte particularly interesting.

All the electrolytes proposed exhibit a low ionic conductivity and a high viscosity compared to DOL:DME (1:1) − 1M LiTFSI, so that their electrochemical performances are not suitable. EMS − 1M LiTFSI and TEGDME − 1M LiTFSI, which exhibit similar characteristics, have been discarded or mixed with other solvents by the past.[48]

5.2. Utilization of DOL as a counter solvent.

A first approach to use 1NM1, 1NM2, and DMDMB as effective electrolyte was to mix them with DOL since it is a common strategy to investigate new electrolyte solvents.[48]

5.2.1. Effect on the physico-chemical parameters

It is expected that the addition of DOL as a counter solvent will increase the ionic conductivity and decrease the viscosity of the electrolyte.[48] The ionic conductivity of different ratio of 1NM1:DOL is reported in **Table 7**, and, as expected, exhibits a significant increase from 1.4 mS.cm^{-1} for pure 1NM1 – 1M LiTFSI to 3.63 mS.cm^{-1} for 1NM1:DOL (1:9). This example shows that the use of DOL as a counter solvent should allow using 1NM1, 1NM2, and DMDMB in a Li-S cell.

(1NM1:DOL)	1:0	1:1	1:2	1:3	1:6	1:9	0:1
Ionic conductivity (mS.cm^{-1})	1.4	2.66	3.02	3.21	3.45	3.63	4

Table 7. Ionic conductivity of different ratios of 1NM1 :DOL from pure 1NM1 to pure DOL.

5.2.2. Electrochemical performance of different ratio DOL:SOLVENT.

In the following are reported results obtained with DME:DOL (1:1), TEGDME:DOL (1:1), DMDMB:DOL in the volume ratios (1:1), (1:3), (1:5), (1:9), 1NM1:DOL (1:1) and (1:3). The first and 5th discharges are shown in **Figure 46**. The electrochemical profile is similar for all the different electrolytes, and is typical of Li-S system. A first plateau around 2.3-2.4 V is characteristic of the reduction reactions from S^0 to S$_4^{2-}$, resulting in the dissolution of long-chain polysulfides. The second plateau is a liquid-solid redox reaction during which Li$_2$S precipitates at the positive electrode. All the electrolytes exhibit a more or less marked super-saturation point

around 400 mAh.g^{-1}. One can notice that the electrolytes based on 1NM1 and DMDMB show the least pronounced super-saturation point, suggesting that the formation of Li$_2$S is easier in these solvents.
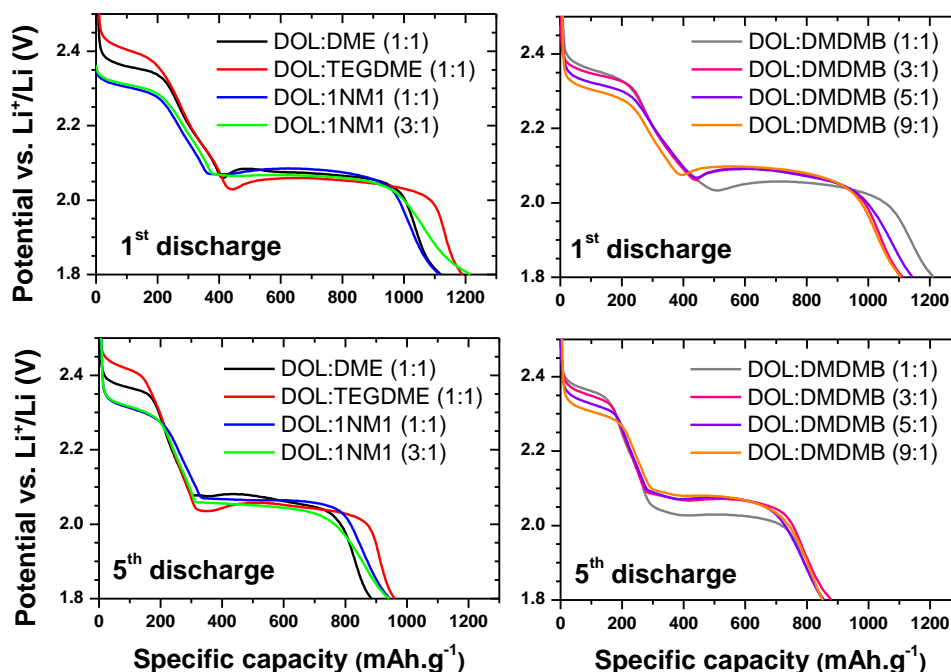
Figure 46. 1st and 5th discharges of a CMK-3/S (50 wt% S) electrode at C/5 in various electrolytes.

The capacity retention over 100 cycles is shown in **Figure 47** for the different cells. DME:DOL (1:1) appears to be the best electrolyte regarding this criterion with a discharge capacity retention of 62% after the 100th cycle. 1NM1:DOL (1:1) retains more capacity during the first twenty cycles, but the capacity then fades below DOL:DME and ends at ~50% of the initial capacity. TEGDME:DOL (1:1), DMDMB:DOL (1:9), and 1NM1:DOL (1:3) exhibit the same behavior with a capacity retention of ~50%. Higher percentages of DMDMB mixed with DOL show a faster capacity drop upon cycling. Hence, it seems that increasing the electrolyte hydrophobicity is unfavorable to capacity retention.
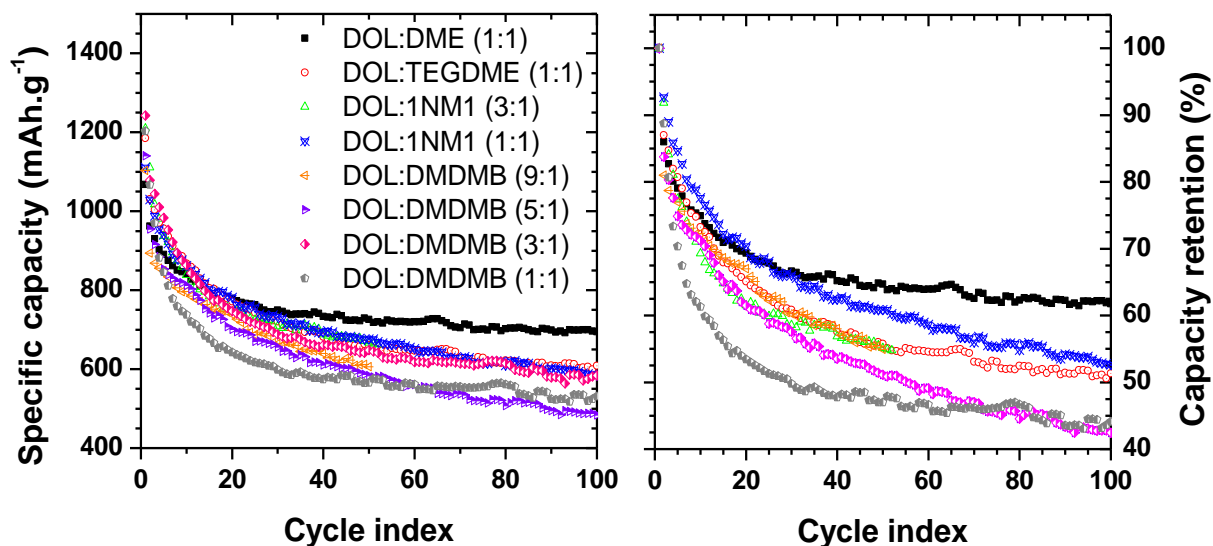
Figure 47. Specific capacity **(left)** and capacity retention **(right)** at C/5 in various electrolytes.

5.2.3. Discussion on the causes of loss of capacity.

Although all electrolytes exhibit a $\sim$20% capacity loss during the first five cycles, such loss should be attributed to different phenomena. For the sake of clarity it was decided to distinguish the loss on the first plateau of discharge (P1) and the one on the second plateau (P2), corresponding to the reduction reactions from S_8 to S_4^{2-}, and to the precipitation from S_4^{2-} to S^{2-}, respectively. These two reduction steps are described by the overall reactions and the specific capacities:

P1 : $\qquad\qquad$ $S_8 + 4\,e^- \rightarrow 2\,S_4^{2-}$ $\qquad\qquad$ $C_1 = \dfrac{4 * e * F}{8 * M_S}$

P2 : $\qquad\qquad$ $S_4^{2-} + 6e^- \rightarrow 4\,S^{2-}$ $\qquad\qquad$ $C_2 = \dfrac{6 * e * F}{4 * M_S}$
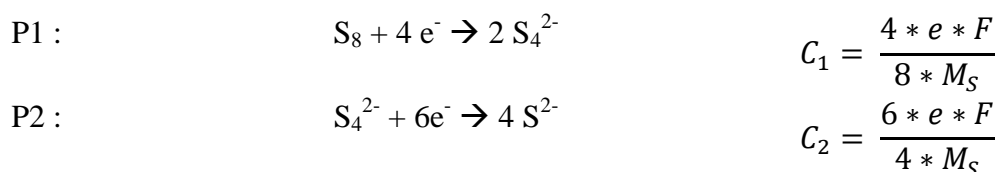
In theory, $C_2/C_1 = 3$, i.e. a loss of capacity on P1 should lead to a subsequent loss three times higher on P2.

102

In general, the loss of capacity could be attributed to different mechanisms:

1. Active material under the form of long-chain polysulfides is lost in the electrolyte and inside the separator so that it cannot participate in the redox processes during the following cycles. This loss on P1 - directly impacting P2 by a factor of 3 - is accentuated by a low ionic conductivity and the repulsive interactions between hydrophobic cathode interface and hydrophilic long-chain polysulfides.

2. The final charge product is not α-S_8 but soluble long-chain polysulfides instead, i.e. the charge is not complete. It results in a loss on P1 in the following discharge that does not impact the length of the second plateau if these Li_2S_n can still reach the cathode by diffusion to be reduced and form Li_2S.

3. Active material under the form of Li_2S is lost by decrepitation and/or loss of electronic contact.

Figure 48 shows the percentage of the total discharge capacity loss assigned to each of the two plateaus, i.e. $\Delta P1(\%)$ and $\Delta P2(\%)$. As it happens, the more hydrophobic the electrolyte is – DMDMB:DOL (1:5), DMDMB:DOL (1:3), 1NM1:DOL (1:1) –the more this loss is observed on the second plateau. The ratio $\Delta P1(\%):\Delta P2(\%)$ approaches the expected value of 25:75 (for instance, 29:71 for DMDMB:DOL (1:1)), which means that after their formation, Li_2S_n do not convert to Li_2S (mechanism #1). For less hydrophobic electrolytes such as DOL:DME, TEGDME, and DOL:DMDMB (9:1), this $\Delta P1(\%):\Delta P2(\%)$ ratio is instead closer to 50:50, implying that the loss of capacity on P1 is not fully impacted on P2. After the five first cycles, the loss of capacity tends to equilibrate between the two plateaus, between 40:60 and 50:50 for all the electrolytes.
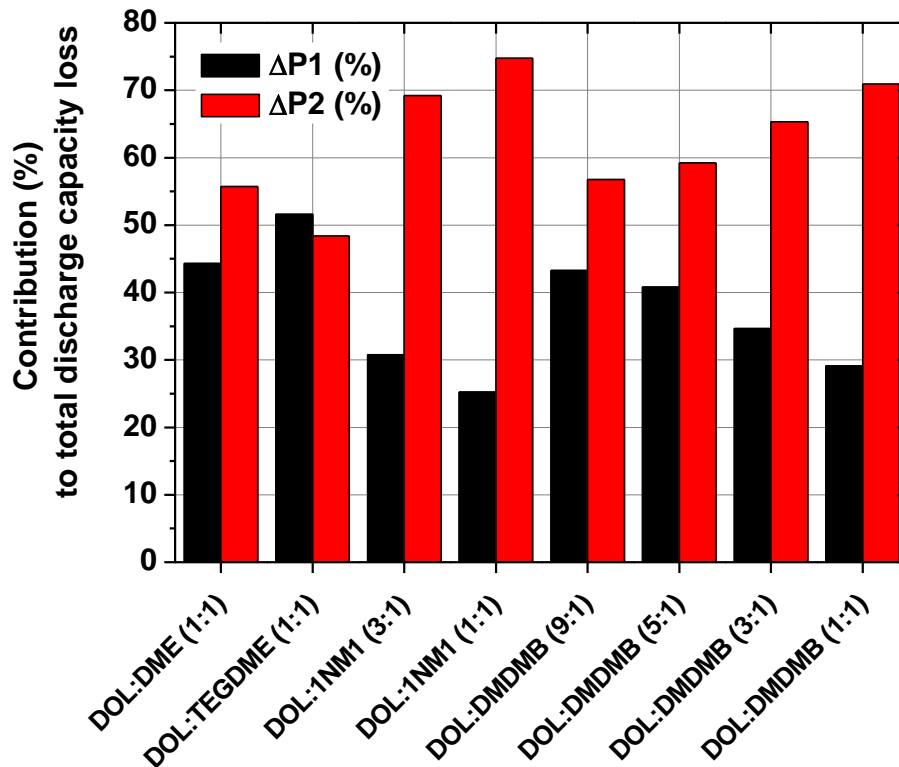
Figure 48. Contribution of capacity loss on the high voltage (P1) and low voltage (P2) plateaus to the overall capacity loss over the first five cycles in selected electrolytes.

The two kinds of behavior observed during the first five cycles can be linked to the electrolyte hydrophobicity. The first kind of electrolytes correspond to DOL:DME, TEGMDE:DOL, and DMDMB:DOL (1:9). Since these electrolytes are highly conductive - 11 mS.cm^{-1} for DOL:DME – there is little chance that the major loss of capacity can be due to a loss of active material – i.e. a mass transport issue – in the electrolyte and in the separator. As it happens, when the reduction of long-chain polysulfides takes place in the cathode, the gradient of Li$_2$S$_n$ concentration has to be balanced by mass transport in order to provide polysulfides to the reduction reaction on the cathode. The higher the mobility, the more available polysulfides there will be. It can explain that the ratio $\Delta P1(\%):\Delta P2(\%)$ is close to 50:50 in the first cycles. The loss of capacity cannot be mostly due to mechanism #1, but is a result of mechanisms #2 and #3.

The other electrolytes all have a lower ionic conductivity and are more hydrophobic. In such electrolytes, the loss of polysulfides in the electrolyte and in the separator would be more important. There is little reason why the polysulfides in solution would diffuse through a low-mobility medium towards the cathode, which is highly hydrophobic in our case. In these systems, the mass transport is slow compared to the reduction reactions and will limit the redox process. The second plateau is therefore more significantly limited by the loss on the first plateau than for highly conductive electrolytes through mechanism #1. However, the ratio $\Delta P1(\%):\Delta P2(\%)$ is higher than 25:75 suggesting that the loss of capacity is now a combination of mechanism #1, #2, and #3 during the five first cycles.

Upon more extended cycling, in all cases the $\Delta P1(\%):\Delta P2(\%)$ ratio is then closer to 40:60, suggesting that the system is reaching an equilibrium for the losses. This equilibrium corresponds to the initial state of highly conductive electrolytes. The loss is mostly due to mechanisms #2 and #3 indicating that the loss of active material in the electrolyte (#1) is not the most important mechanism. One can believe that the electrode decrepitation and the loss of electronic contact will be so important that the polysulfides in solution will always be in excess regarding the number of redox sites available on/in the cathode. These conclusions are in agreement with recent studies that show that the concentration of Li_2S_n in the electrolyte is constant over long-term cycling.[17, 18]

5.2.4. Conclusion.

In this section, glyme solvents were investigated as electrolyte using DOL as counter solvent. However, none of the novel formulation could outclass standard DOL:DME (1:1) Moreover, the best results were obtained with the highest content of DOL that corresponds to the

highest ionic conductivity. All the solvents investigated here solubilize polysulfides, and the addition of DOL should even increase their solubility. It appears that, once in solution, high ionic conductivity is suitable for further polysulfides reduction. Then, their participation in the capacity fading over long-term cycling is not important. From these perspectives, a *good* electrolyte for a Li-S cell should ensure a high ionic mobility (i.e. a maximal solubilization of polysulfides) or should not solvate polysulfides at all.

The characteristics of DOL look predominant in the mixtures prepared in this section, and DME is the best co-solvent regarding the collection of solvents investigated in this section. Therefore, using DOL as a counter solvent could mitigate the particular characteristics in terms of (poly)sulfides solubilities of the novel solvents investigated.

5.3. Use of fluorinated additive to decrease the viscosity.

Electrolytes were blended with 1,1,2,2-Tetrafluoroethyl 2,2,3,3-tetrafluoropropyl ether (HFE) to decrease their viscosities as reported by Wanatabe *et al.* in the case of the TEGDME:LiTFSI equimolar complex.[84] HFE should not participate in the solvation, and therefore should not alter the characteristics of the novel solvents investigated. The evolution of both the viscosity and the ionic conductivity upon HFE addition to *solvent:LiTFSI* was investigated for DMDMB, EMS, ACN, and TEGDME. A particular attention was paid on ACN and DMDMB since they exhibit the lowest Li_2S_n solubility.

5.3.1. Effect on the physic-chemical parameters: viscosity measurements.

Figure 49 shows the evolution of viscosity upon HFE addition. The viscosity of DOL:DME (1:1) - 1M LiTFSI is indicated as a reference. It appears that the effect of HFE addition is different from one electrolyte to another. For instance, the viscosity stays reasonably

constant for TEGDME around 10 cP from 0 vol% to 75 vol%. While the addition of HFE in EMS lowers the viscosity from 23 cP to 10 cP, the impact is much more significant for (DMDMB)$_2$:LiTFSI) and (ACN)$_2$:LiTFSI, but in these cases the concentration of salt decrease upon addition. The first addition of 25 vol% decreases the viscosity from 140 cP to 25 cP for ACN and from 160 cP to around 4 cP for DMDMB. A higher HFE fraction continues to decrease the viscosity for ACN to reach around 4 cP for 66 vol%; on the contrary, the viscosity stays relatively constant for a higher ratio HFE: [(DMDMB)$_2$:LiTFSI)].
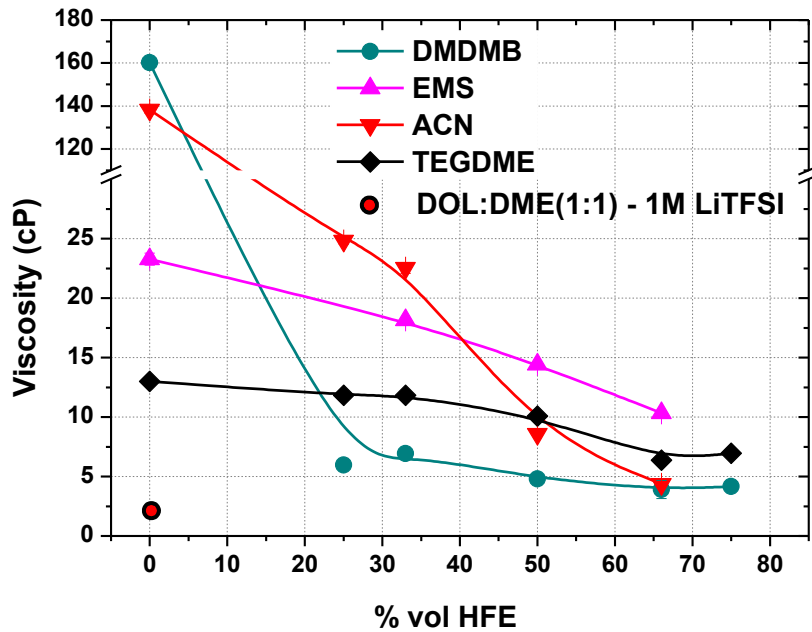
Figure 49. Evolution of viscosity upon HFE addition in solvent:LiTFSI solutions for DMDMB, ACN, EMS, and TEGDME.

It is interesting to notice that all these electrolytes reach a viscosity between 5 and 10 cP for a ratio HFE:solvent of 2:1 (66 vol%), although DOL:DME (1:1) remains the less viscous solution (2 cP). These results show that the addition of HFE is effective to decrease the viscosity, which opens a new perspective for using electrolytes with the specificity of a very low solubility of Li$_2$S$_n$ in Li-S cell.

5.3.2. Effect on the physic-chemical parameters: ionic conductivity measurements.

The variation of the bulk ionic conductivity upon the addition of HFE is also investigated. Since it is assumed that HFE does not participate in the solvation process (from the negligible solubility of LiTFSI), one can expect that too much HFE would decrease the ionic conductivity. This is confirmed in **Figure 50** where the ionic conductivity is plotted as a function of HFE volume fraction.
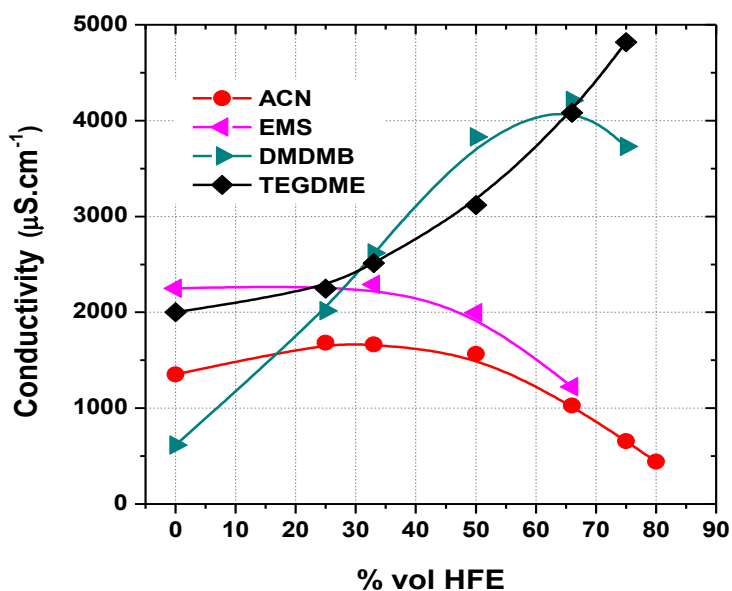
Figure 50. Evolution of conductivity upon HFE addition in LiTFSI solutions of DMDMB, ACN, EMS, and TEGDME.

The results shed light on different behaviors depending on the solvent used. For EMS, the addition of HFE has a negative impact on the ionic conductivity. The effect is also not clearly positive for ACN even if a maximum can be seen around 33 vol% of HFE. However, the addition of HFE significantly increases the ionic conductivity of TEGDME and DMDMB based LiTFSI solutions. No maximum can be observed for TEGDME, but the ionic conductivity increases from 2 mS.cm^{-1} to almost 5 mS.cm^{-1} when HFE increases from 0 vol% to 75 vol%. Last,

HFE:DMDMB exhibits a maximum around 4 mS.cm^{-1} for 66 vol% of HFE, corresponding to eight times the ground conductivity of (DMDMB)$_2$:LiTFSI (0.6 mS.cm^{-1}). For the comparison, DOL:DME (1:1) exhibits a conductivity of 10.4 mS.cm^{-1}, which is two times higher than any formulation prepared with HFE.

5.3.3. Effect on electrochemical impedance of the cell.

The effect of HFE addition on the impedance of the pristine cell was also investigated for pure (ACN)$_2$:LiFSI, DOL:DME (1:1) 1M LiTFSI and ratios of (ACN)$_2$:LiTFSI and HFE of (1:2), (1:1), and (2:1) – denoted simply ACN:HFE (1:2), ACN:HFE (1:1), and ACN:HFE (2:1) in the following. The electrochemical impedance measurements were conducted on a BioLogic VMP 3. The scanning frequency ranged from 250 kHz to 20 mHz and the alternating voltage amplitude was set to 10 mV. **Figure 51** shows the Nyquist plots of the Li-S cells using the electrolytes listed above. The frequencies are indicated for ACN: HFE (1:1) (green).
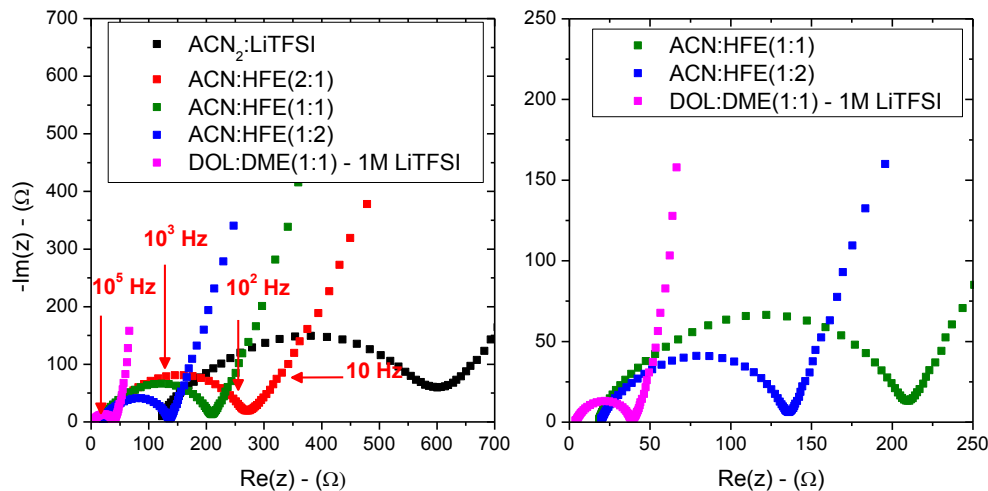
Figure 51. Nyquist plots of Li-S cells using as electrolyte : DOL :DME (1 :1) – 1M LiTFSI, (ACN)$_2$:LiTFSI, ACN:HFE (2:1), ACN:HFE (1:1), and ACN:HFE (1:2). The right panel is only a magnification on the central area.

All the impedance diagrams have the same shape, which consists of a semi-circle at high frequencies (HF) and a straight slopping line at lower frequencies (LF). Such Nyquist plots are typical in Li-S batteries.[12,34] The very high frequency (VHF) response is mostly linked to the ionic conductivity of the electrolyte and is modeled by a pure resistance (R_{VHF}). The HF semi-circle is the signature of a charge-transfer mechanism that occurs at the surface of the electrode. It highly depends on how the electrolyte wets the cathode, which is linked mostly to its viscosity and to a lesser extent, to its hydrophobicity. Its equivalent circuit is a Constant Phase Element (CPE_{HF}) parallel to a resistance (R_{HF}). The CPE is here preferred to a pure capacitor to represent the non-ideal behavior of the electrode due to its porosity and the roughness of the surface. The LF straight line comes from the blocking character of the pristine cathode, and is equivalent to a pure capacitance (C1). **Figure 52** presents the equivalent circuit representative of the electrochemical impedance measurements. The fit results of R_{VHF}, R_{HF}, and CPE_{HF} are listed in the bottom, they are normalized by the cathode surface (2 cm²), for each value the error is < 0.5 %.
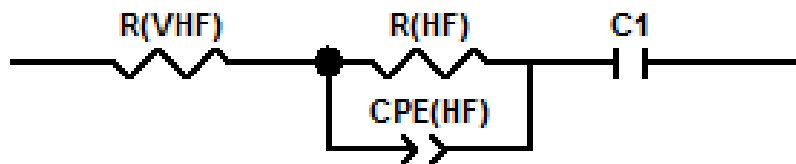
Electrolyte	R_{VHF} ($\Omega.cm^{-2}$)	R_{HF} ($\Omega.cm^{-2}$)	CPE_{HF} T and P	
DOL:DME (1:1)	1.93	18.0	1.5E-5	0.38
$(ACN)_2$:LiTFSI	58.2	260	0.70E-5	0.32
ACN:HFE (1:2)	9.60	60.2	0.85E-5	0.37
ACN:HFE (1:1)	8.72	99.5	0.69E-5	0.37
ACN:HFE (2:1)	11.8	128	0.64E-5	0.35

Figure 52. Equivalent circuit used to fit the electrochemical impedance measured (Nyquist plot presented on **Figure 51**), and the results of the fit for the set of electrolytes studied.

The cell using DOL:DME (1:1) − 1M LiTFSI exhibits as expected the lowest values for R_{VHF} and R_{HF}, showing that its high ionic conductivity lower the resistance due to the electrolyte and that its low viscosity lower the resistance associated with the charge-transfer. On the opposite, pure $(ACN)_2$:LiTFSI exhibits the highest values of 58.2 $\Omega.cm^{-2}$ for R_{VHF} and 260 $\Omega.cm^{-2}$ for R_{HF}, which is expected as this electrolyte suffers from its high viscosity (140 cP). The evolution of both parameters upon HFE addition is reflected by the impedance of the cell :

➢ The ionic conductivity of the three mixtures does not vary much. This is reflected by the little change in R_{VHF} from 11.8 $\Omega.cm^{-2}$ to 8.72 $\Omega.cm^{-2}$ for ACN:HFE (1:2) and ACN:HFE (1:1), respectively. This variation is not significant and could come from slight cell-to-cell variations.

➢ R_{HF} decreases significantly upon the addition of HFE: 128 $\Omega.cm^{-2}$, 99.5 $\Omega.cm^{-2}$, and 60.2 $\Omega.cm^{-2}$ for the ratio (1:2), (1:1), and (2:1), respectively. This decrease is correlated with the clear decrease of the viscosity (**Figure 49**). It shows that a low viscosity results in a better wetting of the cathode.

5.3.4. Effect on the electrochemistry.

The addition of HFE in $(DMDMB)_2$:LiTFSI finally allowed cycling the cell in the absence of DOL as shown on **Figure 53(left)**. The peculiar discharge profile during the first cycle suggests a significant polarization, with the super-saturation visible around 400 $mAh.g^{-1}$ but down to 1.8 V. Voltage increases back to 2.0 V, but the second "plateau" is then extremely short. Last, the slope in the end of discharge is the only feature that is reproduced on the subsequent cycles. Noteworthy, the charge process does not seem to suffer from an over-potential, showing that the oxidation of Li_2S is easier in this electrolyte probably because of its enhanced solubility.

In comparison, the cycling curves (**Figure 53(right)**) in the $(ACN)_2$:LiTFSI based electrolyte display a significant polarization ($E_{disch} \approx 1.8$ V and $E_{ch} \approx 2.5$ V) but a remarkable capacity retention between the first and the subsequent cycles for $[(ACN)_2$:LiTFSI]:HFE (1:1). This volume ratio exhibits the best electrochemical performance, it corresponds to a low viscosity of 8.6 cP and an ionic conductivity still high for ACN based electrolyte (1.6 $mS.cm^{-1}$). The voltage profile is particular, exhibiting no supersaturation point, no overpotential and less net plateaus.
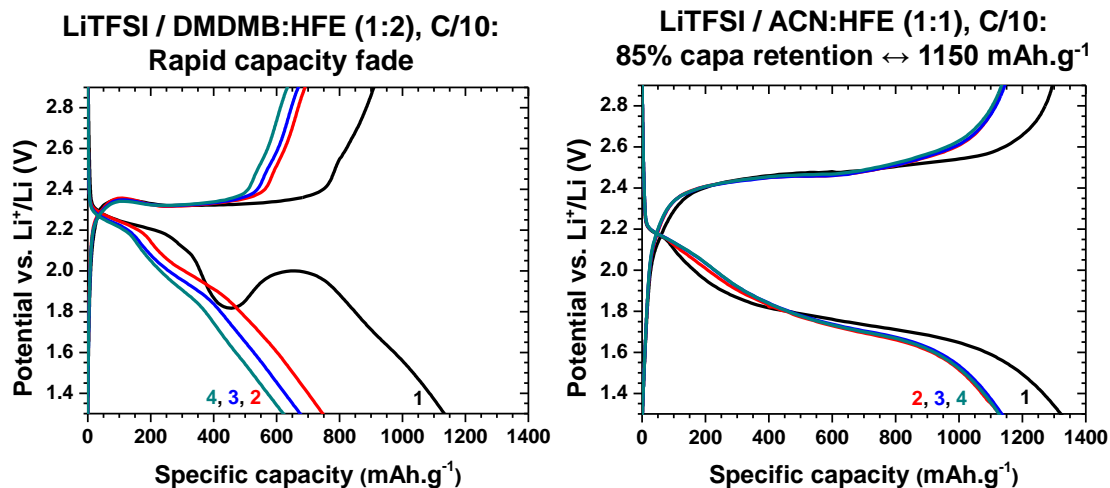
Figure 53. First cycles of Li-S cells using $(DMDMB)_2$:LiTFSI **(left)** or $(ACN)_2$:LiTFSI **(right)** and HFE as a co-solvent.

Unfortunately, such high capacity cannot be retained on the long term, as illustrated by **Figure 54.** After 100 cycles, the specific capacity is higher with ACN:HFE (1:1) than DOL:DME (1:1) − 1M LiTFSI and 2wt% $LiNO_3$. The fading mechanism remains unclear, but can maybe be assigned either to the build-up of insulating Li_2S in the cathode or to the failure of the anode. Indeed, the consumption of Li^+ at the interfaces would result in uncomplexed ACN molecules, rendered free to react with metallic lithium. This failure mechanism could be prevented by protection of the negative electrode in the future, which is pivotal to the development of long performing Li-S batteries.[51,85]
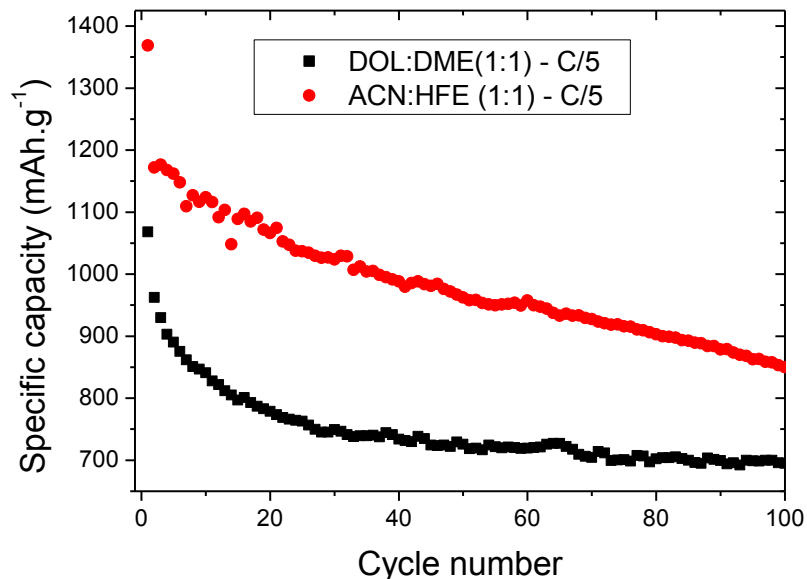
Figure 54. Specific discharge capacities at C/5 using DOL:DME (1:1) – 1M LiTFSI (2wt% LiNO$_3$) and [(ACN)$_2$:LiTFSI]:HFE (1:1).

5.3.5. Investigation of the redox mechanism in ACN based electrolytes.

The electrochemical signature of the cells run in (ACN)$_2$:LiTFSI is particular, and the really low solubility of lithium polysulfides in this electrolyte has drawn attention on the mechanism that could be involved in the cell.

5.3.5.1. First observations.

Celgard® separators recovered from cells run with [(ACN)$_2$:LiTFSI]:HFE (1:1) show no coloration after an half discharge ($\approx$ 800 mAh.g^{-1}, **Figure 55.a** and a full discharge ($\approx$1400 mAh.g^{-1}, **Figure 55.b**), suggesting that little polysulfides are lost in the electrolyte upon discharge.[86] This could mean either that soluble intermediates are not formed or that they exhibit a low mobility within the electrode. This low mobility could explain the difference in the voltage profile (see **Figure 53 (right)**). Indeed, the voltage-composition profile in (ACN)$_2$:LiTFSI

114

electrolytes resembles more to what is commonly observed for monophasic systems – i.e. a sloping curve indicating that the voltage decreases progressively along with an overall composition change – rather than the usual two voltage plateaus characteristics of phase transformations.

a. b.

Figure 55. Celgard® separators recovered from coin cells **a.** half-discharged and **b.** fully discharged.

5.3.5.2. *Operando* XANES measurements on ACN based electrolytes.

Operando XANES measurements at the sulfur K-edge were carried out at the APS at the sector 9-BM-B. Previous XANES measurements showed that sulfur speciation requires the minimization of self-absorption issues to avoid severe distortion of the spectra. This was achieved by the use of porous carbon nanospheres (PCNS) impregnated with sulfur as the active material. However, this cathode could not be used with ACN based electrolytes: for an unclear reason the redox mechanism is not reversible and only one discharge can be achieved. CMK-3 – i.e. carbon nanorods – impregnated with 15 wt% sulfur was chosen as an alternative, but only two dimensions are nanosized in such a material. The total sulfur content of the cathode was decreased by carbon dilution to 10 wt%. The use of CMK-3 as the sulfur host results in severe distortion that is difficult to correct without altering the data as already shown in **Figure 27**.
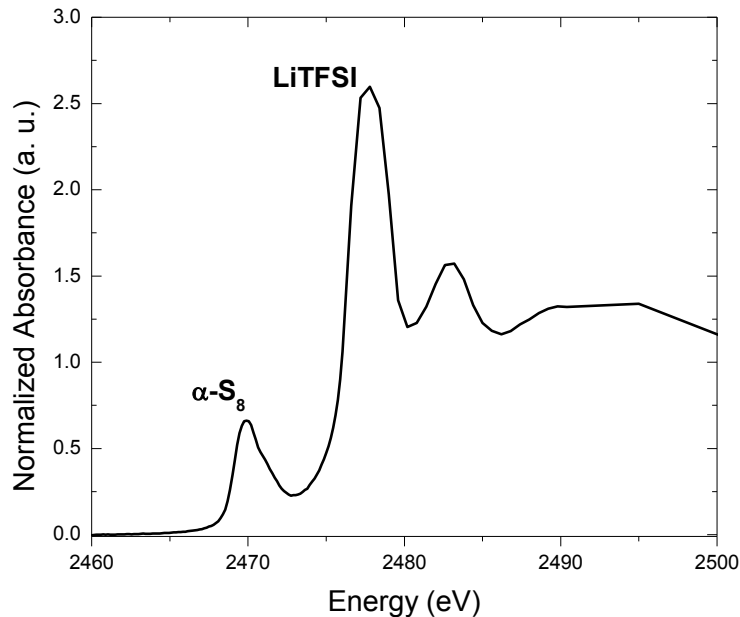
Figure 56. *In situ* Sulfur K-edge of a pristine cathode made with CMK-3/S 15 wt% in the presence of LiTFSI in the electrolyte.

Another strategy implemented for previous *operando* XANES measurements consisted in using $LiClO_4$ instead of LiTFSI as the electrolyte salt to avoid its contribution at the sulfur K-edge. However, neither $LiClO_4$ nor $LiPF_6$ could complex ACN in a similar fashion than LiTFSI. Therefore, the distortion due to self-absorption is overwhelmed by the inherent use of LiTFSI as shown on **Figure 56**. The contribution of LiTFSI around 2477 eV is five times more intense than the one of α-S_8, and impinges on the energy region of interest (2468 eV to 2474 eV typically).

XANES spectra were recorded every 20 minutes during the discharge at C/10. The positive electrode was made of CMK-3 impregnated with 15 wt% of sulfur, PVDF as a binder and Super P as carbon additive, and $[(ACN)_2:LiTFSI]:HFE$ (1:2) was used as the electrolyte. **Figure 57.a** is a 3D plot of the spectra collected upon discharge as a function of capacity. The specific capacity was around 1400 mAh.g^{-1}, in good agreement with previous electrochemical studies on this system. The distortion and the huge contribution of TFSI make a thorough data

analysis – such as Gaussian fit or linear combination as presented in previous report – complicated, but data processing is ongoing.

One can notice the presence of a low energy feature around 2468 eV – characteristic of linear chain polysulfides – proving that they are formed during discharge. Their low mobility, suggested by the absence of coloration of the recovered separators, could prevent chemical equilibria and lead to a gradual reduction rather than the early precipitation of Li_2S. Indeed, while the evolution of the low energy feature undergoes sudden drop/increase for a cell run in conventional DOL:DME – 1M LiTFSI (see **Figure 32)**, its increase is here linear during all the discharge as shown on **Figure 57.b** so that the system behaves more like a solid solution.
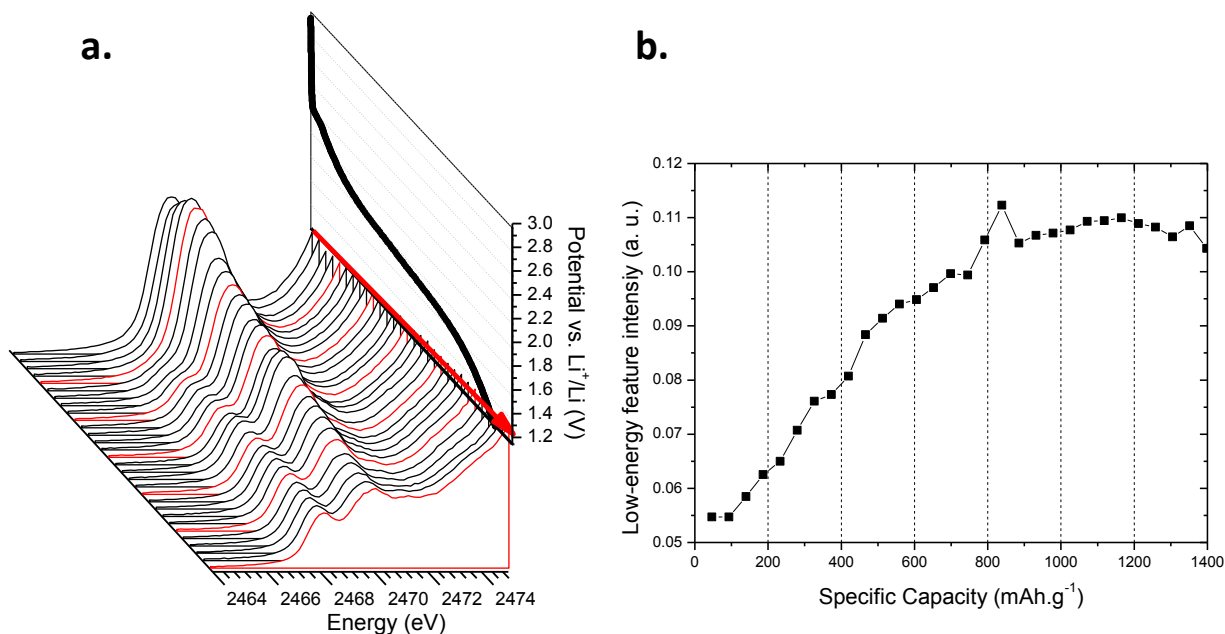
Figure 57. a. 3D plot of the collection of S K-edge spectra of a CMK-3/S-15wt% in [(ACN)₂:LiTFSI]:HFE (1:2) recorded during discharge at C/10. **b.** Evolution of the intensity of the low-energy feature upon discharge.

Figure 58 shows the spectra of the sulfur electrode recorded in the pristine state, the middle of discharge, the end of discharge, and the discharged state after several hours rest. Noticeably, the low energy feature is present in the discharge state but disappears after several hours, suggesting that the remaining polysulfides could diffuse out of the electrode, or engage in chemical reactions if they are given enough time.
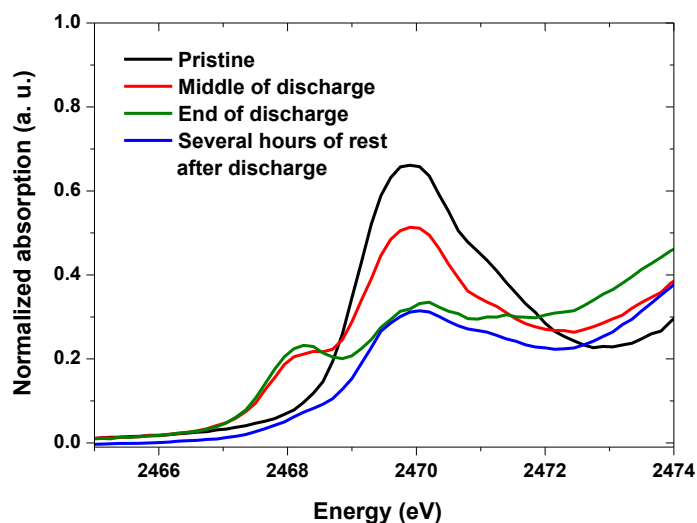
Figure 58. Selection of recorded spectra: pristine (black), middle of discharge (red), end of discharge (green), and discharged state after several hours of rest (blue).

5.4. Conclusion and perspectives.

This chapter investigates novel electrolyte solvents for Li-S cell. The solvents – 1NM1, 1NM2, DMDMB, and ACN – were chosen to tune the solubility of polysulfides and Li_2S. The conclusions of this study are based on the impact of physic-chemical parameters – ionic conductivity, viscosity, and Li_2S and Li_2S_6 solubility – on the electrochemical performances of a Li-S cell. The ionic conductivity and viscosity of the new electrolytes alone are not suitable for electrochemical applications. First, they were mixed with DOL but it appears that the effect is to overwhelm the physic-chemical characteristics of these novel solvents. However, this gave good

118

hints on the design of a Li-S electrolyte: if the dissolution of Li_2S_n cannot be prevented, a high ionic conductivity is required to make them participate efficiently in the redox mechanism. In this context, it appears difficult to overclass DOL:DME – 1M LiTFSI, which exhibit a really high ionic conductivity.

Complexed ACN with LiTFSI – $(ACN)_2$:LiTFSI – exhibits a high viscosity, but dissolves in a very little extent Li_2S_n. The use of HFE enables to use this interesting electrolyte in a Li-S cell and the specific capacity is higher than the one with DOL:DME after 100 cycles. Further experiments should focus on protecting the lithium negative electrode to confirm that the capacity fading originates from the Li/$(ACN)_2$:LiTFSI interface.

The particular electrochemical signature of this electrolyte has attracted attention on the redox mechanism involved. No traces of polysulfides can be seen in the Celgard® separator recovered during discharge. However, the presence of the low energy feature at the sulfur K-edge shows that polysulfides are formed during the electrochemical reduction of sulfur in $(ACN)_2$:LiTFSI, although the constrains imposed by this novel electrolyte to the XANES experiment complicate the data analysis. By comparison with the conventional glyme/sulfone – 1M LiTFSI solutions, fully complexed acetonitrile may not permit polysulfides to equilibrate in solution and therefore the voltage-composition profile does not exhibit usual features such as a short upper voltage plateau, a super-saturation knee and a long lower voltage plateau. Instead, polysulfides may be reduced progressively, resulting in a smooth sloping discharge curve.

6. <u>Future perspectives.</u>

This thesis was devised as a fundamental study of the Li-S system by the use of ^{7}Li MAS NMR, XANES, and NRIXS. These spectroscopies present the advantage to be local probes that could be sensitive to the amorphous intermediates species formed upon (dis)charge, giving novel insights in the redox chemistry of sulfur and guiding the future design of Li-S cell to enhance the performance of this system. However, the lack of knowledge – and the absence of suitable reference compounds – about lithium polysulfides, Li_2S_n, renders any spectroscopic study equivocal.

In that purpose, the first part of this thesis aimed to synthesize and characterize lithium polysulfides, which had never been isolated as stable intermediate phases between elemental sulfur and lithium. By the chemical reaction of Super Hydride and elemental sulfur, a novel stable phase was isolated. The existence of this compound, which corresponds to Li_2S_6, was proved by ^{7}Li NMR that shows a unique lithium environment. However, ^{7}Li NMR performed during this thesis failed to distinguish other targeted Li_2S_n. In the future, higher field NMR could better resolve the narrow chemical shifts displayed between these compounds. Also, ^{33}S NMR could be used to probe the sulfur environment. Preliminary ongoing experiments are very promising, with for instance the prospect to access Li diffusivity in the various sulfur redox species or explain the potential barrier when (re)oxidizing Li_2S. Neutron Pair Distribution Function could also offer a unique insight on the structure of Li_2S_6, which could help understanding its formation and consumption.

The successful synthesis of Li_2S_6 enabled to build a spectral database, for both XANES and NRIXS, built on S_8, Li_2S_6, Li_2S, and sodium polysulfides Na_2S_2 and Na_2S_4 to complete the

picture. The overall conclusion of NRIXS is that the distinction between the different sulfur species is delicate at both the sulfur L-edge and the lithium K-edge; on top of that, *ex situ* measurements showed that the constraints of this technique may compromise *operando* measurements. Future work could try to perform this experiment on binder-free electrodes with high sulfur loading that have been reported in the literature.

However, a clear distinction can be made between linear chain polysulfides, lithium sulfide, and elemental sulfur using XANES at the sulfur K-edge. Among linear chain polysulfides, short-chain and long-chain polysulfides can be distinguished based on the intensity of the low-energy feature that is only present in these compounds. These references opened the way to perform *operando* XANES measurements on the Li-S system by the use of nano-sized PCNS/S to reduce the inherent distortion of the spectra. The analysis of the evolution of the XANES spectra gave important insights on the Li-S cell, showing the redox mechanism involved during (dis)charge. In the future, EXAFS should provide a deeper understanding of the structure of (dis)charged products. Beside this study on a typical Li-S system, XANES measurements were performed on heat-treated PCNS/S that exhibits an untypical electrochemical signature. After a first electrochemical study via PCGA, *operando* XANES measurements showed a clear evolution at the sulfur K-edge mimicking the redox behavior. More XANES measurements should come in the next future to obtain reference spectra by, for example, coupling the PCGA and XANES.

In parallel with these fundamental investigations of the Li-S system, a systematic study of novel electrolytes was conducted by measuring their ionic conductivity, viscosity, and polysulfides solubility. The goal here was to tune the Li_2S_n solubility to see the impact on the electrochemistry. When blended with HFE, complexed ACN and LiTFSI showed fairly good specific capacity retention after 100 cycles and attracted attention due to its smoother voltage

profile. Future research should focus on the protection of the lithium metal anode to prevent any degradation from ACN, which could be the most important mechanism of capacity loss. First observations on the redox mechanism showed no evidence of the formation of polysulfides, but *operando* XANES measurements prove that they participate in the redox mechanism. This one appears to happen more gradually than typical Li-S because of the low mobility of Li_2S_n that may not be able to equilibrate in solution. The XANES data analysis is difficult, but future work should aim to confirm this mechanism.

REFERENCES

1   Regulation (EC) No 443/2009 of the European Parliament and of the Council of 23 April 2009 setting emission performance standards for new passenger cars as part of the Community's integrated approach to reduce CO 2 emissions from light-duty vehicles.

2   Global Warming Pollution Reduction Act

3   Budde-Meiwes, H., Drillkens, J., Lunz, B., Muennix, J., Rothgang, S., Kowal, J. & Uwe Sauer, D. A review -of current automotive battery technology and future prospects, *Proc. Inst. Mech. Eng. D J. Automob. Eng.*, **227**, 761-776 (2013)

4   Jacoby, M. Burning Batteries, *Chemical and Engineering News,* **85**, 26-28 (2007)

5   Deutsche Bank, The end of the Oil Age – 2011 and beyond: a reality check (2010)

6   Peramunage, D. & Licht, S. Asolid sulfur cathode for aqueous batteries, *Science*, **261**, 1029-1032 (1993)

7   Hagen, M., Dörfler, S., Fanz, P., Berger, T., Speck, R., Tübke, J., Althues, H., Hoffmann, M. J., Scherr, C. & Kaskel, S. Development and costs calculation of lithium-sulfur cells with high sulfur load and binder free electrodes. *J. Power Sources*, **224**, 260-268 (2013)

8   Yamin, H. & Peled, E. Electrochemistry of a Nonaqueous Lithium/Sulphur Cell. *J. Power Sources*, **9**, 281-287 (1983)

9   Dean, J,-A. Lange's Handbook of Chemistry (1985)

10   He, X., Ren, J., Wang, L., Pu, W., Jiang, C. & Wan, C. Expansion and shrinkage of the sulfur composite electrode in rechargeable lithium batteries. *J. Power Sources*, **190**, 154-156 (2009)

11   Elazari, R., Salitra, G., Talyosed, Y., Grinblat, J., Scordilis-Kelley, C., Xiao, A., Affinito, J. & Aurbach, D. Morphological and structural studies of composite sulfur electrodes upon cycling by HRTEM, AFM and Raman spectroscopy. *J. Electrochem. Soc.*, **157**, A1131-A1138 (2010)

12   Barchasz, C., Lepêtre, J.-C., Alloin, F. & Patoux, S. New insights into the limiting paramters of the Li/S rechargeable cell. *J. Power Sources*, **199**, 322-330 (2011)

13   Cheon, S. E., Ko, K. S., Cho, J. H., Kim, S. W., Chin, E. Y. & Kim, H. T. Rechargeable lithium sulfur battery, *J. Electrochem. Soc.,* **150**, A796-799 (2003)

14   Rauh, R. D., Abraham, K. M., Pearson, G. F., Surpenant, J. K. & Brummer, S. B. A lithium/dissolved sulfur battery with an organic electrolyte. *J. Electrochem. Soc.*, **126**, 523-527 (1979)

15   Diao, Y., Xie, K., Xiong, S. & Hong, X. Shuttle phenomenon – The irreversible oxidation mechanism of sulfur active materal in Li-S battery. *J. Power Sources*, **235**, 181-186 (2013)

[16]   Rao, B. M. L. & Shropshire, J. A., *J. Electrochem. Soc.*, **128**, 942 (1981)

[17]   Nelson, J, Misra, S., Yang, Y., Jackson, A., Liu, Y., Wang, H., Dai, H., Andrews, Cui, Y. & Toney, M. F. In operando X-ray diffraction and transmission X-ray microscopy of lithium sulfur batteries. *J. Am. Chem. Soc.,* **134**, 6337 (2012)

[18]   Diao, Y., Xie, K., Xiong, S. & Hong, X. Analysis of polysulfide dissolved in electrolyte in discharge-charge process of Li-S battery. *J. Electrochem. Soc.*, **159**, A421-A425 (2012)

[19]   Peled, E., Sternberg, Y., Gorenshtein, A. & Lavi, Y. Lithium–sulfur battery: Evaluation of dioxolane-based electrolytes. *J. Electrochem. Soc.* **136**, 1621–1625 (1989)

[20]   Akridge, J. R., Mikhaylik, Y. V. & White, N. Li/S fundamental chemistry and application to high-performance rechargeable batteries. *Solid State Ion*. **175**, 243-245 (2004)

[21]   Liang, C., Dudney, N. J. & Howe, J. Y. Hierarchically structured sulfur/carbon nanocomposite material for high-energy lithium battery. *Chem. Mater.* **21**, 4724-4730 (2009)

[22]   Zheng, G., Zhang, Q., Cha, J. J., Yang, Y., Li; W., Seh, Z. W. & Cui, Y. Amphilic surface modification of hollow carbon nanofibers for imroved cycle life of lithium sulfur batteries. *Nano Lett.*, **13**, 1265-1270 (2013)

[23]   Barchasz, C., Molton, F., Duboc, C., Leprêtre, J. C., Patoux, S. & Alloin, F. Lithium/sulfur cell discharge mechanism : an original approach for intermediate species identification. *Anal. Chem.*, **84**, 3973-3980 (2012)

[24]   Tobishima, S.-I., Yamamoto, H. & Matsuda, M. Study on the reduction species of sulfur by alkali metals in nonaqueous solvents. *Electrochimica Acta* **42**, 1019-1029 (1997)

[25]   Patel, M. U. M., Demir-Cakan, R., Marcrette, M., Tarascon, J.-M., Gaberscek, M. & Dominko, R. Li-S battery analyzed by UV/Vis in Operando mode. *Chem. Sus. Chem.* DOI: 10.1002/cssc.20300142 (2013)

[26]   Argyropoulos, D. S., Hou, Y., Ganesaratnam, R., Harpp, D. N. & Koda, K. Quantitative NMR analysis of alkaline polysulfide solutions. *Holzforschung*, **59**, 124-131 (2005)

[27]   Badoz-Lambling, J., Bonnaterre, R., Cauquis, G., Delamar, M. & Demange, G. La reduction du soufre en milieu organique. *Electrochimica Acta* **21**, 119-131 (1976)

[28]   Yamin, H., Gorenshtein, A., Penciner, J., Sternberg, Y. & Peled, E. Lithium – sulfur battery. Oxidation/reduction mechanisms of polysulfides in THF solutions. *J. Electrochem. Soc.: Electrochem. Sc. Techno.* **135**, 1045-1048 (1988)

[29]   Li, Y.,Zhan, H., Liu, S., Huang, K. & Zhou, Y. Electrochemical properties of the soluble reduction products in rechargeable Li/S battery. *J. Power Sources* **195**, 2945–2949 (2010)

[30]   Mikhaylik, Y. V. & Akridge, J. Polysulfide shuttle study in the Li/S battery system. *J. electrochem. Soc.*, **151**, A1969-A1976 (2004)

[31]   Cheon, S.-E., Ko, K.-S., Cho, J.-H., Kim, S.-W., Chin, E.-Y. & Kim, H.-T. Rechargeable lithium sulfur battery II. Rate capability and cycle characteristics. *J. Electrochem. Soc.* **150**, A800-A805 (2003)

[32]   Choi, Y.-J., Chung, Y.-D., Baek, C.-Y., Kim, K.-W., Ahn, H.-J. & Ahn, J.-H. Rechargeable lithium/sulfur battery with liquid electrolytes containing toluene as additive. *J. Power Sources* **184**, 441-445 (2008)

[33]   Yuan, L., Qiu, X., Chen, L. & Zhu, W. Improvement of cycle property of sulfur-coated multi-walled carbon nanotubes composite cathode for lithium/sulfur batteries. *J. Power Sources* **189**, 1141-1146 (2009)

[34]   Yuan, L., Qiu, X., Chen, L. & Zhu, W. New insight into the discharge process of sulfur cathode by electrochemical impedance spectroscopy. *J. Power Sources* **189**, 127-132 (2009)

[35]   Gao, J., Lowe, M. A., Kiya, Y. & Abruña, H. D. Effects of liquid electrolytes on the charge discharge performance of rechargeable lithium/sulfur batteries: electrochemical and in-situ x-ray absorption spectroscopic studies. *J. Phys. Chem. C.* **115**, 25132–25137 (2011)

[36]   Ji, X., Tae Lee, K. & Nazar, L. F. A highly ordered nanostructured carbon-sulphur cathode for lithium-sulphur batteries. *Nat. Mat.*, **8**, 500-506 (2009)

[37]   Jayaprakash, N., Shen, J., Moganty, S. S., Corona, A. & Archer, L. A. Porous Hollow Carbon@Sulfur Composites for High-Power Lithium–Sulfur Batteries. *Angew. Chem*., **123**, 6026(2011)

[38]   Kim, J., Lee, D.-J., Jung, H.-G., Sun, Y.-K., Hassoun, J. & Scrosati, B. An advanced lithium-sulfur battery. *Adv. Funct. Mater*., **23**, 1076-1080 (2013)

[39]   Guo,J., Xu, Y. & Wang, C. Sulfur-impregnated disordered carbon nanotubes cathode for lithium-sulfur batteries. *Nano Lett.*, **11**, 4288-4284 (2011)

[40]   Zheng, G., Yang, Y., Chan, J. J., Hong, S. S. & Cui, Y. Hollow carbon nanofiber-encapsulated sulfur cathodes for high specific capacity rechargeable lithium batteries. *Nano Lett.*, **11**, 4462-4467 (2011)

[41]   Wang, H., Yang, Y., Liang, Y., Robinson, J. T., Li, Y., Jackson, A., Cui, Y. & Dai, H. Graphene-wrapped sulfur particles as a rechargeable lithium-sulfur battery cathode material with high capacity and cycling stability. *Nano Lett.*, **11**, 2644-2647 (2011)

[42]   Ji, L., Rao, M., Zheng, H., Zhang, L., Li, Y., Duan, W., Guo, J., Cairns, E. J. & Zhang, Y. Graphene oxide as a sulfur immobilizer in high performance lithium/sulfur cells. *J. Am. Chem. Soc.*, **133**, 18522-18525 (2011)

[43]   Ryu, H. S., Ahn, H. J., Kim, K. W., Ahn, J. H., Lee, J. Y. & Cairns, E. J. Self-discharge of lithium-sulfur cells using stainless-steel current-collectors. *J. Power Sources*, **140**, 365-369 (2005)

[44]   Ryu, H.-S. & Ahn, H.-J. Self-discharge behavior of lithium/sulfur battery using aluminum current collector. *Mater. Sci. Forum*, **486-487**, 630-633 (2005)

[45]   Peled, E., Gorenshtein, A., Segal, M. & Sternberg, Y. Rechargeable lithium-sulfur battery. *J. Power Sources*, **26**, 269-271 (1989)

[46]   US Patent no. 6255002B1

[47]   US Patent no. 6030720

[48]   Kim, H. S. & Jeong, C.-S. Electrochemical properties of binary electrolytes for lithium-sulfur batteries. *Bull. Korean Chem. Soc.*, **32**, 3682-3686 (2011)

[49]   Choi, J.-W., Kim, J.-H., Cheruvally, G., Ahn, J.-H., Kim, K.-W., Hyo-Jun, A. & Kim, J.-U. Microporous poly(vinylidene fluoride-*co*-hexafluoropropylene polymer electrolytes for lithium/sulfur cells. *J. Ind. Eng. Chem.*, **12**; 939-949 (2006)

[50]   US Patent no. 20080187840A1

[51]   Aurbach, D., Pollak, E., Elazari, R., Salitra, G., Scordilis Kelley, C. & Affinito, J. On the surface chemical aspects of very high energy density, rechargeable Li-sulfur batteries. *J. Electrochem. Soc.*, **156**, A694-A702 (2009)

[52]   Chen, S., Dai, F. Gordin, M. L. & Wang, D. Exceptional electrochemical performance of rechargeable Li-S batteries with a polysulfide-containing electrolyte. *RSC Adv*, **3** 3540 (2013)

[53]   Xu, R., Belharouak, I., Li, J. C. M., Zhang, X., Bloom, I. & Bareño Role of polysulfides in self-healing lithium-sulfur batteries. *Adv. Energy Mater.*, DOI: 10.1002/aenm.201200990 (2013)

[54]   Bragg, W. L. The diffraction of short electromagnetic waves by a crystal. *Proc. Cambridge Phil. Soc.*, **17**, 43-57 (1913)

[55]   Balasubramanian, M., Sun, X., Yang, X. Q. & McBreen, J. In situ x-ray absorption studies of a high-rate $LiNi_{0.85}Co_{0.15}O_2$ cathode material. *J. Electrochem. Soc.* **147**, 2903-2909 (2000)

[56]   Yang, X. Q., Xue, K. H., Lee, H. S., Guo, Y. H. & McBreen J. *In situ* X-ray absorption studies of organo-disulfide redox polymeric electrodes. *The Electrochem. Soc.*, **140**, 943-946 (1993)

[57]   Newville, M. Fundamentals of XAFS. *Consortium for advanced radiation sources* (2004)

[58]   http://wap.ati.ac.at/index.php?id=247 Atominstitut Institute of Atomic and Subatomic Physics.

[59]   Data calculated from http://henke.lbl.gov/optical_constants/atten2.html

[60]   Manceau A. & Nagy K.L. Quantitative analysis of sulfur functional groups in natural organic matter by XANES spectroscopy. *Geochimica et Cosmochimica,* **99**, 206-223 (2012)

[61]   Ravel, B. & Newville, M. J. ATHENA, ARTEMIS, HEPHAESTUS: data analysis for X-ray absorption spectroscopy using IFEFFIT. *J. Synchrotron Rad.* **12**, 537-541 (2005)

[62]   Okamto, H. The Lithium-Sulfur System. *J. Phase Equilibria*, **16**, 94-97 (1995)

[63]   Rauh, R. D., Shuker, F. S., Marston, J. M. & Brummer, S. B. Formation of lithium polysulfides in aprotic media. *J. Inor. Nucl. Chem.*, **39**, 1761-1766 (1977)

64   Sangster, J. & Pelton, A. D. The Sodium-Sulfur system. *J. Phase Equilibria*, **18**, 89-96 (1997)

65   Gladysz, J.A., V. K. Wong, V. K. & Jick, B.S. Introduction of Sulfur into Organic Molecules via Lithium Triethylborohydride Reduction of S_8. *J. Chem. Soc., Chem. Commun.* **19**, 838-839 (1978)

66   Takahara, H., Tabuchi, M., Takeuchi, T., Kageyama, H., Ide, J., Handa, K., Kobayashi, Y., Kurisu, Y., Kondo, S. & Kanno, R. Application of lithium metal electrodes to all-solid-state lithium secondary batteries using Li_3PO_4-Li_2S-SiS_2 glass. *J. Electrochem. Soc*. **151**, A1309-A1313 (2004)

67   Totir, D. A., Antonio, M. RM, Schiling, P., Tittsworth, R. & Scherson, D. A. In situ sulfur K-edge X-ray absorption near edge structure of an embedded pyrite particle electrode in a non-aqueous Li^+-based electrolyte solution. *Electrochemica Acta*, **47**, 3195-3200 (2002)

68   Pickering, I. J., George, G. N., Yu, E. Y., Brune, D. C., Tuschak, C., Overmann, J., Beatty, J. T. & Prince, R. C. Analysis of sulfur biochemistry of sulfur bacteria using X-ray absorption spectroscopy. *Biochem*, **40**, 8138-8145 (2001)

69   Athena User's Guide, version 1.5, Bruce Ravel (2009)

70   Naoi, K., Kawase, K. I. & Inoue, Y. A new energy storage material : organosulfur compounds baed on multiple sulfur-sulfur bonds. *J. Electrochem. Soc.*, **144**, L170-L172 (1997)

71   Visco, S. J., Mailhe, C. C., De Jonghe, L. C. & Armand M. B. A novel class of organosulfur electrodes for energy sulfur. *J. Electrochem. Soc.*, **136**, 661-664 (1989)

72   Wang, L., He, X., Li, J., Gao, L.., Guo, J., Jianga, C. & Wana, C. Analysis of the synthesis process of sulphur-poly(acrylonitrile)-based cathode materials for lithium batteries. *J. Mater. Chem.*, **22**,22077-22081 (2012)

73   Wang, J., Liu, L., Ling, Z., Yang, J., Wana, C. & Jiang, C. Polymer lithium cells with sulfur composites as cathode materials. *Electrochem. Acta*, **48**, 1861-1867 (2003)

74   Wang, J. Z., Lua, L., Choucairc, M. Strided, J. A., Xua, X. & Lieu, H.-K Sulfur-graphene composite for rechargeable lithium batteries. *J. Power Sources*, **196**, 7030-7034 (2011)

75   Guo, J., Xu, Y. & Wang, C. Sulfur-impregnated disordered carbon nanotubes cathode for lithium-sulfur batteries. *Nano Lett.*, **11**, 4288-4294 (2011)

76   Lai, C., Gao, X. P., Zhang, B., Yan, T. Y. and Zhou, Z. Synthesis and electrochemical performance of sulfur/highly porous carbon composites. *J. Phys. Chm. C*, **113**, 4712-4716 (2009)

77   Yang, Z., Yao, Z., Li, G., Fang, G., Nie, H., Liu, Z., Zhou, X., Chen, X. & Huang, S. Sulfur-doped graphene as an efficient metal-free cathode catalyst for oxygen reduction. *ACS Nano*, **6**, 205-211 (2012)

78   Cheon, S.-E., Ko, K.-S., Cho, J.-H., Kim, S.-W. Chin, E.-Y. & Kim, H.-T. Rechargeable Lithium Sulfur Battery: I. Structural change of sulfur cathode during discharge and charge. *J. Electrochem. Soc.*, **150**, A796-A799 (2003)

79   US Patent no. 6225002 B1

80   Zhang, Z., Lu, J., Assary, R. S., Du, P., Wang, H.-H., Sun, Y.-K., Qin, Y. Lau, K. C., Greeley, J., Redfern, P. C., Iddir, H., Curtiss, L. A. & Amine, K. Increased stability toward oxygen reduction products for Lithium-air batteries with oligoether-functionalized silane electrolyte. *J. Phys. Chem.*, **115**, 25535-25542 (2011)

81   Furukawa, K., Yamada, Y., Yaegashi, M., Zhou, H. & Yamada A. Li-Air battery using stabilized acetronitrile electrolyte. *The Electrochem Soc.*, Abstract #182 (2012)

82   Seo, D. M., Borodin, O., Han, S.-D., Boyle, P. D. & Henderson, W. A. Electrolyte solvation and ionic association II. Actetonitrile-Lithium salt mixtures: highly dissociated salts.

83   Dominko, R., Demir-Cakan, R., Morcrette, M. & Tarascon, J.-M . Analytical detection of soluble polysulphides in a modified Swagelok cell. *Electrochem. Comm.*, **13**, 117-120 (2011)

84   Watanabe et al., Abstract #12, Honolulu PRIME (2012)

85   Lee, Y. M., Choi, N.-S., Park, J. H. & Park, J.-P Electrochemical performance of lithium/sulfur batteries with protected Li anodes. *J. Power Sources*, **119-121**, 964-972 (2003)

86   Patel, M. U. M., Demir-Cakan, R., Morcrette, M., Tarascon, J.-M., Gaberscek, M. & Dominko, R. Li-S battery analyzed by UV/Vis in Operando Mode, *ChemSusChem*, **6**, 1177-1181 (2013)